TYPE Ia SUPERNOVAE AS TOOLS FOR COSMOLOGY

Patrice M. OKOUMA

THESIS SUBMITTED IN PARTIAL FULFILLMENT
OF THE REQUIREMENTS FOR THE DEGREE OF

MASTER OF SCIENCE in ASTROPHYSICS and SPACE SCIENCE

IN THE DEPARTMENT
OF
MATHEMATICS AND APPLIED MATHEMATICS

UNIVERSITY OF CAPE TOWN

May 2008

Acknowledgments

First of all I would like to thank my supervisor Prof. Bruce A. Bassett for making it possible for me to complete my master's studies in such an oustanding institution as UCT, and also for suggesting a very instructive topic to work with. My M.Sc project has greatly benefited from fruitful discussions with several other students from UCT, most importantly with Renée Hlozek, Jacques Kotze and Yabebal Tadesse. Thank you ! Also a very special thank is to be addressed to the South African National Astrophysics and Space Science Programme (NASSP) for the full support provided. These thanks would be incomplete if i did not mention Gabon - one of my homes - for the permanence. May all those who came before me perceive my deep gratitude.

I know the meaning of plagiarism and declare that all of the work in the document, save for that which is properly acknowledged, is my own.

Abstract

In this thesis both the theoretical and observational foundations of dark energy are explored, as well as our present day understanding of Type Ia supernovae (SNe Ia). The core of the thesis addresses the problem of identifying the phase (time since explosion) and redshift of a Type Ia supernova from its spectrum by comparison with the Nugent set of SNe Ia spectral templates. Solutions have been implemented using both grid and Markov Chain Monte Carlo (MCMC) maximum likelihood methods, which have been tested against the templates themselves and data from the SUSPECT supernova database. While the method works well in some cases, the limited number of templates and noise/systematic errors in the spectra make matching challenging for other cases. For completeness we compare with the cross-correlation techniques used by the recently released SuperNova IDentification code (SNID). SNID uses an algorithm developed by (Blondin and Tonry, 2006) and gives accurate estimates for redshift ($\sigma_z \leq 0.01$) and phase ($\sigma_t \leq 3$ days) of SNe Ia. By including a range of non-SNe Ia templates, SNID also constrains the type of the supernova under consideration. Nevertheless, even SNID struggles in some cases, which means that a small fraction of supernovae spectra are never identified, even in the large on-going SNe Ia surveys such as SDSS, ESSENCE and SNLS.

Contents

List of Tables

List of Figures

Chapter 1

Introduction

1.1 Modern cosmology

Cosmology is the branch of science investigating the structure and evolution of the universe as a whole. Its recent evolution has led it from the highly speculative field of mere philosophy to a data-driven field of knowledge with a well established formalism. (Hubble, 1929), established a relationship between the redshift and distance of galaxies. Soon after, it became clear that the universe was expanding : a static universe was therefore impossible. The theory of the Big Bang found solid grounds in the process of back tracking that observed expansion. The future of the universe seemed then contained into two dominant scenarios : a future collapse or an expansion forever; both depending on the density of matter present in the universe.

Recent observations showing that the universe is experiencing an accelerated phase of expansion, sent a shockwave through the scientific community. The term Dark Energy (DE) has been coined to name the energy driving that acceleration. According to current estimates, approximately two-thirds of our universe is made up of that smoothly distributed DE component, about one-third is in the form of the pressureless Cold Dark Matter (CDM), while the familiar baryonic matter makes up less than 5% of the total density of the Universe. These hypotheses and values come from the Standard Model of cosmology, which is basically sustained by a philosophical postulate - the cosmological principle - and by Albert Einstein's General Theory of Relativity.

No satisfying particles have been yet discovered for making up the CDM. Various candidates are still being explored from particle physics. Concerning dark energy, the dominant beliefs assume that it might be caused by Einstein's cosmological constant,Λ, leading to the ΛCDM model; or by a time-varying scalar field rolling slowly down the potential and thus being dominated by the potential energy.

1.2 This thesis

With the observational evidence for an accelerated phase of expansion of the universe, Type Ia supernovae (SNe Ia) have become important astronomical objects for quantifying the dynamics of the universe. Because of that there is an urgent need for a better understanding of their physics as well as a more accurate knowledge of their properties in terms of redshift, phase and type.

In this thesis, parameter estimation from SNe Ia spectra is performed. Both a grid based χ^2 method and a Markov Chain Monte Carlo (MCMC) simulation are performed to fit template

spectra to SNe Ia data. The aim is to estimate: (a) the redshift of the SN Ia, (b) the phase of the targeted SN Ia relative to the time of B-band maximum brightness. Nugent's templates are used. The data are from SUSPECT, an online database of supernovae ($http://bruford.nhn.ou.edu/\sim suspect/index1.html$). A cross-correlation technique and tool is also presented.

Chapters 2 and 3 give a review of the theoretical and observational foundations for DE. Chapter 4 gives some elements on the present day understanding of Type Ia supernovae. In chapter 5, two commonly used statistical methods for parameter estimation in cosmology are applied, namely grid based χ^2 and Markov Chain Monte Carlo (MCMC). The related codes and results are also discussed. In chapter 6, SNID, a cross-correlation based tool recently developped by (Blondin and Tonry, 2006) is presented. The summary is given in chapter 7.

Chapter 2

Basic concepts of Friedman-Lemaître-Robertson-Walker (FLRW) cosmology

2.1 The metric

The metric in any given space of finite dimension is the mathematical tool that allows to characterize some properties of that space, like distances. The common one in the everyday (three-dimensional) space is the one associated to the determination of distance in euclidian space. An infinitesimal distance ds is given there by :

$$ds^2 = dx^2 + dy^2 + dz^2 = g_{ij} dX^i dX^j, \tag{2.1}$$

with $X = (x, y, z)$ and $i, j = 1, 2, 3$. The associated metric being :

$$g_{ij} = \begin{pmatrix} 1 & 0 & 0 \\ 0 & 1 & 0 \\ 0 & 0 & 1 \end{pmatrix} \quad \text{where i,j = 1,2,3.} \tag{2.2}$$

The general equation that Einstein obtained in his theory of general relativity is (Dodelson, 2003) :

$$G_{\mu\nu} \equiv R_{\mu\nu} - \frac{1}{2} g_{\mu\nu} R = 8\pi G T_{\mu\nu} \quad with\ \mu, \nu = 0, 1, 2, 3. \tag{2.3}$$

The relation in (2.3) relates the Einstein tensor, $G_{\mu\nu}$, describing the geometry, to $T_{\mu\nu}$, the energy-momentum tensor describing the energy content of space-time. $R_{\mu\nu}$ is the Ricci tensor: It depends on the metric $g_{\mu\nu}$ and its derivatives. $R = g^{\mu\nu} R_{\mu\nu}$ is the Ricci scalar, the contraction of the Ricci tensor. G is Newton's constant.

With that equation for space-time, it was natural - in view of its components - to suppose that it could have some applications in cosmology. Assuming some relevant symmetries, the Einstein equations have simple analytical solutions. The Friedmann-Lemaitre-Robertson-Walker (FLRW) metric is based on the assumption of homogeneity and isotropy of the universe (the cosmological principle). A line-element, ds, via that metric is defined as :

$$ds^2 = -c^2dt^2 + a(t)^2\left[\frac{dr^2}{1-kr^2} + r^2\left(d\theta^2 + \sin^2\theta d\phi^2\right)\right], \tag{2.4}$$

where

- $a(t)$ is the scale factor and corresponds to the radius of curvature of space-like sections;
- The coordinates r, θ and ϕ are known as comoving coordinates. A freely moving particle comes to rest in these coordinates.
- t, is the proper time measured by comoving observers and c is the speed of light;

The constant k - the curvature parameter - in Eq. (2.4) gives the geometry of the spatial section of space-time. Because $a(t)$ and k are arbitrarily chosen, one can rescale $a(t)$ so that there are only three possible values for k :

- $k = -1$, the geometry of the universe is open (hyperbolic) meaning that two parallel lines will eventually diverge from each other,
- $k = 0$, the universe is flat meaning that two parallel lines remain parallel,
- $k = +1$, the geometry of the universe is closed (spherical) meaning that two parallel lines will eventually cross each other.

Currently a good test for the assumption of isotropy is provided by all-sky Cosmic Microwave Background (CMB) experiments like COBE (COsmic Background Explorer) and WMAP (Wilkinson Microwave Anisotropy Probe) whose result is illustrated in figure 2.1. The isotropy around all the other points as can be expected if our location is by no means special, also implies homogeneity (figure 2.2).

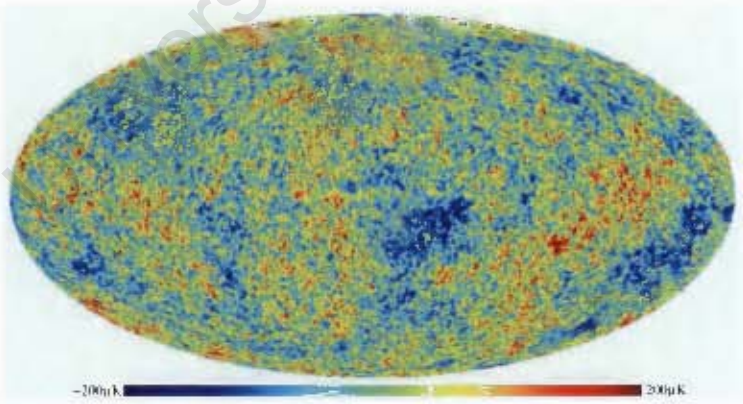

Figure 2.1: *Evidence for the large scale isotropy of the Universe via the observation of the Cosmic Microwave Background with the WMAP probe. Temperature fluctuations are of the order of* $\frac{\Delta T}{T} \sim 10^{-5}$. *According to the gravitational instability theory, these measurements tell us about the thermal history of the universe and they provide a picture of the lumps of matter that were the seeds of the structure we observe today. Source : (Tegmark* et al., *2003).*

It is clear from Eq. (2.4) that the effect of k is negligible for small r, meaning that *one must look at a large volume to see the effect of curvature*. A radial light ray (i.e $d\theta = d\phi = 0$) moving

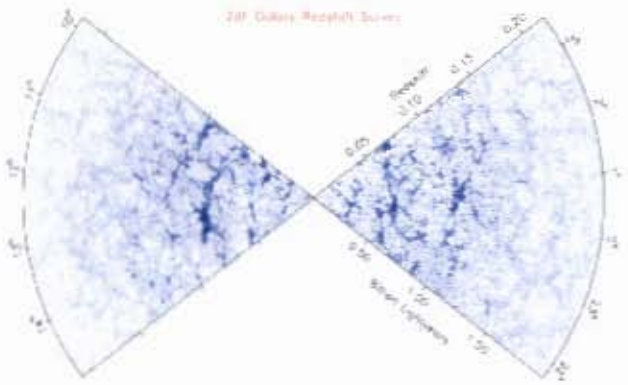

Figure 2.2: *Evidence for the large scale homogeneity of the universe via the observation of the Large Scale Structure in the 2dF survey. Structures (inhomogeneities) are prevalent at redshift < 0.1. They visibly recede on larger scales due to incompleteness of the survey. Our own galaxy is located at the intercepts of both portions of the observed sky. Source : (Colless* et al., *2003).*

towards an observer is considered. The observer can be put at the origin without loss of generality. Eq. (2.4) and the fact that for a light ray, $ds^2 = 0$ bring :

$$\frac{c^2 dt^2}{a(t)^2} = \frac{dr^2}{1 - kr^2}. \tag{2.5}$$

Therefore :

$$\frac{cdt}{a(t)} = +\frac{dr}{\sqrt{1 - kr^2}}. \tag{2.6}$$

Because the ray is an incoming one relative to the observer (i.e $dr < 0$) :

$$\frac{cdt}{a(t)} = -\frac{dr}{\sqrt{1 - kr^2}}. \tag{2.7}$$

By defining :

$$d\chi = \frac{dr}{\sqrt{1 - kr^2}} \Longleftrightarrow \chi = -\int_r^{r_0} \frac{dr_*}{\sqrt{1 - kr_*^2}} \Longleftrightarrow r = S_k(\chi), \tag{2.8}$$

with

$$S_k(\chi) = \begin{cases} \sinh(\chi) & if\ k = -1 \\ \chi & if\ k = 0 \\ \sin(\chi) & if\ k = 1. \end{cases} \tag{2.9}$$

in units where $c = 1$. An integration of Eq.(2.8) leads to

- $\chi = arcsinh(r) \Longleftrightarrow r = \sinh(\chi) = S_k(\chi)$ for an open universe $(k = -1)$,
- $\chi = r = S_k(\chi)$ for a flat universe $(k = 0)$,
- $\chi = \arcsin(r) \Longleftrightarrow r = \sin(\chi) = S_k(\chi)$ for a closed universe $(k = 1)$.

The line element in a FLRW background becomes :

$$ds^2 = -dt^2 + a(t)^2 \left[d\chi^2 + S_k(\chi)^2 \left(d\theta^2 + \sin^2 \theta d\phi^2 \right) \right], \tag{2.10}$$

2.2 Cosmological equations

Einstein's equations :

$$G_{\mu\nu} \equiv R_{\mu\nu} - \frac{1}{2} g_{\mu\nu} R = 8\pi G T_{\mu\nu}, \tag{2.11}$$

formulates the interplay between the geometry and the energy content of space-time. In all the following derivations a perfect fluid is considered. In physics, a perfect (ideal) fluid is a fluid that can be completely characterized by its rest frame energy density ρ and pressure p. In the case of an ideal fluid as the source of the energy momentum tensor $T_{\mu\nu}$ measured in a local free-fall frame comoving with the fluid (i.e. $g_{\mu\nu} = \eta_{\mu\nu}$) :

$$T_{\mu\nu} = \begin{pmatrix} \rho & 0 & 0 & 0 \\ 0 & -p & 0 & 0 \\ 0 & 0 & -p & 0 \\ 0 & 0 & 0 & -p \end{pmatrix}, \tag{2.12}$$

where ρ and p are the energy density and the pressure of the fluid respectively. By considering the time and space component of Eq.(2.3), respectively, two equations are obtained :

$$H^2 = \left(\frac{\dot{a}}{a}\right)^2 = \frac{\zeta\rho}{3} - \frac{k}{a^2}, \tag{2.13}$$

$$\dot{H} = -\frac{\zeta}{2}(\rho + p) + \frac{k}{a^2}, \tag{2.14}$$

where $\zeta = 8\pi G$, H is the Hubble parameter, ρ and p denote the total energy density and pressure of all species present in the universe at a given epoch.

The Bianchi identities $G^{\mu\nu}_{;\nu} = 0 \Leftrightarrow T^{\mu\nu}_{;\nu} = 0$ stating the conservation of energy momentum, leads to :

$$\dot{\rho} + 3H(\rho + p) = 0. \tag{2.15}$$

It can also be derived from the first principle of thermodynamics. Eliminating the $\frac{k}{a^2}$ term from Eqs. (2.13) and (2.14) leads to :

$$\frac{\ddot{a}}{a} = -\frac{\zeta}{6}(\rho + 3p). \tag{2.16}$$

Considering that the deceleration parameter q is given by

$$q = -\frac{a\ddot{a}}{\dot{a}^2} = -\frac{\ddot{a}}{a} \cdot \left(\frac{a}{\dot{a}}\right)^2,$$

Eq. (2.16) states that the accelerating phase ($q < 0$) holds for :

$$\frac{\ddot{a}}{a} > 0 \Longleftrightarrow (\rho + 3p) < 0. \tag{2.17}$$

By introducing the dimensionless quantity

$$\Omega(t) = \frac{\rho(t)}{\rho_c(t)}$$

with $\rho_c(t) = \frac{3H^2(t)}{8\pi G}$, the critical density, Eq. (2.13) can be re-written as :

$$\Omega(t) - 1 = \frac{k}{a^2 H^2}. \tag{2.18}$$

Eq. (2.18) states that the matter content determines the spatial geometry of our universe :

$$\Omega < 1 \Longleftrightarrow \rho < \rho_c \qquad \text{for } k = -1 \text{ (open geometry)}, \tag{2.19}$$

$$\Omega = 1 \Longleftrightarrow \rho = \rho_c \quad \text{for } k = 0 \text{ (flat geometry)}, \tag{2.20}$$

$$\Omega > 1 \Longleftrightarrow \rho > \rho_c \qquad \text{for } k = +1 \text{ (closed geometry)}. \tag{2.21}$$

2.3 The evolution of an Universe filled with a perfect fluid

A universe filled with a perfect fluid is considered. In physics, a perfect fluid is a fluid that can be completely characterized by its rest frame energy density ρ and its pressure p. The equation of state of that universe is defined as :

$$\omega = \frac{p}{\rho}. \tag{2.22}$$

Recent observations (Spergel *et al.*, 2003) suggest that the universe has an almost flat geometry, i.e. $\Omega \simeq 1$. Solving the Einstein Eqs. (2.13) and (2.14) with k = 0 (flatness) and $\omega \neq -1$ (not a cosmological constant) brings, assuming $\omega = constant$:

$$H = \frac{2}{3(1+\omega)(t - t_0)}, \tag{2.23}$$

$$a(t) \propto (t - t_0)^{\frac{2}{3(1+\omega)}}, \tag{2.24}$$

$$\rho \propto a^{-3(1+\omega)}, \tag{2.25}$$

where t_0 is a constant. The radiation-dominated universe corresponds to $\omega = \frac{1}{3}$ and the dust dominated universe to $\omega = 0$. Both cases correspond to a decelerated phase of expansion of the universe :

$$a(t) \propto t^{\frac{1}{2}},\ \rho \propto a^{-4} \qquad \text{for the radiation-dominated universe}, \tag{2.26}$$

$$a(t) \propto t^{\frac{2}{3}},\ \rho \propto a^{-3} \qquad \text{for the dust dominated universe}. \tag{2.27}$$

Eq. (2.16) states that a phase of accelerated expansion of the universe ($\rho + 3p < 0$) occurs for an equation of state in a range given by

$$\omega < -\frac{1}{3}. \tag{2.28}$$

Chapter 3

Dark energy

3.1 Observational evidence for dark energy

The expansion of the universe implies that the wavelength of light is stretched as one looks deeper into space. The redshift, z, quantifies that effect. The redshift corresponds to the fractional change of the stretched wavelength :

$$z = \frac{\lambda_0 - \lambda_e}{\lambda_e}. \tag{3.1}$$

In other words :

$$1 + z = \frac{\lambda_0}{\lambda_e}, \tag{3.2}$$

where the index "e" and "0" are for the emitted and observed wavelengths, respectively. In FLRW, a similar relation also holds for the scale factor. Hence we have the relation :

$$1 + z = \frac{\lambda_0}{\lambda} = \frac{a_0}{a}. \tag{3.3}$$

Here the subscript "0" denotes the quantities at the present epoch.

3.1.1 The luminosity distance

The luminosity distance, d_L plays a very important role in astronomy and particularly in supernovae observations. The observed flux F at distance d from a source of known luminosity L_s is defined as :

$$F = \frac{L_s}{4\pi d^2} \tag{3.4}$$

since the total flux through a spherical shell with area $4\pi d^2$ is constant. Applied to an expanding universe, the luminosity distance, d_L is defined as :

$${d_L}^2 = \frac{L_s}{4\pi F}. \tag{3.5}$$

Working in comoving coordinates and considering an object with absolute luminosity L_s located at a coordinate distance χ_s from an observer at $\chi = 0$. The following derivations can be made (Copeland *et al.*, 2006). The radial light ray traveling along the χ direction satisfies the geodesic

equation $ds^2 = -dt^2 + a^2(t)d\chi^2 = 0$. Thus :

$$\chi_s = \int_0^{\chi_s} d\chi = \int_{t_1}^{t_0} \frac{dt}{a(t)} = \frac{1}{a_0 H_0} \int_0^z \frac{dx}{E(x)}, \tag{3.6}$$

where $E(z) = \frac{H(z)}{H_0}$ and using $\dot{z} = -(1+z)H$ from Eq. (3.3).

From the metric in (2.10), $A(t)$, the area of a sphere at any epoch can be deduced :

$$A(t) = 4\pi(a(t)S_k(\chi))^2. \tag{3.7}$$

Then at $t = t_0$, $A(t_0) = 4\pi(a_0 S_k(\chi))^2$ and the observed energy flux becomes :

$$F = \frac{L_0}{4\pi(a_0 S_k(\chi))^2} (= \frac{L_0}{A(t_0)}). \tag{3.8}$$

Substituting Eqs. (3.7) and (3.8) for Eq. (3.5), the luminosity distance in an expanding universe is then :

$$d_L = a_0 S_k(\chi_s)(1+z), \tag{3.9}$$

where χ_s is given in Eq.(3.6).

In terms of $\Omega_k = -\frac{k}{a^2 H^2}$, the scale factor at z = 0, a_0, can be expressed as :

$$a_0 = \frac{d_H}{\sqrt{|\Omega_k|}}, \tag{3.10}$$

where $d_H = \frac{c}{H_0}$ is the Hubble scale.

A dimensionless luminosity distance can be defined as :

$$d'_L = \frac{d_L}{d_H} = \frac{1+z}{\sqrt{|\Omega_k|}} S_k\left(\sqrt{|\Omega_k|} \int_0^z \frac{dx}{E(x)}\right), \tag{3.11}$$

the factor $\sqrt{|\Omega_k|}$ is removed in the case of a spatially flat geometry and :

$$E(z)^2 = \left(\frac{H(z)}{H_0}\right)^2 = \Omega_r(1+z)^4 + \Omega_m(1+z)^3 + \Omega_k(1+z)^2 + \Omega_{DE} \exp\left(\int_0^z 3\left[\frac{1+\omega_{DE}(x)}{1+x}\right] dx.\right). \tag{3.12}$$

Ω_i is used to denote the density of the i-th component (r-radiation, m-matter, DE-Dark Energy) in units of the critical density $\rho_c = \frac{3H^2}{8\pi G}$. In Eq. (3.12) the term for the DE is written in a very general form that allows for an arbitrarily time varying equation of state parameter ω_{DE}. As explained in section **4.2.2**, by fitting the theoretical curve of the luminosity distance to the observations of appropriate astronomical objects, it is possible to constrain some cosmological parameters.

3.1.2 Luminosity distances of Type Ia supernovae : The smoking gun

Astronomers usually measure the brightness of astronomical objects in units of apparent or absolute magnitude, respectively noted m and M. Both quantities are related to the luminosity distance d_L via the relation :

$$m - M = 5\log_{10}\left(\frac{d_L}{1Mpc}\right) + 25, \text{ M = Flux(distance = 10pc).} \tag{3.13}$$

It can be deduced from Eq.(3.4), considering that :

$$m_1 - m_2 = -2.5 \log_{10} \left(\frac{F_1}{F_2} \right), \tag{3.14}$$

where m_1 and m_2 are the apparent magnitudes of two distinct sources; F_1 and F_2 are their respective fluxes. The numerical factors arise from the astronomical conventions used in the definition of m and M. The dimensionless combination $(\frac{H_0 d_L}{c})$ rather than $d_L(z)$ is often used. Eq. (3.13) then changes to :

$$m(z) = \Xi + 5 \log_{10} \left(\frac{H_0 d_L(z)}{c} \right), \tag{3.15}$$

with the quantity Ξ being related to M by (Copeland *et al.*, 2006) :

$$\Xi = M + 25 + 5 \log_{10} \left(\frac{c H_0{}^{-1}}{1 Mpc} \right) = M - 5 \log_{10} h + 42.38. \tag{3.16}$$

The quantity Ξ and the other constants appearing in the previous equations do not fundamentally change the related physics.

It was the observation of luminosity distances of high redshift SNe Ia (Riess *et al.*, 1998; Perlmutter *et al.*, 1999) that brought the direct evidence for the accelerated phase of expansion of the universe. Since its onset, the most exciting observational development in studies of the Hubble expansion rate have undoubtedly been the measurements of the deceleration parameter $q = \frac{dH^{-1}}{dt} - 1 = \frac{\Omega_m}{2} - \Omega_\Lambda$. It has been repeatedly found negative through deep studies of the Hubble diagram of SNe Ia pioneered by the Supernova Cosmology Project (Perlmutter *et al.*, 1999) and the High-z Search Team (Riess *et al.*, 1998). The basic observation that set the ground for the idea of an accelerating universe was that Type Ia supernovae at $z \sim 0.5$ were $\Delta m \sim 0.25$ mag (corresponding to $10^{\Delta m/2.5} - 1 \sim 25\%$) fainter than would be expected for a decelerating universe such as the $\Omega_m = 1$ Einstein-deSitter model. This has been interpreted as implying that the expansion rate has been accelerating since then, implying that the observed SNe Ia are actually further away than expected.

In the above-mentioned observations, the choice of Type Ia supernovae was motivated by the fact that they seem to be equally intrinsically luminous at all redshifts, setting them as one good type of *standardizable candle*. As detailed in chapter **4**, SNe Ia are the brightest and most homogeneous class of supernovae, with hydrogen poor spectra and, even if a sound theoretical understanding of their underlying genesis is still lacking, a general concensus on their use as standardizable candles exists in the scientific community.

3.1.3 The age of the Universe

When the age of the universe (t_0) is compared to the age of the oldest stellar populations (t_s), it is consistent to require that $t_0 > t_s$. It was recently estimated that the age of globular clusters is $t_1 = 13.5 \pm 2\ Gyr$ (Jimenez *et al.*, 1996). Another method of dating applied to specific globular clusters (Richer *et al.*, 2002; Hansen *et al.*, 2002) estimated that age to be $t_1 = 12.7 \pm 0.7\ Gyr$. considering these results, a lower bound of $t_0 > 11 - 12\ Gyr$ can be set for the age of the universe.

A model of the universe with three components is considered : radiation ($\omega_r = \frac{1}{3}$), pressureless dust ($\omega_m = 0$) and dark energy in the form of a cosmological constant ($\omega_\Lambda = -1$) as suggested by the ΛCDM model. Assuming a FLRW background, Eq. (3.6) gives an expression for t_0 at any

redshift z :

$$H_0 t_0 = \int_0^{t_0} d\tau = \int_0^{\infty} \frac{dz}{(1+z)H(z)} = \int_0^{\infty} \frac{dx}{x\left[\Omega_r^{(0)} x^4 + \Omega_m^{(0)} x^3 + \Omega_\Lambda^{(0)} + \Omega_k^{(0)} x^2\right]^{\frac{1}{2}}}, \tag{3.17}$$

where $x = 1 + z$. $\Omega_r^{(0)}$, $\Omega_m^{(0)}$, $\Omega_k^{(0)}$ and $\Omega_\Lambda^{(0)}$ are respectively, the radiation, matter, curvature and dark energy density parameters as observed today. H_0 is the Hubble constant today.

The existence of high redshift galaxies with evolved stellar population, high redshift radio galaxies and the dating of high redshift QSOs (Alcaniz and Lima, 1999; Dunlop *et al.*, 1996; Dunlop, 1998; Krauss, 1997; Peacock *et al.*, 1998; Yoshii *et al.*, 1998) can threrefore be used in conjunction with Eq. (3.17) to constrain our knowledge of dark energy in the FLRW framework. Most of these observations require either $\Omega_\Lambda \neq 0$ or $\Omega_k > 0$ if they have to be consistent with

$$H_0 = 72 \pm 3 \pm 7 \ km\ s^{-1}\ Mpc^{-1}$$

or

$$H_0^{-1} = 9.776 h^{-1}\ Gyr,\ 0.64 < h < 0.80$$

with $h = \frac{H_0}{100\ km/s/Mpc}$; as obtained by the Hubble Space Telescope Key project (HKP) (Freedman *et al.*, 2001) where direct measurements of the distances to 18 nearby spiral galaxies (using Cepheid variables) were made. However, the interpretation of these observations at present requires fairly complex modeling and the prevalence of systematics (local peculiar motions to be corrected for in HKP and sensitivity of Cepheid calibration to metallicity for example) suggest that the present results are not totally water tight (Sarkar, 2007).

3.1.4 The Cosmic Microwave Background

Penzias and Wilson (1964) discovered the Cosmic Microwave Background (CMB) while determining the noise factor of a radiating horn at a wavelength of 7.35 cm. The study of cosmology was radically changed after that discovery. Several powerful groups of cosmologists, and particularly the Russian school led by Zeldovich and his colleagues in Moscow, and R.H. Dicke and his students in Princeton were at the forefront of the support of Penzias-Wilson's discovery as proving that the big bang idea was correct (Hoyle *et al.*, 2000).

The dominant paradigm in modern cosmology states that the universe became totally transparent to photons when the early universe recombined at $z_r \simeq 1089$ (Bennett *et al.*, 2003), moving from a tightly coupled photon-plasma rendered opaque by Compton scattering, to a neutral fluid of atoms. Since leaving the surface of last scattering - set at $z \simeq z_r$ - the photons have been traveling freely and randomly accross the universe, and some of them reach us today where we see them as the CMB, emitted when the universe was $\simeq$ 400 000 years old. The expansion of the universe has stretched their wavelength to such extent that they are observed in the (sub-)millimetric range of the electromagnetic spectrum.

Because the CMB radiation is supposedly emitted from an extremely hot phase of the evolution of the universe (the Big Bang), its spectrum is expected to be of a black body type. Observations by the COBE spacecraft in 1992 confirmed that the CMB has a very nearly black body spectrum (Mather *et al.*, 1990; Smoot *et al.*, 1990; Mather *et al.*, 1994) with a temperature today of $T_0 \simeq 2.725 \pm 0.001\ K$ (Fixsen and Mather, 2002). In addition, that temperature is the same in almost

every direction one looks i.e the background is highly isotropic. Today, both the black body spectrum and the isotropy of the radiation constitute two very strong arguments for the (Hot) Big Bang theory. The best measurements so far of the spectrum of this background have been obtained through the Wilkinson Microwave Anisotropy Probe (WMAP) in 2003. These measurements tell us about the thermal history of the universe and they provide a picture of the lumps of matter that were the seeds of the struture we observe today according to the gravitational instability theory.

The temperature fluctuations of the CMB sky have the strongest contrast (after removing the dipolar temperature anisotropy caused by the motion of the Local Group) for the patches with a typical angular size of $\simeq 1^{\circ}$. This typical scale is directly related to R_S, the sound horizon[1] in the tightly coupled baryon-photon fluid prior to the recombination phase (see next section).

As a result, the CMB is not perfectly isotropic. Temperature fluctuations of the order of $\frac{\Delta T}{T} \sim 10^{-5}$ are observed in the maps from COBE and WMAP. These temperature fluctuations are mostly related to density fluctuations at recombination ($z_r \simeq 1089$). A photon leaving an overdense region will lose a significant amount of its energy to overcome gravity and then reach us colder than before. On the opposite, a photon emitted by a region of lower density, will reach us warmer than the previous one. As illustrated in figure 3.1, it is known that the angular scale of any object depends on the geometry of the universe and the geometry depends on the mass content, which affects temperature fluctuations. Therefore, measuring temperature fluctuations corresponds to measuring the geometry of the universe, since R_S is essentially independent of curvature.

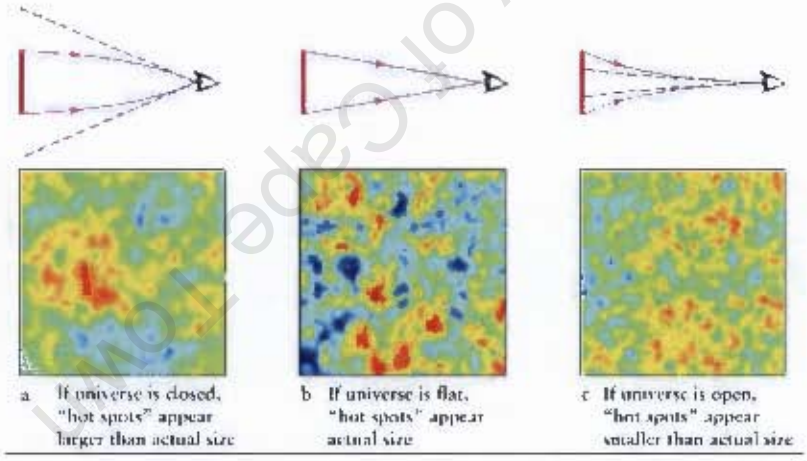

Figure 3.1: *Effect of the geometry of the universe on angular sizes. At a given redshift, the angular diameter D_A giving the size of the object on the sky is $D_A \propto \frac{S_k(\chi)}{\sqrt{\Omega_k}}$ and clearly depends on the curvature k. Measuring D_A at $z \sim 1000$ tells wether the universe is open ($k = -1$), flat ($k = 0$) or closed ($k = 1$). Source : (http://ircamera.as.arizona.edu/NatSci102/NatSci102/images/imagesize.jpg)*

The most fundamental statistics to measure from the observed sky map by WMAP is its angular power spectrum, C_l, which measures the variance of the temperature fluctuations over a range of angular scales (Hinshaw, 2000; Hinshaw *et al.*, 2003). The multipole moment l in the angular power spectrum is related to the angular scale Θ by $l \propto \frac{100}{\Theta}$. There exists an approximate analytical expression on how the position of the first acoustic peak in the angular power spectrum depends on the background distribution of energy densities between matter and a cosmological constant (Weinberg, 2000). By constraining the curvature of the universe to be $|\Omega_k| = 0.030^{-0.026}_{-0.025} \ll 1$

[1]The sound horizon is the distance a sound wave can travel in the time between the Big Bang and the surface of last scattering set at the time of recombination

(Page *et al.*, 2003), the position of the first acoustic peak around $l = 200$, as seen in figure 3.2, corroborates the necessity of a non-zero density parameter for the cosmological constant Ω_Λ. Here, a necessary word of caution is that the constraint on Ω_Λ is not strong when only the CMB data are considered. Figure 3.4 illustrates some of the confidence levels reached so far in combining CMB with other cosmological tests.

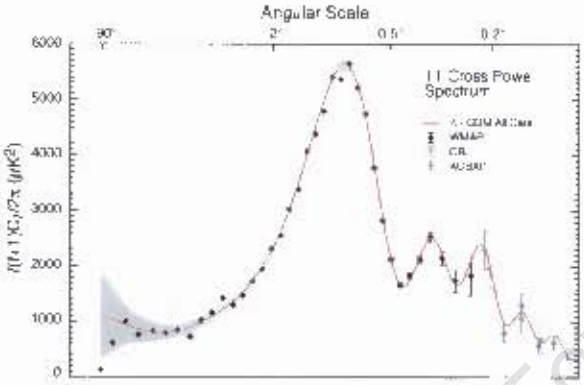

Figure 3.2: *Angular power spectrum of temperature fluctuations obtained with WMAP and other small scale CMB experiments. The position of the first peak gives an indication on the geometry of the universe. Source : (Spergel* et al., *2003).*

3.1.5 The Large Scale Structure clustering

The acoustic waves that gave rise to the peaks seen in the CMB temperature fluctuations power spectrum also affected the power spectra of matter and galaxies. It is generally admitted that the early universe consisted of a homogeneous plasma of electrons, protons, neutrons, dark matter, photons and neutrinos. Due to quantum fluctuations during inflation, very small perturbations arose, inducing slightly denser regions. Perturbations in radiation oscillates because of the forces competing being the radiation pressure and gravity (Dodelson, 2003). The tight coupling between electrons and photons due to Thompson scattering then caused the baryons to move in unison with the radiation, inducing then the combined oscillation of that primordial fluid.

At decoupling, the sound speed of the baryonic medium drops to almost zero since the perturbation stalls at a characteristic distance. As the dark matter content determines the mass profile of the (gravitational) perturbation, it will exhibit a small excess at this characteristic distance. After decoupling, baryons started to fall back onto the CDM density peak that has grown significantly since the matter-radiation equality (Hutsi, 2006) [2]. The effect of the above mentioned excess, in the present-day universe, is the existence of a characteristic length scale, approximately 150 Mpc, of the large-scale structure. An effect quantified by a peak in the two-point correlation function (figure 3.3) of galaxy distribution at roughly 150 Mpc (in comoving scale), corresponding to oscillating features in the matter power spectrum known as Baryon Acoustic Oscillations (BAO).

BAO have been recently confirmed by the analysis of the spatial clustering of the Sloan Digital Sky Survey (SDSS) Luminous Red Galaxy (LRG) sample (Eisenstein *et al.*, 2005) (who determined the two-point correlation function) and more recently by (Hutsi, 2006) (who determined both the power spectrum and the two-point correlation function). (Cole et al., 2005) have similarly detected

[2] A pedagogical example of the whole process has been developed by D. Eisenstein at http://cmb.as.arizona.edu/~acousticpeak/. It is based on an original work by Bashinsky & Bertschinger, 2002

acoustic oscillations in the power spectrum from the 2dF galaxy sample. (Eisenstein *et al.*, 2005) provide clear evidence for the acoustic peak at a 3.4σ confidence level. Their best fit of the large-scale redshift-space correlation function of the SDSS LRG sample, using a χ^2 method, requires a non-zero dark energy component and their measurement of matter density parameter Ω_m matches the CMB findings. It also improves the constraints on Ω_k.

CMB and Large Scale Structure clustering : The connection

In defining a standard ruler using the SDSS LRG sample, Eisenstein et al., 2005 introduced a H_0-independent distance to $z_1 = 0.35$ (typical redshift of the SDSS LRG sample) as :

$$A = \frac{\sqrt{|\Omega_m|}}{E(z_1)^{\frac{1}{3}}} \left[\frac{1}{z_1 \sqrt{|\Omega_k|}} S_k \left(\sqrt{|\Omega_k|} \int_0^{z_1} \frac{dz}{E(z)} \right) \right]^{\frac{2}{3}}, \tag{3.18}$$

where S_k and $E(z)$ are given by Eqs.(2.9) and (3.12) respectively.

The factors Ω_k are removed for a flat universe. In its simplest form, well constrained by their data, Eq. (3.18) can be re-written as :

$$A = D_V(0.35) \frac{\sqrt{\Omega_m H_0^2}}{0.35c}, \tag{3.19}$$

with :

$$D_V(z) = \left[D_M(z)^2 \frac{cz}{H(z)} \right]^{\frac{1}{3}}, \tag{3.20}$$

where $D_M(z)$ is the redshift-dependent comoving angular diameter distance.

Likelihood contours of CDM models as function of $\Omega_m h^2$ and $D_V(0.35)$ were used. By marginalising these contours, they obtained $D_V(0.35) = 1370 \pm 64$ Mpc (4.7%) and then deduced a value of A , from Eq.(3.19) to be $A = 0.469 \pm 0.017$ (3.6%). Tegmark *et al.* (2004) give an estimate for $D_M(1089)$, the comoving angular diameter distance to the surface of last scattering. One way to calculate it is by determining the so-called shift parameter I, obtained using the WMAP data and defined (Knop *et al.*, 2003; Ichikawa and Takahashi, 2005) as :

$$I = \frac{\sqrt{\Omega_m}}{\sqrt{|\Omega_k|}} S_k \left(\sqrt{|\Omega_k|} \int_0^{z_r} \frac{dz}{E(z)} \right). \tag{3.21}$$

An estimate for I has been obtained using the best fit for the so-called WMAPext dataset (Spergel *et al.*, 2003). That best fit was obtained by assuming a flat universe and priors on non-zero density parameters for the cosmological constant Ω_Λ and the matter content Ω_m of the universe, today.

In the SDSS LRG sample, Eisenstein *et al.* (2005) measure - with $D_V(0.35)$, then A - the acoustic peak scale to just better than 4%. Comparing their result to the angular scale of the CMB anisotropies gave them the distance ratio $R_{0.35} = \frac{D_V(0.35)}{D_M(1089)} = 0.0979 \pm 0.0036$. Since the comoving length scales of BAO appearing in the SDSS LRG Galaxy power spectrum do not change after recombination, the ratio R_{z_1} therefore sets them as a possible CMB calibrated standard ruler to measure the angular diameter distance and Hubble parameter as functions of redshift.

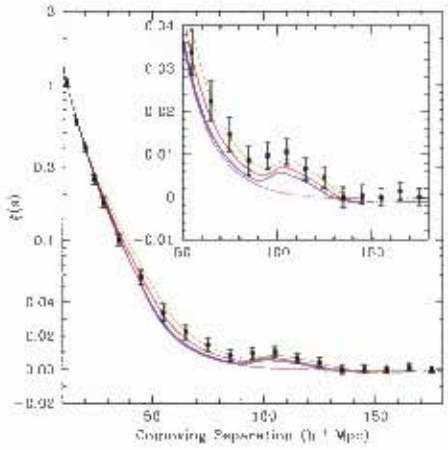

Figure 3.3: *The peak in the two-point correlation function of galaxy distribution at roughly 150 Mpc (in comoving scale) corresponds to oscillating features in the matter distribution power spectrum known as baryon acoustic oscillations (BAO) . Source : (Eisenstein* et al., *2005).*

on

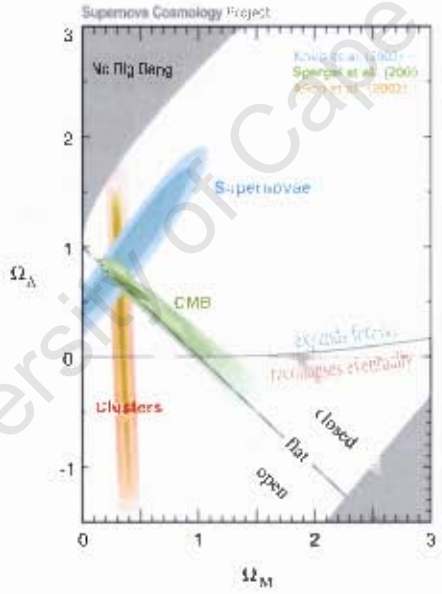

Figure 3.4: *Confidence contours on the true values of cosmic parameters. Here are plotted confidence contours for Ω_M and Ω_Λ obtained from three independent cosmological tests: Type Ia supernovae, CMB and clustering of galaxies. $(\Omega_M, \Omega_\Lambda) = (1, 0)$, the flat universe without a cosmological constant is ruled out by the combined three cosmological tests at high significance. Source : (Supernova Cosmology Project : http://supernova.lbl.gov/)*

3.2 Λ : The cosmological constant

In 1917, Einstein (helped by the French mathematician E. Cartan) introduced the cosmological constant Λ in the field equation (2.3) with the motivation that it would allow for a static, closed and finite universe in which the energy density of matter determines the geometry. The first challenge to that approach was introduced when de Sitter (1917) produced a solution to Einstein's equations

(2.3) with cosmological constant and no matter (de Sitter, 1917). The cosmological constant was hereafter dropped with the evidence for the expansion of the universe brought by (Hubble, 1929).

3.2.1 Introduction of Λ

When Einstein obtained the equations of general relativity in 1915, a first roadblock was that the final models of the universe were homogeneous and isotropic but not static. The cosmological constant can be introduced from a straightforward mathematical reasoning. In Eq. (2.3), the metric $g_{\mu\nu}$ behaves as a constant with respect to covariant derivatives. And because $G_{\mu\nu}$ and $T_{\mu\nu}$ satisfy respectively the Bianchi identities $G^{\mu\nu}_{;\nu} = 0$ and energy conservation $T^{\mu\nu}_{;\nu} = 0$, there is a freedom to add a cosmological constant term Λ under the form $\Lambda g_{\mu\nu}$ in the equations without affecting energy conservation. The modified Einstein equations therefore are given by :

$$G_{\mu\nu} = R_{\mu\nu} - \frac{1}{2}g_{\mu\nu}R + \Lambda g_{\mu\nu} = 8\pi G T_{\mu\nu}, \tag{3.22}$$

in units where c = 1. In the FLRW background given by Eq.(2.4) the modified Einstein equations give :

$$H^2 = \left(\frac{\dot{a}}{a}\right)^2 = \frac{\zeta\rho}{3} - \frac{k}{a^2} + \frac{\Lambda}{3}. \tag{3.23}$$

$$\frac{\ddot{a}}{a} = -\frac{\zeta}{6}(\rho + 3p) + \frac{\Lambda}{3}. \tag{3.24}$$

A sphere with comoving radial coordinate r is considered. It has a physical radius ar if curvature effects are neglected. Using Eq.(3.24), a test particle with mass m at the boundary of the sphere will accelerate as space evolves as (Bergstrom and Goobar, 2006) :

$$\frac{d^2(ar)}{dt^2} = -\frac{\zeta\rho}{6}(ar) + \frac{\Lambda}{3}(ar). \tag{3.25}$$

The mass, M of the sphere is defined as $M = \frac{4\pi(ar)^3}{3}\rho$, substituting M in Eq.(3.25) gives :

$$\frac{d^2(ar)}{dt^2} = -\frac{GM}{(ar)^2} + \frac{\Lambda}{3}(ar). \tag{3.26}$$

The first term in the right-hand side of Eq.(3.26) is the familiar Newtonian (attractive) force. The second term shows that the force associated with the cosmological constant is repulsive.

Setting $a = const$, $k = 1$ and $\Lambda = 0$ brings $H = \frac{\dot{a}}{a} = 0 = \frac{\ddot{a}}{a}$; Eqs.(3.23) and (3.24) give :

$$\rho = -3p = \frac{3k}{8\pi G a^2}. \tag{3.27}$$

Eq.(3.27) is the first roadblock experienced by Einstein in his initial approach : no homogeneous isotropic model of the universe with $\rho > 0$ is possible under Einstein's initial assumption of a static (and closed) universe. As also later envisaged by Einstein, in the case of a dust(matter)-dominated universe ($p = 0$), Eqs.(3.23) and (3.24) state that Einstein's static universe corresponds to :

$$\rho = \frac{\Lambda}{4\pi G}, \quad \frac{k}{a^2} = \Lambda. \tag{3.28}$$

$\rho > 0$ corresponds to $\Lambda > 0$ (i.e $k > 0$) meaning that the static universe is a closed one ($k = 1$) with a radius of curvature a given by :

$$a = \sqrt{\frac{k}{\Lambda}} = \sqrt{\frac{1}{\Lambda}} = \sqrt{\frac{1}{4\pi G\rho}}. \tag{3.29}$$

Eq.(3.29) states that the larger the value of ρ, the smaller the radius of curvature a, with the energy density ρ determined by Λ. Already during Einstein's epoch the question of how big could Λ be was implicit, assuming that it is a given universal constant like G. That implicit difficulty resurfaced later in the 20^{th} century under the heading of the "cosmological constant problem".

3.2.2 "The cosmological constant problem"

The *smallness* of the cosmological constant is one of the most challenging difficulty in modern theoretical physics. The full (modified) Einstein's field equations are given by :

$$R_{\mu\nu} - \frac{1}{2}g_{\mu\nu}R + \Lambda g_{\mu\nu} = 8\pi G T_{\mu\nu}. \tag{3.30}$$

The cosmological term can be moved over to the right-hand side of the equation and leads to :

$$R_{\mu\nu} - \frac{1}{2}g_{\mu\nu}R = 8\pi G\left(T_{\mu\nu} + T^{\Lambda}_{\mu\nu}\right), \tag{3.31}$$

where $T^{\Lambda}_{\mu\nu} = -\frac{\Lambda}{8\pi G}g_{\mu\nu}$. In a local free-fall frame comoving with the fluid (i.e $g_{\mu\nu} = \eta_{\mu\nu}$), $T^{\Lambda}_{\mu\nu}$ acts like a contribution to the energy-momentum tensor of the form :

$$T^{\Lambda}_{\mu\nu} = \begin{pmatrix} \rho_\Lambda & 0 & 0 & 0 \\ 0 & -\rho_\Lambda & 0 & 0 \\ 0 & 0 & -\rho_\Lambda & 0 \\ 0 & 0 & 0 & -\rho_\Lambda \end{pmatrix}, \tag{3.32}$$

where $\rho_\Lambda = \frac{\Lambda}{8\pi G}$ can be defined as the vacuum energy density. In units where $c = 1 = \hbar$, the Planck mass is $m_{pl} = G^{-\frac{1}{2}} = 1.22 \times 10^{19}$ GeV where G is Newton's gravitational constant. ρ_Λ can be re-written as $\rho_\Lambda = \frac{\Lambda m_{pl}^2}{8\pi}$.

Observations suggest that today $\frac{\Lambda}{3H_0^2} = \Omega_\Lambda^0 \sim 1$ i.e. $\Lambda \sim H_0^2 = (2.13h \times 10^{-42}GeV)^2$. This corresponds to a vacuum density ρ_Λ :

$$\rho_\Lambda \sim 10^{-47}GeV^4. \tag{3.33}$$

Meanwhile the *vacuum energy density,* ρ_{vac} , evaluated by the *sum of zero-point energies of quantum fields with mass* m is given by (Copeland *et al.*, 2006) :

$$\rho_{vac} = \frac{1}{2}\int_0^\infty \frac{d^3\mathbf{k}}{(2\pi)^3}\sqrt{k^2+m^2} = \frac{1}{4\pi^2}\int_0^\infty dk\ k^2\sqrt{k^2+m^2}, \tag{3.34}$$

where k denotes a Fourier mode.

$\frac{1}{4\pi^2}\int_0^\infty dk\ k^2\sqrt{k^2+m^2} \sim \frac{1}{4\pi^2}\int_0^\infty dk\ k^3$ for finite mass m. The integral in Eq.(3.34) should diverge as $k \longrightarrow \infty$ except if there is a cut-off scale k_{max} somewhere between 0 and ∞. The latter is the meaning of the assumption that near the Planck (energy) scale m_{pl}, conventional field theory

breaks down, i.e. one can expect quantum field to be valid up to some cut-off scale k_{max} where

$$\rho_{vac} \simeq \frac{k_{max}^4}{16\pi^2}.$$

Hence if it is assumed that $k_{max} \simeq m_{pl}$, the vacuum energy density is estimated to be

$$\rho_{vac} \simeq 10^{74} GeV^4,$$

which is about 10^{120} orders of magnitude larger than the observed estimate given by Eq.(3.33). This is known as the "cosmological constant problem".

Because, from quantum theory, the vacuum energy density ρ_{vac} is proportional to the Planck constant $\hbar$, it is assumed that the cosmological constant problem is above the framework of classical physics, where $\hbar \longrightarrow 0$. A relevant framework being generally considered is the one unifying general relativity and quantum fields, such as is attempted in string theory. Early in the eighties, supersymmetry was proposed as a way to cancel the cosmological constant, considering the possibility for given elementary particles to yield opposite contribution that could bring the integral in Eq.(3.34) to zero. However, with supersymmetry said to break down around $10^3 GeV$, a clear solution to the cosmological constant problem is still unavailable (Copeland *et al.*, 2006). Details on these aspects can be found in (Bergstrom and Goobar, 2006).

3.3 Scalar field models of dark energy

With the cosmological problem still unsolved , many approaches have flourished on the dark energy issue. The common strategy consists in inferring that the cosmological constant is zero for some as yet unknown mechanisms and explore the possibility that ω, the equation of state of dark energy changes with time (redshift). Most of the models derived from that strategy strongly rely on scalar fields. Two such lagrangians are (Padmanabhan, 2003) :

$$L_{quin} = \frac{1}{2}\partial_\alpha\phi\partial^\alpha\phi - V(\phi), \tag{3.35}$$

$$L_{tach} = -V(\phi)\left[1 - \partial_\alpha\phi\partial^\alpha\phi\right]^{\frac{1}{2}}, \tag{3.36}$$

Where L_{quin} and L_{tach} denote the Lagrangian for quintessence and tachyon, respectively. Quintessence and tachyon are two types of scalar fields[3] $\phi = \phi(x,t)$. $V(\phi)$, the potential of the field, is an arbitrary function.

3.3.1 Quintessence

The lagrangian L_{quin} is a natural generalization of the lagrangian for a non-relativistic particle,

$$L = \frac{1}{2}(\dot{q})^2 - V(q)$$

where $q = q(t)$ denotes the position. The action S associated to a quintessence field is given by :

$$S = \int d^4x\sqrt{-g}\left[\frac{1}{2}\partial_\alpha\phi\partial^\alpha\phi - V(\phi)\right], \tag{3.37}$$

[3]A scalar field is a function of space and time, meaning that it contains an infinite number of degrees of freedom.

with $\partial_\alpha\phi\partial^\alpha\phi = g_{\alpha\beta}\partial^\beta\phi\partial^\alpha\phi$ and $\alpha, \beta = 0, 1, 2, 3$.

In a local free-fall frame comoving with the fluid (i.e $g_{\mu\nu} = \eta_{\mu\nu}$), the energy density ρ_ϕ and pressure density p_ϕ of the scalar field are given by :

$$\rho_\phi = \frac{1}{2}\left(\dot{\phi}\right)^2 + V(\phi),\ p_\phi = \frac{1}{2}\left(\dot{\phi}\right)^2 - V(\phi). \tag{3.38}$$

The time dependent equation of state ω_ϕ for the field ϕ is therefore :

$$\omega_\phi = \frac{p_\phi}{\rho_\phi} = \frac{(\dot{\phi})^2 - 2V(\phi)}{(\dot{\phi})^2 + 2V(\phi)}. \tag{3.39}$$

Substituting Eqs.(3.38) in the energy conservation equation $\dot{\rho} + 3H(\rho + p) = 0$ leads to :

$$\ddot{\phi} + 3H\dot{\phi} + \frac{\partial V}{\partial \phi} = 0, \tag{3.40}$$

which is the Klein-Gordon equation, governing the time evolution of a scalar field in a potential $V(\phi)$. From the ratio $\frac{\ddot{a}}{a}$, it appears that in these models, the accelerated phase of the universe occurs for $(\dot{\phi})^2 < V(\phi)$. It is also worth noting that the equation of state for the field ϕ varies in the range $-1 \leq \omega \leq 1$ and that the slow-roll limit, $(\dot{\phi})^2 \ll V(\phi)$, corresponds to $\omega_\phi \sim -1$, similar to the case of a cosmological constant.

In a flat FLRW spacetime (k = 0), the relation

$$\dot{H} = -4\pi G\dot{\phi}^2$$

can be derived from Eq. (2.14), hence a way to express $V = V(\phi)$ and ϕ in terms of H and $\dot{H}$ (Copeland *et al.*, 2006) :

$$V = \frac{3H^2}{8\pi G}\left(1 + \frac{\dot{H}}{3H^2}\right), \tag{3.41}$$

$$\phi = \int dt \left[-\frac{\dot{H}}{4\pi G}\right]^{\frac{1}{2}}. \tag{3.42}$$

The investigation of specific potentials brings a variety of quintessence models, most of them relying on potential energy of a scalar field to lead to the late time observed acceleration of the universe. Along that line of thought, models with power-law type of growth for the scale factor are of interest: $a(t) \propto t^p$ with $p > 1$ for an accelerated expansion. They are generally obtained via exponential type of potentials (i.e $V(\phi) \propto e^\varphi$) that possess the so called cosmological *scaling solutions* in which the *field energy density (ρ_ϕ) is proportional to the dominant background energy density ($\rho_{background}$)*. Also of interest is the fact that scalar fields potential that are not steep compared to exponential potentials can lead to an accelerated expansion (Copeland *et al.*, 2006).

3.3.2 Tachyon field

In Eq.(3.36), L_{tach} is a simple type of more general lagrangians associated with so-called tachyon fields. Its structure can be understood by a simple analogy from special relativity :

$$L = -m\sqrt{1 - (\dot{q})^2}$$

is the lagrangian describing a relativistic particle with (one dimensional) position q(t) and mass m. A field theory can be constructed by upgrading q(t) to a field depending both on space and time $[\phi = \phi(t, \mathbf{x})]$, $(\dot{q})^2$ to be replaced by $\partial_i \phi \partial^i \phi$ and the mass parameter m by a function of ϕ, say, $V(\phi)$. The lagrangian is then

$$L = -V(\phi_L) \left[1 - \partial_i \phi_L \partial^i \phi_L\right]^{\frac{1}{2}}$$

where $V(\phi_L)$ is the tachyon potential (Copeland *et al.*, 2006).

In a FLRW spacetime, the energy density ρ and the pressure density p are given by (Copeland *et al.*, 2006) :

$$\rho = \frac{V(\phi)}{\sqrt{1 - (\dot{\phi})^2}}, \tag{3.43}$$

$$p = -V(\phi)\sqrt{1 - (\dot{\phi})^2}. \tag{3.44}$$

Combining Eq. (2.16) and the energy conservation equation (2.15) gives :

$$\frac{\ddot{a}}{a} = \frac{8\pi G V(\phi)}{3\sqrt{1 - (\dot{\phi})^2}} \left(1 - \frac{3}{2}(\dot{\phi})^2\right), \tag{3.45}$$

which shows that in this model, the accelerated expansion phase occurs for $(\dot{\phi})^2 < \frac{2}{3}$.

The equation of state of the tachyon field is :

$$\omega_\phi = \frac{p}{\rho} = (\dot{\phi})^2 - 1. \tag{3.46}$$

Using Eqs.(2.16) and (3.45) brings $\frac{\dot{H}}{H} = -\frac{3}{2}(\dot{\phi})^2$ and an expression for $V(\phi)$ and ϕ in terms of H and $\dot{H}$ is :

$$V = \frac{3H^2}{8\pi G}\left(1 + \frac{2\dot{H}}{3H^2}\right)^{\frac{1}{2}}, \tag{3.47}$$

$$\phi = \int dt \left(-\frac{2\dot{H}}{3H^2}\right)^{\frac{1}{2}}. \tag{3.48}$$

A power-law expression for the scale factor, $a(t) \propto t^p$, requires a tachyon potential having an inverse square power-law, $V(\phi) \propto \phi^{-2}$. Scalar-fields potentials that are not steep compared to $V(\phi) \propto \phi^{-2}$ can also lead to an accelerated expansion (Copeland *et al.*, 2006).

3.3.3 Phantom (Ghost) field

Today, ω, the equation of state parameter is estimated to be $\omega = -0.98 \pm 0.12$ (Spergel *et al.*, 2003) when making various combinations of WMAPext data, supernonae observations and large scale structure data. Of interest is that $\omega \geq -1$ for the above discussed scalar fields models. Phantom (Ghost) dark energy is said to be the driver of the expansion for the region where $\omega < -1$. That phantom dark energy is said to arise from a scalar field with a negative kinetic energy and defines a (phantom) field with an action given by (Copeland *et al.*, 2006) :

$$S = \int d^4x\sqrt{-g}\left[-\frac{1}{2}\partial_\alpha \phi \partial^\alpha \phi - V(\phi)\right]. \tag{3.49}$$

A mathematical treatment similar to the one for quintessence models lead to an energy density ρ and pressure density p given by $\rho = \frac{-(\dot{\phi})^2}{2} + V(\phi)$ and $p = \frac{-(\dot{\phi})^2}{2} - V(\phi)$. The equation of state parameter is then :

$$\omega = \frac{p}{\rho} = \frac{(\dot{\phi})^2 + 2V(\phi)}{(\dot{\phi})^2 - 2V(\phi)}, \tag{3.50}$$

$\dot{\phi} = 0$ leads to $\omega_\phi = -1$.

3.3.4 K-Essence

K-Essence models were developed on the basic idea that the accelerated expansion of the universe could arise from modifications to the kinetic energy of the scalar field. The most general scalar field action governing these models is given by (Copeland *et al.*, 2006) :

$$S = \int d^4x\sqrt{-g}\cdot p(\phi, X), \tag{3.51}$$

where $X = \partial_\alpha\phi\partial^\alpha\phi = g_{\alpha\beta}\partial^\beta\phi\partial^\alpha\phi$ with $\alpha, \beta = 0, 1, 2, 3$ and p is an arbitrary function. This can lead to acceleration and scaling solutions.

3.3.5 Chaplygin gas

It is also possible to imagine, dark energy models involving an ideal type of fluid (Chaplygin gas) having an equation of state (Kamenshchik *et al.*, 2001) :

$$p = -\frac{A}{\rho}, \tag{3.52}$$

where A is a positive constant. From the equation of continuity

$$\dot{\rho} + 3H(\rho + p) = 0,$$

an expression for ρ is :

$$\rho = \sqrt{A + \frac{B}{a^6}}, \tag{3.53}$$

where B is a constant. Asymptotic patterns are :

$$\rho \sim \frac{\sqrt{B}}{a^3} \quad \text{if } a \ll (\frac{B}{A})^{\frac{1}{6}}, \tag{3.54}$$

$$\rho \sim -p \sim \sqrt{A} \quad \text{if } a \gg (\frac{B}{A})^{\frac{1}{6}}. \tag{3.55}$$

Early in time, when a is small, the Chaplygin gas behaves as a pressureless dust. In late times, it behaves like a cosmological constant, thus leading to an accelerated phase of expansion of the universe.

A potential V can be associated to the chaplygin gas by approaching it as an ordinary scalar field ϕ where the energy density $\rho = \frac{(\dot{\phi})^2}{2} + V(\phi)$ and the pressure density $p = \frac{(\dot{\phi})^2}{2} - V(\phi)$. Therefore using Eqs.(3.52) and (3.53)gives :

$$(\dot{\phi})^2 = \frac{B}{a^6\sqrt{A + \frac{B}{a^6}}}, \tag{3.56}$$

$$V = \frac{1}{2}\left[\sqrt{A + \frac{B}{a^6}} + \frac{A}{\sqrt{A + \frac{B}{a^6}}}\right]. \tag{3.57}$$

Using the relation $H = \left(\frac{8\pi\rho}{3m_{pl}^2}\right)^{\frac{1}{2}}$, Eq.(3.56) can be re-written as :

$$\frac{\kappa}{\sqrt{3}}\frac{d\phi}{da} = \frac{\sqrt{B}}{a\sqrt{Aa^6 + B}}, \tag{3.58}$$

where $\kappa^2 = 8\pi G = 8\pi(m_{pl})^{-2}$. An integration leads to :

$$a^6 = \frac{4Be^{2\sqrt{3}\kappa\phi}}{A\left(1 - e^{2\sqrt{3}\kappa\phi}\right)^2}. \tag{3.59}$$

When substitued in Eq.(3.57), a potential V corresponding to a Chaplygin gas is (Copeland *et al.*, 2006) :

$$V(\phi) = \frac{\sqrt{A}}{2}\left(\cosh(\sqrt{3}\kappa\phi) + \frac{1}{\cosh(\sqrt{3}\kappa\phi)}\right). \tag{3.60}$$

3.4 General case : Scalar field models in the presence of a barotropic perfect fluid

In physics, a perfect fluid is a fluid that can be completely characterized by its rest frame energy density ρ and its pressure p. A barotropic fluid is defined as that state of a fluid for which the density parameter ρ_m is function of only the pressure p_m : $\omega_m = \frac{p_m}{\rho_m}$. In the present case, simultaneously to the presence of a barotropic fluid, the existence of a scalar field ϕ with an equation of state $\omega_\phi = \frac{p_\phi}{\rho_\phi}$ is assumed. The aim is to have a model where during the radiation and matter dominated eras, the energy density of the scalar field remains subdominant and emerges only at late times to drive the current observed accelerating phase of expansion of the universe. Therefore, from Eqs.(2.13) and (2.14) and in the case of a flat ($k = 0$) FLRW spacetime :

$$H^2 = \left(\frac{\dot{a}}{a}\right)^2 = \frac{\zeta}{3}(\rho_\phi + \rho_m), \tag{3.61}$$

$$\dot{H} = -\frac{\zeta}{2}\left(\rho_\phi + p_\phi + \rho_m + p_m\right). \tag{3.62}$$

The continuity equation (2.15) becomes :

$$\dot{\rho_\phi} + 3H(1 + \omega_\phi)\rho_\phi = 0, \tag{3.63}$$

$$\dot{\rho_m} + 3H(1 + \omega_m)\rho_m = 0. \tag{3.64}$$

Cosmological scenarios characterized by the relation

$$\frac{\rho_\phi}{\rho_m} = C, \tag{3.65}$$

with C a non-zero constant are called *"scaling solutions"*, because in such a case, the energy density of the scalar field "mimics" the background fluid density. Exponential potentials are of particular

interest because they give rise to such cosmological scenarios. One such solution is an attractor in state space and whatever the initial conditions, the field will enter the scaling regime at a certain point. To leave that scaling regime and give rise to the observed late time acceleration, the field potential should have a slope shallower at late time compared to the corresponding one during the scaling phase (Copeland *et al.*, 2006). Barreiro *et al.* (2000); Sahni and Wang (2000) can be consulted for additional details.

3.4.1 Dynamical systems for scalar field dark energy models

Dynamical systems methods allow a qualitative description of the evolution of any system described by a first order linear differential equation of the type :

$$\dot{X} = A \cdot X \Longleftrightarrow \dot{X} = f(X), \tag{3.66}$$

where A is the matrix associated to the vector field f. " $\cdot$ " $\equiv \frac{d}{d\tau}$, where τ is any suitable parameter. It is often convenient to take as parameter for the dynamics of dark energy $\tau = ln(a)$, *the number of e-foldings* where a is the scale factor. The dynamical systems method approach leads to investigating the behavior of the vector field f around equilibrium (fixed) points. The approach is briefly illustrated below with quintessence models.

The density for a quintessence scalar field ϕ with a potential $V(\phi)$ is :

$$\rho_\phi = \frac{1}{2}\epsilon(\dot{\phi})^2 + V(\phi), \tag{3.67}$$

where $\epsilon = +1$ for an ordinary (quintessence) scalar field. Eqs.(3.61), (3.62) and (3.63) read :

$$H^2 = \frac{\kappa^2}{3}\left[\frac{1}{2}\epsilon\dot{\phi}^2 + V(\phi) + \rho_m\right], \tag{3.68}$$

$$\dot{H} = -\frac{\kappa^2}{2}\left[\epsilon\dot{\phi}^2 + (1+\omega_m)\rho_m\right], \tag{3.69}$$

$$\epsilon\ddot{\phi} + 3H\dot{\phi} + \frac{dV}{d\phi} = 0, \tag{3.70}$$

where $\kappa^2 = 8\pi G = 8\pi(m_{pl})^{-2}$. (Copeland *et al.*, 1998; S. C. C. Ng and Rosati, 2001) introduce the following dimensionless quantities :

$$x = \frac{\kappa\dot{\phi}}{\sqrt{6}H},\ y = \frac{\kappa\sqrt{V}}{\sqrt{3}H},\ \lambda = -\frac{V_{,\varphi}}{\kappa V},\ \Gamma = \frac{VV_{,\varphi\varphi}}{V_{,\varphi}^2}, \tag{3.71}$$

where $V_{,\varphi} = \frac{dV}{d\varphi}$. The autonomous forms associated to equations (3.68), (3.69) and (3.70) are :

$$\frac{dx}{dN} = -3x + \frac{\sqrt{6}}{2}\epsilon\lambda y^2 + \frac{3}{2}x\left[(1-\omega_m)\epsilon x^2 + (1+\omega_m)\left(1-y^2\right)\right], \tag{3.72}$$

$$\frac{dy}{dN} = -\frac{\sqrt{6}}{2}\lambda xy + \frac{3}{2}x\left[(1-\omega_m)\epsilon x^2 + (1+\omega_m)\left(1-y^2\right)\right], \tag{3.73}$$

$$\frac{d\lambda}{dN} = -\sqrt{6}\lambda^2(\Gamma - 1)x, \tag{3.74}$$

with a constraint equation given by :

$$\epsilon x^2 + y^2 + \frac{\kappa^2 \rho_m}{3H^2} = 1. \tag{3.75}$$

Here, an effective equation of state ω_{eff} is defined as :

$$\omega_{eff} = \frac{p_\phi + p_m}{\rho_\phi + \rho_m}, \tag{3.76}$$

and an accelerated phase of expansion of the universe occurs for $\omega_{eff} < -\frac{1}{3}$. From the autonomous system, a study of the stability around the equilibrium (fixed) points is then performed for given potentials $V(\phi)$ (Copeland *et al.*, 2006).

Chapter 4

Type Ia supernovae

4.1 Generalities on supernovae

4.1.1 A bit of history

The word supernova as from its latin origin - *novae* - indicates something new appearing in the sky. In modern scientific language, supernovae are *stellar explosions* during which a large fraction of the progenitor's outer layers are blown off at high speed (the ejecta). These stellar explosions are very energetic events with an energy output of order the host galaxy's. The convention in naming supernovae requires that their denomination begins with SN, followed by the year of observation, then a letter indicating the rank of that discovery in the chronology of supernovae discovery for the given year (e.g. the first supernova discovered in 1987 is designated by SN 1987A). Early in the 20^{th} century, Baade and Zwicky were the first to attempt systematic studies of supernovae (Zwicky and Baade, 1934). Late in the 70's, with still a handful of homogeneous sets of data, the existence of different types of supernovae was becoming evident. The sub-class of SNe known as Type Ia supernovae is the most important for the present work.

4.1.2 From cepheids to SNe Ia

The ideal standard candle to be used in cosmology should have the following characteristics :

- Homogeneity. So that it can be used for a precise calibration of the luminosity and thus, of distance measurements.
- High luminosity. So that it can be observed in the distant universe.
- Ubiquity. So that it can be detected both in the local and distant universe.

In **3.1.1** we ended up with the relation :

$$d'_L = \frac{d_L}{d_H} = \frac{1+z}{\sqrt{|\Omega_k|}} S_k\left(\sqrt{|\Omega_k|}\int_0^z \frac{dx}{E(x)}\right), \tag{4.1}$$

where S_k is given by Eq.(2.9). The factor $\sqrt{|\Omega_k|}$ is removed for flat spacial section and

$$E(z)^2 = \left(\frac{H(z)}{H_0}\right)^2 = \Omega_r(1+z)^4 + \Omega_m(1+z)^3 + \Omega_k(1+z)^2 + \Omega_{DE}\exp\left(\int_0^z 3\left[\frac{1+\omega_{DE}(x)}{1+x}\right]dx\right). \tag{4.2}$$

Ω_i is used to denote the density of the i-th component (r-radiation, m-matter, DE-Dark Energy) in units of the critical density $\rho_c = \frac{3H^2}{8\pi G}$.

Determining cosmological parameters via the relation (4.1) requires the accurate measurement of the observed intrinsic luminosity of a standard candle. Strictly speaking there are no perfect standard candles. With thorough observations, some astronomical objects appear to be *standardizable*, i.e an empirical relation allows to estimate their intrinsic flux. Up to now, only two types of objects are standardizable: cepheids and Type Ia supernovae. An in-depth review on extragalactic distance indicators is given in (Jacoby *et al.*, 1992).

Cepheids are very luminous variable stars with a luminosity ranging from $5 \cdot 10^2$ to $5 \cdot 10^4 L_\odot$. These are young and massive stars (from 2 to 10 $M_\odot$) starting to burn the helium content in their core. Their intrinsic luminosity has been observed to obey an empirical law known as the PLC (period-luminosity-color) and given by :

$$< L >= \alpha \log_{10}(P) + \beta(< B > - < V >) + \gamma, \tag{4.3}$$

where $< L >$ is the star's intrinsic luminosity in a given band and $< B > - < V >$ is the average K-color (reddening correction explained below).

Unfortunately, because they are not luminous enough at high-redshift, cepheids cannot be used to accurately constrain cosmological parameters. Meanwhile, they remain objects of interest for the calibration of local distance measurements. The error budget on distance estimates using cepheids is said to be around 15% (Jacoby *et al.*, 1992). During the last decades, supernovae (SNe) have been succesfully used as extragalactic distance indicators and original approaches for the measurement of distances with SNe of different types have been developed (Kirshner and Kwan, 1974).

4.1.3 Elements of stellar evolution

Supernovae are born from stars and stars have an evolution globally described by the Hertzprung-Russel (HR) diagram (figure 4.1). Everything is believed to start in regions of overdensities known as protostars. These overdensities are said to result from acoustic waves in, as well as from collisions between dense molecular clouds. These overdense regions gravitationally attract matter from the surroundings. As more of that matter ($\frac{3}{4}$ hydrogen ,$\frac{1}{4}$ Helium and heavy elements) accumulates , an increase in temperature and pressure ignites the thermonuclear fusion of protons. The protostar then starts to generate some energy and slowly migrates towards the main sequence of the HR diagram : *A star is born and is maturing* (Bohm-Vitense, 1989).

Stars burn hydrogen into helium in their core. Their luminosity L is related to their surface temperature T_S by Stefan's law : $L = 4\pi\sigma \cdot R^2 T_S^4$ where $\sigma = 5.67 \cdot 10^{-8} W \cdot m^{-2} \cdot K^{-4}$ is Stefan's constant. While its hydrogen content is being burnt into helium, a star, in hydrodynamic equilibrium, evolves along the main sequence of the HR diagram. Any evolution beyond the main sequence depends on its initial mass. According to numerical simulations, two scenarios are possible :

If the mass of the star is greater than $\sim$ 8 solar masses, i.e. a high mass star, the thermonuclear fusion will last for a few millions years. The star is then hot and very luminous (10^4 to $10^6 L_\odot$). Once the hydrogen content in its core is exhausted, the latter contracts, as there is no longer enough energy produced to counterbalance the inner gravitational pull. The outer layers of hydrogen also contract and start burning into helium.

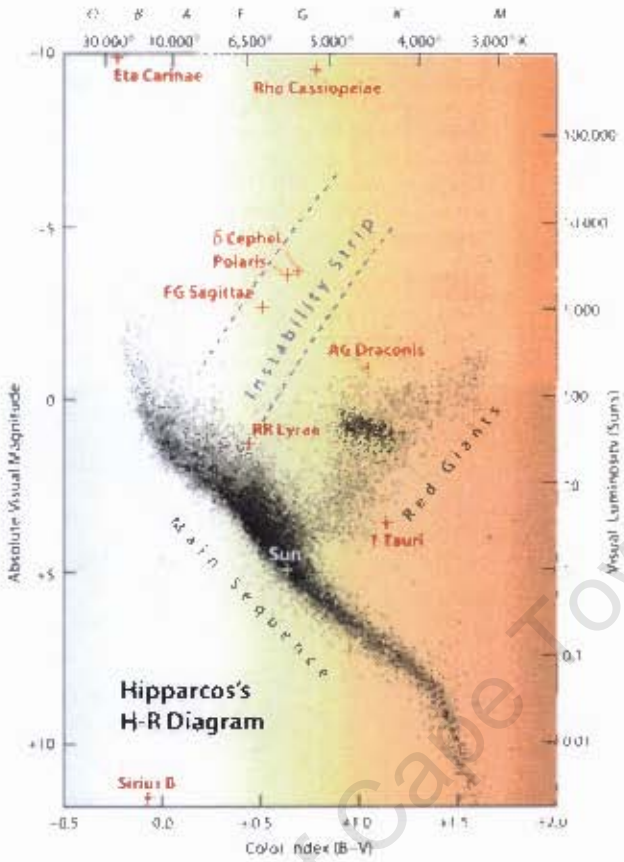

Figure 4.1: *Hertzprung-Russell diagram representing the absolute magnitude (or luminosity) as a function of surface temperature (or color) of a star. Temperature and color are equivalent because stars are seen as a perfect black body. Most of the stars are located along the main sequence of the HR diagram and spend their lifetime burning hydrogen into helium. Their subsequent evolution depends on their initial mass. For more details consult (Bohm-Vitense, 1989). Source : (http : //www.hip.obspm.fr/hipparcos/SandT/images/hipphrb.jpg)*

At this stage, the star has reached the temperature required to start fusing the helium content of its core into carbon, nitrogen, oxygen, neon, silicium and finally iron, the most stable element in nature. This process of energy production is known as the CNO cycle (Bethe, 1940). On the HR diagram, this stage corresponds to an evolution along the *horizontal branch* of the HR diagram (figure 4.2). Towards the end of its lifetime, that star is structured in layers formed by materials with increasing atomic mass as one moves towards the core (figure 4.3). Current estimates give a temperature of several billion degrees and a density of $\sim 10^{14} g/cm^3$ in the core. Details on this subject can be found in (Bohm-Vitense, 1989). It is generally admitted that the gravitational core collapse of a high mass star around the end of its lifetime is the physical process underlying the onset of a type II supernova, a type of SNe that is not of significant importance for the present work.

In the opposite case, **if the initial mass of the star is smaller than $\sim$ 8 solar masses**, the fusion processes in the core are slower because of smaller values for the central pressure and temperature than in the previous case. In particular, hydrogen fusion into helium can last for several billions of years. When the hydrogen content of the central layers is exhausted, the outer layers of hydrogen also contract and start burning into helium. The helium produced adds-up to

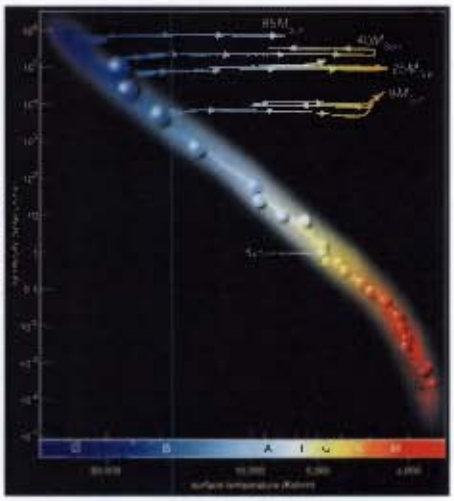

Figure 4.2: Theoretical evolutionary track on an HR diagram for a high mass star ($M > 8$ solar masses). It is generally admitted that the gravitational core collapse of a high mass star around the end of its lifetime is the physical process underlying the onset of a type II supernova. Source : (*http : //ganymede.nmsu.edu/tharriso/ast110/1322_1617.jpg*)

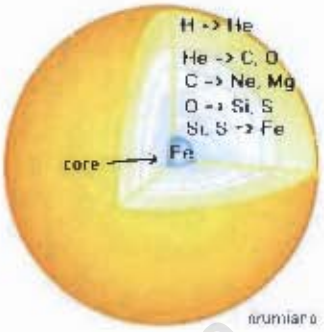

Figure 4.3: A model of the onion-like internal structure of a high-mass star towards the end of its lifetime. It is then formed by materials with increasing atomic mass as we move towards the core. Source : (*http : //nrumiano.free.fr/Images/oignon_E.gif*)

the mass of the core, which at that stage is degenerate i.e. the core hosts strengthened mutual repulsion of electrons forcing each other into higher energy states. Because of that degeneracy, the pressure is almost independent of temperature i.e. the usual processes regulating the equilibrium of the star no longer hold and due to their strong dependency on temperature, runaway thermonuclear fusions can occur.

As more and more layers of hydrogen are burning, the most outer ones are blown off by subsequent core expansion, producing a decrease of the surface temperature of the star, which then experiences a reddening. In a HR diagram, the star - around this stage - evolves along the *Red Giant Branch*. After $\sim$ one billion years, the temperature in the core is high enough to ignite the fusion of helium into carbon and oxygen. By inducing an expansion of the core, the subsequent onset of the Helium flash stage breaks the prevailing internal degeneracy and triggers an important expansion of the star leading it into the red giant stage.

At some point in time, the star evolves along the Horizontal Branch of the HR diagram over a period of a hundred million years. Somewhere there, the highly energetic photons emitted by the star (predominantly in the UV range) ionize the gas content of the ejecta (mostly hydrogen, nitrogen, oxygen), which then becomes visible as *planetary nebulae*.

Finally, when the Helium content has been exhausted, there is a collapse of the carbon-oxygen core due to its own gravity. The remaining thermonuclear fusion occurs in an almost static shell around that core. As the inner temperature is not high enough to ignite carbon fusion, the combustion in the external layers slowly dies out and when the mass of the remaining hydrogen reaches a threshold of $\sim 10^{-4} M_{\odot}$ (Bohm-Vitense, 1989), the star starts cooling down. It is then predominantly made of carbon and oxygen with a total mass smaller than the Chandrasekhar limit ($\sim 1.44 M_{\odot}$). It cools down further by radiating the remaining energy and ends up as a white dwarf: *a star is dead*. An illustration of that theoretical evolutionary track for low mass stars is given in figure 4.4. Details on this subject can be found in (Bohm-Vitense, 1989; Christensen-Dalsgaard,

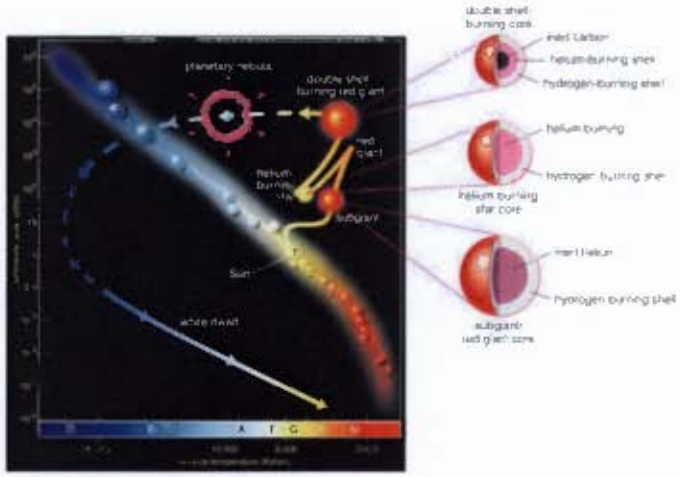

Figure 4.4: *Theoretical evolutionary track on an HR diagram for a low mass star ($M < 8$ solar masses). White dwarfs are typical end stages for that type of stars and they are seen as favourite progenitors for Type Ia supernovae Source : (http : //www.brumbrosom.com/astro/images/lowmass_lifetrack_hr.jpg).*

1995). As presented in the next sections, white dwarfs are seen as favourite progenitors for Type Ia supernovae, the sub-type of SNe relevant to the present work.

4.1.4 Observational classification of supernovae

Most of the time, supernovae classification is realised using information from their spectra mostly obtained a short time after the explosion. When a supernova occurs, the matter (ejecta) is ejected at high speed. As shown in figure 4.6, shortly after the explosion, spectral features evolve quite rapidly. The expanding shell of gas is optically thick meaning that we mainly observe absorption lines in the spectrum.

The first observational classification was introduced by (Minkowski, 1941). He defined two classes of types that were simply named I and II. The main difference between the two types came from their respective spectra : *Type II supernovae have hydrogen lines in their spectra (notably H_α and H_β) while type I do not.*

With time, differences started appearing among type I supernovae. They can be classified into two groups : *some of the type I SNe exhibit strong silicon (Si II) lines in their spectra with a light-curve easily recognizable by a larger B-band peak luminosity. They were given the name of Type Ia supernovae.* The others became type Ib or Ic depending on whether their spectrum suggest a large or small helium content respectively. As illustrated in figure 4.7, type II are much less luminous than Type Ia. Type II also have a sub-classification depending on the shape of their respective light-curve (see figure 4.7). The global classification scheme for supernovae is given in figure 4.5.

Considering the last decades of supernovae characterization, two main streams of criticism have emerged:

- It does not group supernovae according to their astrophysical origin; it is generally admitted that type II, Ib and Ic supernovae develop from (gravitational) core collapse (Filipenko, 1997) and Type Ia from thermonuclear explosions (as presented below);.
- It does not fully account for the wide variety of supernovae (figure 4.6).

The ongoing increase in surveys targeting supernovae will definitely improve their classification.

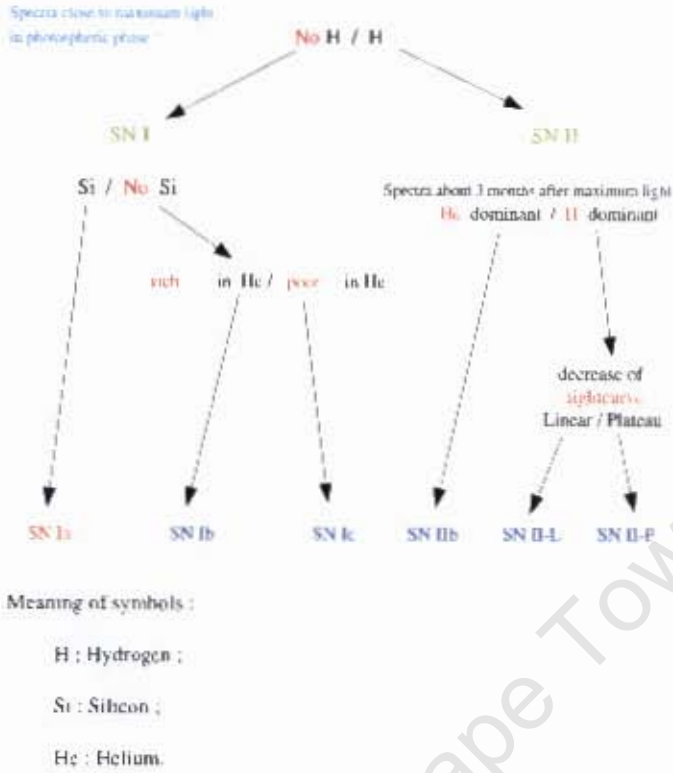

Figure 4.5: *Classification of supernovae based on the spectra around peak luminosity (photospheric phase) and the shape of the lightcurve. Type II supernovae have hydrogen lines in their spectra (notably H_α and H_β) while type I do not. Source : (Capellaro and Turatto, 1999).*

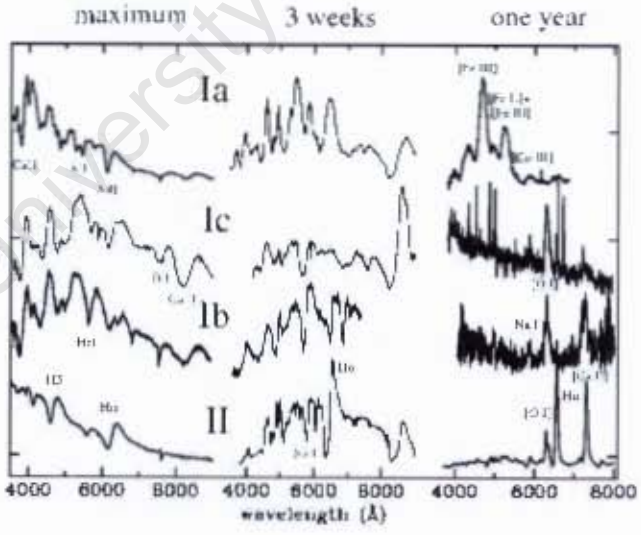

Figure 4.6: *Spectra of supernovae of the four main types. Left-hand side : For classification, spectra around maximum light are most commonly used. Middle: Some spectra obtained three weeks after maximum. Right hand side : Spectra, one year after maximum. The most prominent line-elements are identified. Source: (Turatto, 2003).*

4.2 Thermonuclear supernovae : Type Ia supernovae

4.2.1 What do we know about Type Ia supernovae ?

Known facts from their spectra

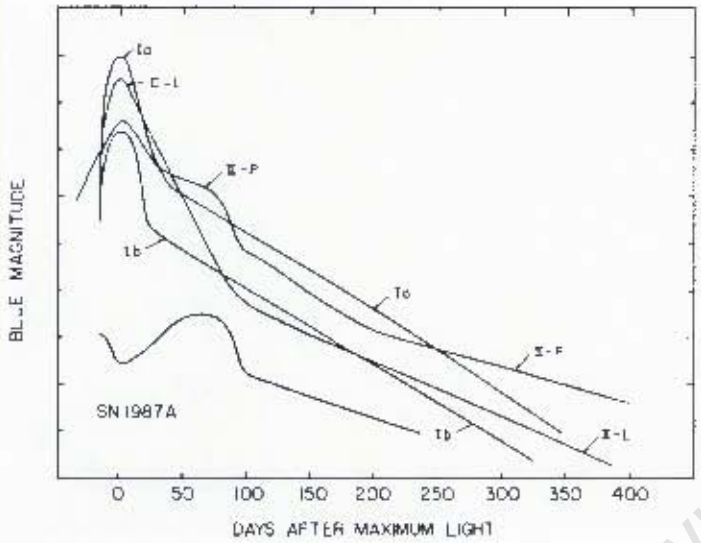

Figure 4.7: *Schematic lightcurves of the main types of supernovae through a B-band filter (centered around $\lambda_B^{center} = 4400$ angstroms). SNe Ia are clearly the most luminous objects. The curve for SNe Ib includes SNe Ic as well (they have similar spectroscopic and photometric properties), and represents an average. The typical "plateau" for SNe II-P is shown. The presence of SN 1987A is to highlight the fact that some supernovae cannot be classified in any of the known categories, these are called peculiar objects. Source : (Filipenko, 1997).*

- If the spectra are taken a short time (< 07 days) after the explosion, the surrounding shell of gas is still optically thick and mainly absorption lines are observed. As illustrated in figure 4.8, the SN Ia is in its *photospheric phase* and the "scan" in figure 4.10 schematically describes the evolution of the photosphere and the spectral features.
- On the opposite, if the spectra are taken several weeks after the peak in luminosity, mostly emission lines are observed, as the surrounding shell is more transparent to photons. The spectra are then said to be in the *nebular phase* (figure 4.9).

For classification purposes, the spectra used are mostly taken during the photospheric phase.

From these spectra, SNe Ia are recognized by the absence of hydrogen lines and the presence of broad lines due to high velocities of the ejecta. SNe Ia are characterised by a deep absorption trough around 6150 angstroms (rest frame) produced by blueshifted Si II $\lambda\lambda$6347, 6371 ; collectively called λ6355 and recognizable by a characteristic P-Cygni profile(figure 4.11). The spectrum also has some lines coming from intermediate-mass elements like calcium Ca II (3934 angstroms, 3868 angstroms and 8579 angstroms), magnesium Mg II (4481 angstroms), sulfur S II (5468 angstroms, 5612 angstroms and 5654 angstroms) as well as oxygen O I (7773 angstroms). Details on these lines can be found in (Filipenko, 1997; Leibundgut, 2000). Later on, these intermediate-mass elements are replaced by iron type elements that mostly appear in emission lines (Bowers *et al.*, 1997).

Known facts from their light-curve

Supernovae light-curves provide a lot of information. They are generally obtained from specially designed filters that select a fraction of the incoming light from the source. Figure 4.12 gives an example of SNe Ia lightcurves obtained through different filters. By convention, the origin of

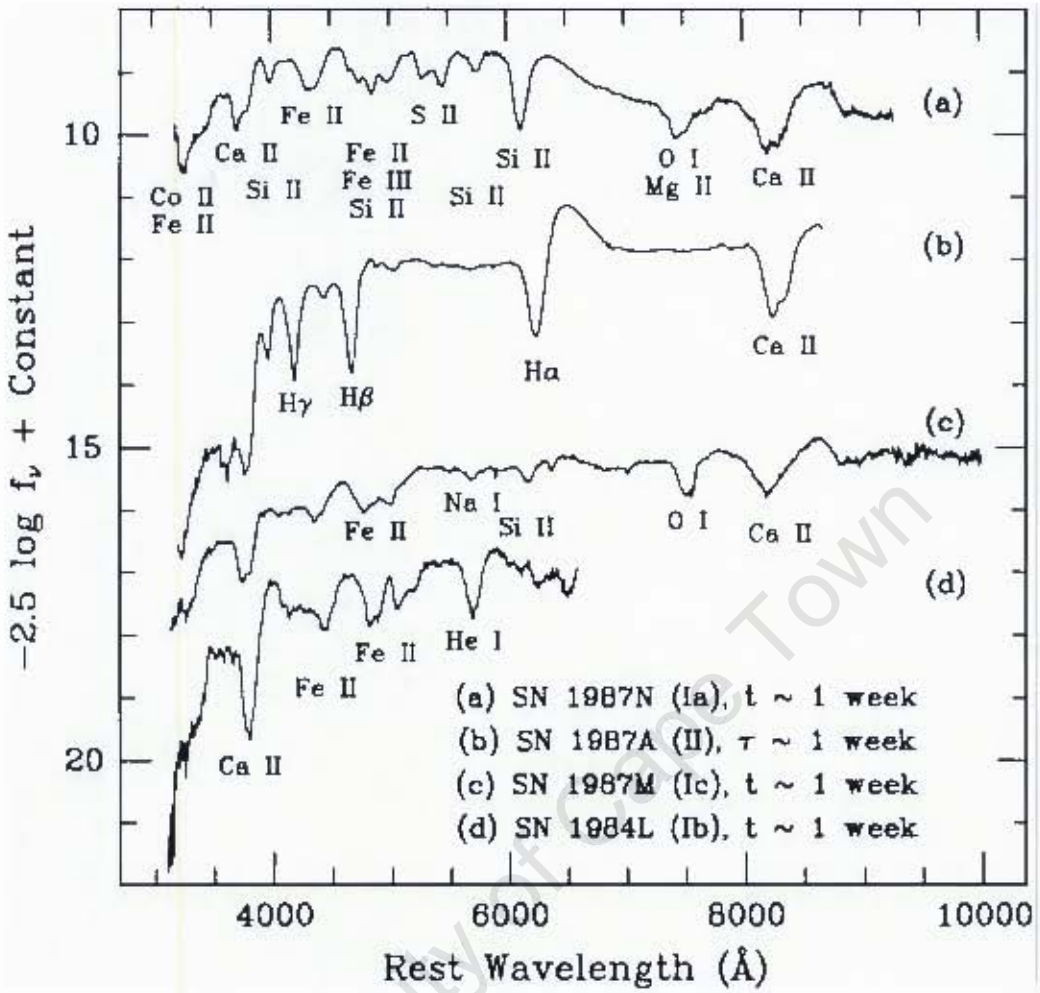

Figure 4.8: *Optical Spectra of some SNe in the photospheric phase (some days after peak luminosity). t and τ represent time after observed B-band maximum and time after core collapse, respectively. It is generally admitted that the gravitational collapse of the core of a high mass star around the end of its lifetime is the physical process underlying the onset of a type II supernova. The main lines of the spectra are identified. Source: (Filippenko, 1997).*

time is defined when the light-curve reaches its peak luminosity in the B-band[1] ($\lambda_B^{center} = 4400$ angstroms) relative to the Bessell system (Bessell, 1990). Three stages are noticeable on most of them :

- The increase : Observed in the B-band, SNe Ia reach the peak of their luminosity in approximately 18 days after the explosion. (Riess *et al.*, 1998) suggest an average value of 19.5 days.
- The maximum : It is reached earlier in the I-band than in the B-band with an average interval of 5 days. In terms of color, the SNe Ia shifts from blue to red from the maximum onwards. A gaussian or a polynomial can model that section (Contardeo *et al.*, 2000).

[1] *The choice of the B-Band as the commonly used filter in supernovae cosmology is based on the higher brightness of these objects in that wavelength region at maximum light, and on the availability of better constrained standardization from B-band lightcurves* (Folatelli, 2004).

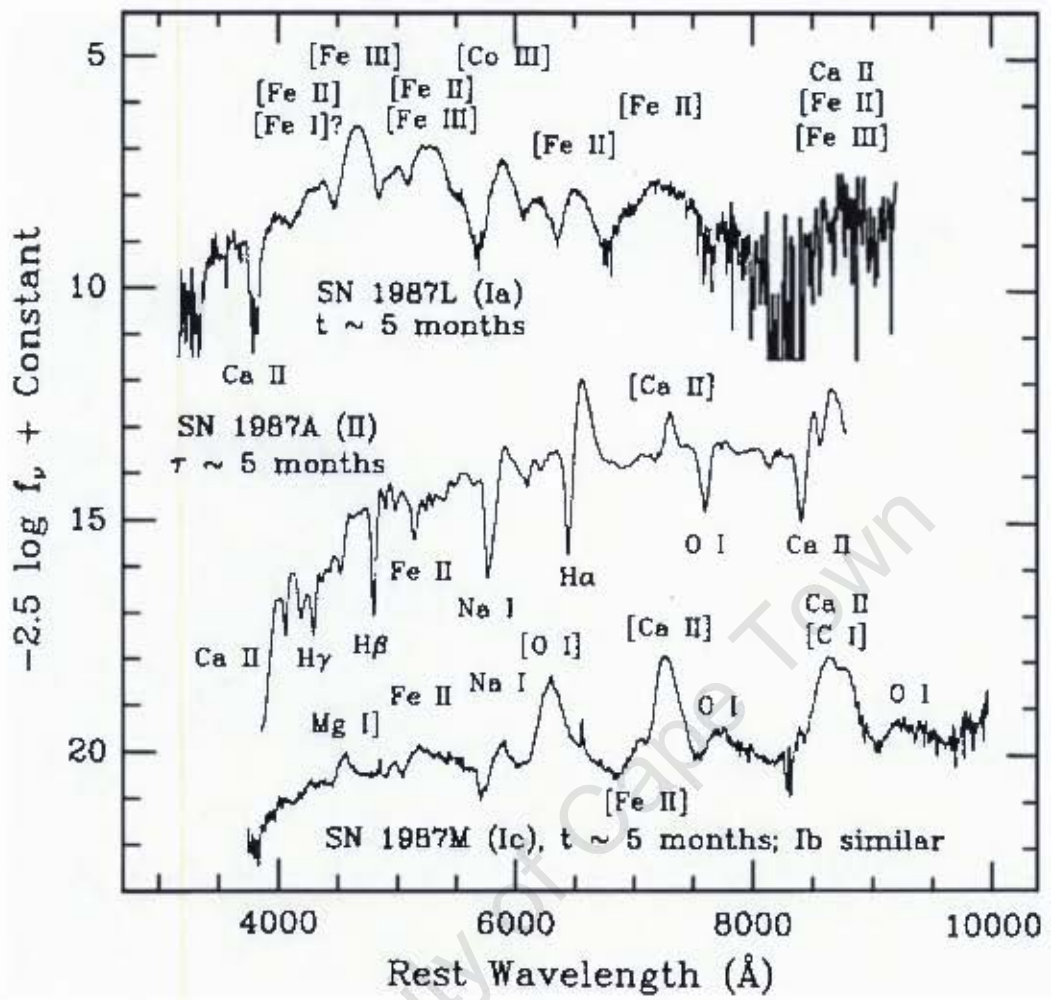

Figure 4.9: *Optical Spectra of some SNe in the nebular phase (some months after peak luminosity). t and τ represent time after observed B-band maximum and time after core collapse respectively. It is generally admitted that the gravitational collapse of the core of a high mass star around the end of its lifetime is the physical process underlying the onset of a type II supernova. The main lines of the spectra are identified. Source: (Filipenko, 1997).*

- The decrease : There is an exponential decrease in the UV and blue range (U and B-bands) while in the infrared range (from I-band onwards) the light-curve presents a second peak around 21 to 30 days after B-band maximum. Finallly, from 50 to 120 days onwards, SNe Ia lightcurves decrease uniformly in all the bands (Leibundgut, 2000).

In doing cosmology with SNe Ia, one learnt from section **3.1.2** about the importance of properly knowing the peak B-band magnitude as well as accurately estimating the Hubble constant (H_0). The most accurate values have been obtained from SNe Ia whose distances have been estimated from Cepheids. An average value of $M_B = -19.5 \pm 0.1$ and $M_V = -19.5 = 0.1$ has been measured from a set of eight SNe Ia (Saha *et al.*, 1999).

The Standardization of SNe Ia luminosities

As stated above, SNe Ia show a global homogeneity in their spectral and photometric properties. When omitting few peculiar ones, the majority of the residual population do exhibit that overall

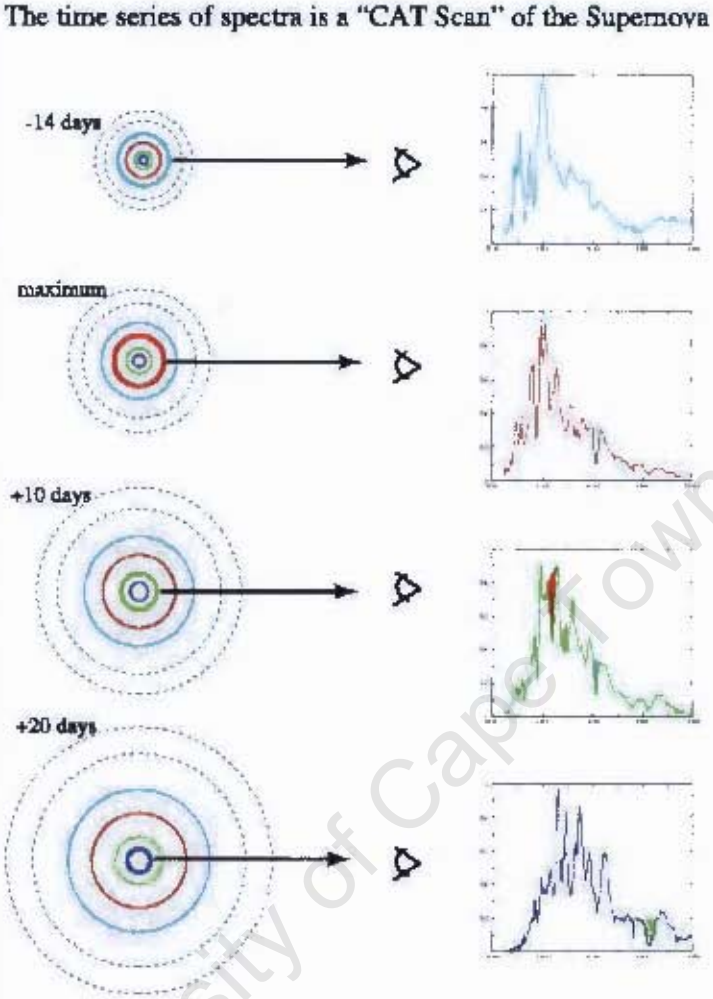

Figure 4.10: *A schematic view of the time evolution of a supernova spectrum. As the ejecta expands and cools down, the continuum and line properties change. The photosphere recedes in the ejecta and lines of different elements appear at different phases. Source: (Folatelli, 2004).*

homogeneity. The central fact in them being named *standardizable candles* rests upon the small dispersion ($\sigma < 0.4$ magnitudes) in their B-band absolute magnitude at maximum light as evidenced in the analysis of a large set of SNe Ia in the range $0.01 < z < 0.1$, the so called *Hubble flow*, (Hamuy *et al.* (1996) ; Riess *et al.* (1999)). In the Hubble flow, the Hubble diagram is well approximated by a linear law through the Hubble parameter ($d_L = \frac{z}{H_0}$), and the peculiar velocities of galaxies are negligible when compared to the recession velocities. Unfortunately, as illustrated in the top of figure 4.13, a $\sigma \simeq 0.4$ dispersion in magnitudes corresponds to relative fluctuations of $\sim 46\%$ in flux leading to disparities of $\sim 23\%$ in distances estimates.

The salvation comes from the fact that *brighter SNe Ia show broader lightcurves (i.e slower time-evolution) and vice versa*. That relation was first suggested by (Pskovskii, 1977). (Phillips, 1993) reinvestigated it using far better quality data on SNe Ia. It is the cornerstone of the standardization of SNe Ia luminosities. On top of that standardization, an adequate treatment of extinction is required: the study of SNe Ia in the *Hubble flow* strongly helped to address that aspect thanks to high quality data available in that range. In the first standardization method developed by (Phillips, 1993), one introduces the parameter Δm_{15}, as the amount in magnitude of the decrease

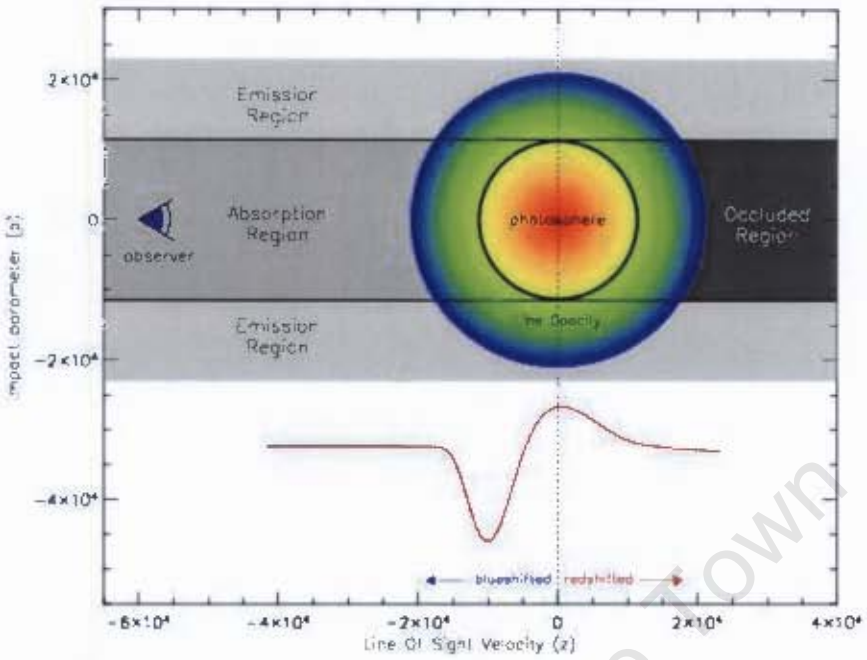

Figure 4.11: *The typical P-Cygni profile associated with the Si II absorption line in SNe Ia spectra. It is due to a rapidly expanding atmosphere. The atmosphere absorbs the outgoing photons and re-emits them isotropically. The region located between the core and the observer is approaching the latter. The subsequent absorption line appears blueshifted: for SNe Ia, it is commonly the blueshifted Si II λλ6347, 6371 (collectively called λ6355) resulting in the deep absorption trough around λ6150 (rest frame). Source : (http : //supernova.lbl.gov/ ∼ dnkasen/tutorial/p cygni/pcygni_form.jpg)*

of the B-band lightcurve between maximum light and 15 days after. After correction for extinction, a strong correlation was found between Δm_{15} and peak luminosity ($\sigma < 0.1$ mag) (Phillips *et al.*, 1999). A tentative explanation for that correlation is presented in section **4.2.5** below.

(Riess et *al.*, 1996) have developed a second approach by bringing the Δm_{15} method further into the multi-color lightcurve shape method (MLCS). The MLCS is an advanced method allowing to fit the relation between peak absolute magnitudes and lightcurve shapes for several colors simultaneously. One of its main advantages is to allow the inclusion of the extinction correction in the process of standardization (Folatelli, 2004). Extinction is known to be color dependent, i.e dimmed objects appear redder and the total absorption is proportional to the reddening. A third approach and simpler one is based on the capability of reproducing the range of observed lightcurve shapes by stretching or contracting the time axis of a template lightcurve by a *stretch factor s* (Perlmutter *et al.*, 1997). Figure 4.13 (bottom) illustrates a final result when using the stretch factor method. A dispersion of $\sigma \sim 0.18$ is typical for the current measurements of SNe Ia in the Hubble flow, when using these three methods. After correction for uncertainties and errors in redshift due to peculiar velocities (~ 300 km/s), an intrinsic precision ~ 0.12 (6% in the distance) is obtained for SNe Ia (Folatelli, 2004).

Some uncertainties ?

In the following we highlight three of the major difficulties that still plague what is known from SNe Ia's lighcurves:

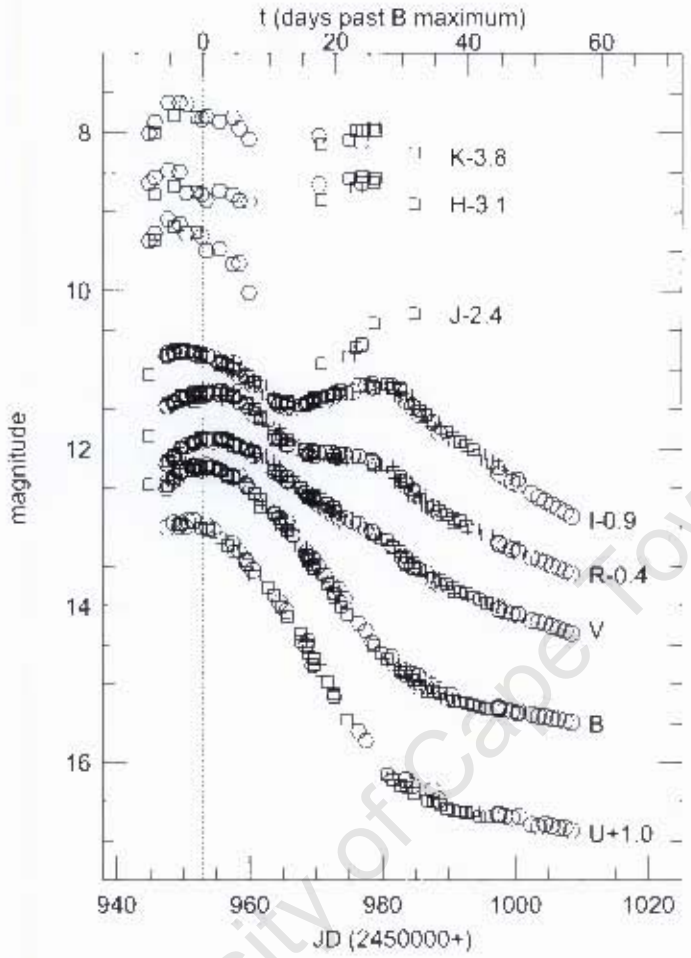

Figure 4.12: *Lightcurves for the Type Ia SN 1998bu taken through UBVRIJHK filters, covering ther wavelength range from the near-infrared to visible. Source : (Leibundgut, 2000).*

- **The difference in light curves** :
  Early in the use of SNe Ia as standardizable candles (Phillips, 1993; Hamuy and et al., 1993), it was shown that there is a strong correlation between the peak B-band brightness and the change in magnitude measured 15 days after (Δm_{15}). That correlation initially observed on a small set of data was later confirmed by (Riess *et al.*, 1994; Hamuy *et al.*, 1995). Sharp criticisms were raised by (Rowan-Robinson, 2002) when he brought some evidence that $M_B - \Delta m_{15}$ relation is weaker than stated if the analysis is restricted to supernovae observed before maximum. Notwithstanding that, a consensus is prevailing on SNe Ia, considering that after correction for that correlation, the dispersion is only about $\sigma \simeq 0.12$, corresponding to an uncertainty on the true distance of $\simeq 6\%$ (Folatelli, 2004).

- **Do SNe Ia evolve with redshift** ?
  A general rule of thumb is that an event at $z \simeq 1$ is seen when the universe is $\sim$ one third of its present age. The correlation between intrinsic luminosity and decay time is calibrated at low redshift. A natural question arising from that is whether SNe Ia observed at various

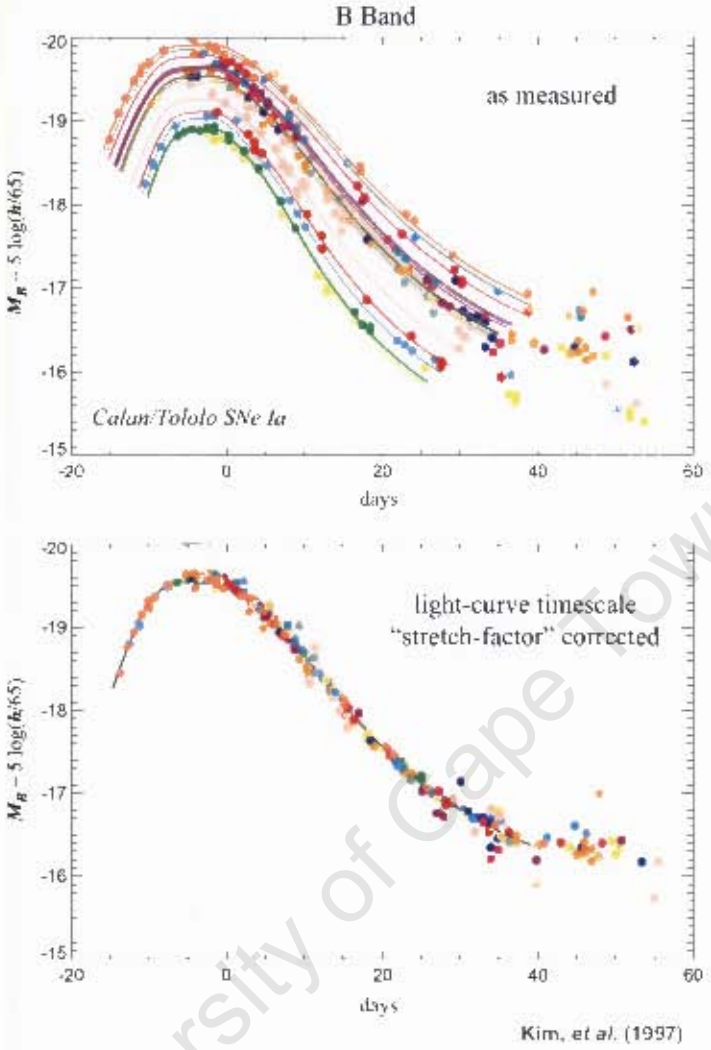

Figure 4.13: *Top: B-band spread of SNe Ia lightcurves. Clearly, SNe Ia with slowly evolving lightcurves are brighter than average and vice-versa. The dispersion in terms of flux is estimated to be ~ 40%. Bottom: The same lightcurves after the contraction of the time axis of the lightcurves by a stretch factor s has been applied. The dispersion in magnitudes appears significantly reduced than in the top. Source: (Perlmutter* et al., *1997).*

epochs of the universe exhibit consistent and strong enough similarities for them to be used in cosmology. In other words, to be used for robust work in cosmology, it is necessary that SNe Ia do not evolve or only mildly. Recent work on that problem seem to indicate that SNe Ia do not evolve significantly (Goobar and Perlmutter, 1995; Drell *et al.*, 2000; Branch *et al.*, 2001) as illustrated in figure 4.14. Presently, two approaches have been adopted by observational teams to see if evolution has its role in the dimming of high redshift supernovae : going to higher redshift to investigate how the Hubble diagram evolves, and increasing the statistical sample with multi-band photometry and spectroscopy.

- **Extinction** and **K-correction**

  When measuring magnitudes of SNe Ia, corrections for photometric band effects (K-corrections) and foreground effects (extinction) are applied. The accuracy of these corrections depend on the knowledge of SNe Ia intrinsic properties. As far as cosmology is concerned, the central

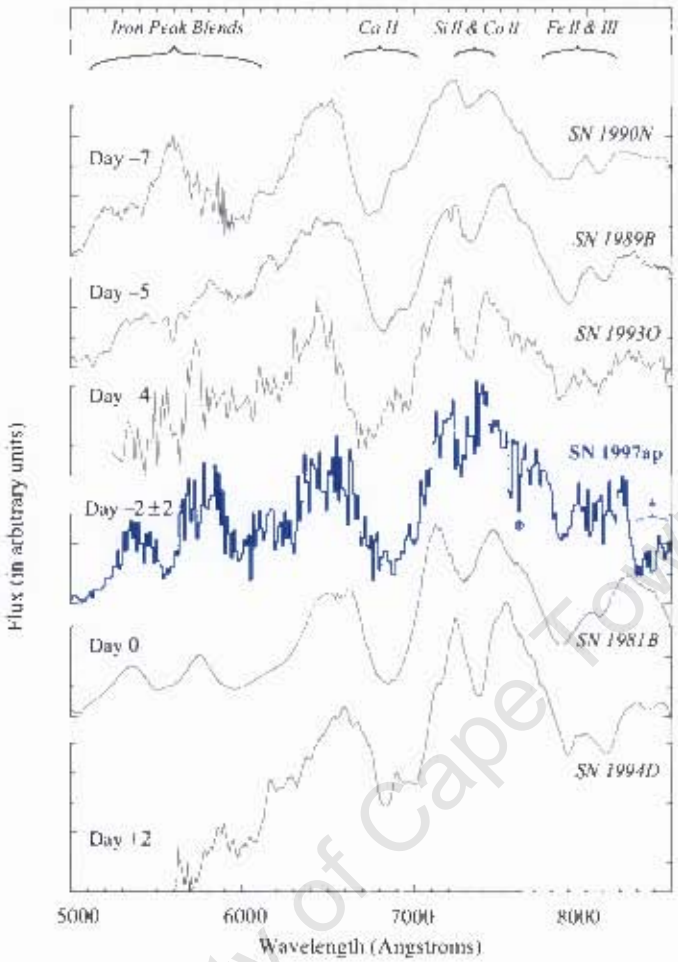

Figure 4.14: *Comparison between spectra from nearby SNe Ia and of SN 1987ap, a SNe Ia at z = 0.83. All the spectra are brought into the rest frame of SN 1987ap. The absence of any noticeable difference suggests an almost total absence of evolution with respect to redshift among SNe Ia. Source : (Perlmutter* et al., *1998).*

question here is to know what physical process(es) other than the accelerating universe can induce the dimming of light from SNe Ia.

Extinction

Extinction is a term used in astronomy to describe the absorption and scattering of light emitted by astronomical objects by matter (dust and gas) between the emitting object and the observer. In the optical domain, blue light is observed to be much more strongly attenuated than red light and this results in an object appearing redder than expected (i.e dimmed) to an observer and the total absorption is proportional to the interstellar extinction that is called reddening. It was realized early enough that reddening could induce a dimming of SNe Ia, similar to the one attributed to the accelerating universe. While some nearby SNe Ia take place in ellipticals where internal extinction (IE) in the host may be neglected, a large fraction of them takes place in spiral galaxies where IE cannot be neglected. For the reasons given previously, the presence of dust on the optical path can induce dimming of supernovae light. It is therefore capital to disentangle between the dust and the accelerated expansion contribution in the dimming of SNe Ia. (Riess *et al.*, 1998; Perlmutter *et al.*,

1999), assumed that IE at high redshift is small or even negligible, in addition to using 1 to 2 filters only (Rowan-Robinson, 2002). Given a supernova intrinsic color, it is possible to correct for reddening. Two approaches are currently extended to deal with this issue. The first one consists in taking multi-band photometry to increase the color leverage and make dust contribution more detectable. The second one is to observe at higher redshift to discrimate between scenarios of dust or dark energy (DE) : because extinction correction terms for typical environments are known in some way (see section **4.2.2**), going to high z will accentuate DE contribution while extinction factors lead to characteristic reddening unless the dust has unusual properties (Aguirre, 1999). In doing so, a careful attention is also given to properly correcting for dust from the Milky Way.

K-correction

The dimming of SNe Ia could also be due to instrumental effects. An important difficulty appears when one tries to evaluate the magnitude through a specific filter. For SNe Ia, the peak magnitude is usually obtained in the rest frame B-band filter, while the observations are done using filters which, redshifted, do not exactly correspond to the previous one. K-correction is the term introduced for the purpose of correcting that error. More precisely, the magnitude of an object at redshift z, observed through a filter i is corrected by (Folatelli, 2004) :

$$m_i = m_i(z = 0) + K_i(z), \tag{4.4}$$

where $K_i(z)$ is the redshift-dependent K-correction that applies to the observation at that redshift.

The K-correction usually depends on the flux observed through a filter i and the transmission of that same filter. On top of that, it has to be taken into account the fact that SNe Ia spectra evolve with time, particularly around maximum light. Therefore, it is not possible to use a single SNe Ia spectrum to compute the K-corrections at all times: making spectral time series is required. Because of the observed homogeneity of SNe Ia spectra, the basic strategy consists of using time series of template spectra to compute K-corrections for any supernovae. The numerous inaccuracies appearing when implementing this strategy are said to be resolvable with a large sample of spectro-photometrically well observed SNe Ia such as planned by the Nearby Supernova Factory and more recently the Supernovae Legacy Survey (SNLS) and the the Sloan Digital Sky Survey (SDSS). An additional difficulty comes from the fact that at $z \sim 0.5$, for a B-band filter K-correction, some information from the U part of the spectrum is needed. For handling the last problem, the approach developed first by (Kim *et al.*, 1996) consists of introducing a cross-filter K-correction, $K_{ij}(z)$. Through a filter j, the observed magnitudes of an object at redshift z are corrected by (Folatelli, 2004) :

$$m_j(z) = m_i(z = 0) + K_{ij}. \tag{4.5}$$

Most of the additional work will then consist of reducing the uncertainties in the (cross-filter) K-correction.

4.2.2 Defining a distance indicator from Type Ia supernovae

Doing cosmology using SNe Ia as standardizable candles requires an accurate knowledge of both their magnitude and redshift. From an observational point of view there appears a need to introduce

an *effective magnitude*. It depends on the choice of filter i in which the observations at low-redshift are done. At high-redshift, the effective magnitude is given by (Folatelli, 2004) :

$$m_i^{eff} = m_j - K_{ij} + \Delta_{corr} - A_i - A_j, \tag{4.6}$$

where K_{ij} is the cross-filter K-correction, m_j as defined in Eq.(4.5), Δ_{corr} is a correcting term obtained from the Δm_{15} relation seen in section **4.2.1**, A_i is a correction for extinction in the host galaxy (assuming that the extragalactic extinction is produced in the host galaxy), and A_j is the corresponding Galactic extinction in the observed filter. The more the ways to treat the right side of Eq.(4.6), the more the available strategies. As illustrated in figure 4.15, the B-band filter is commonly used for the previously stated reasons.

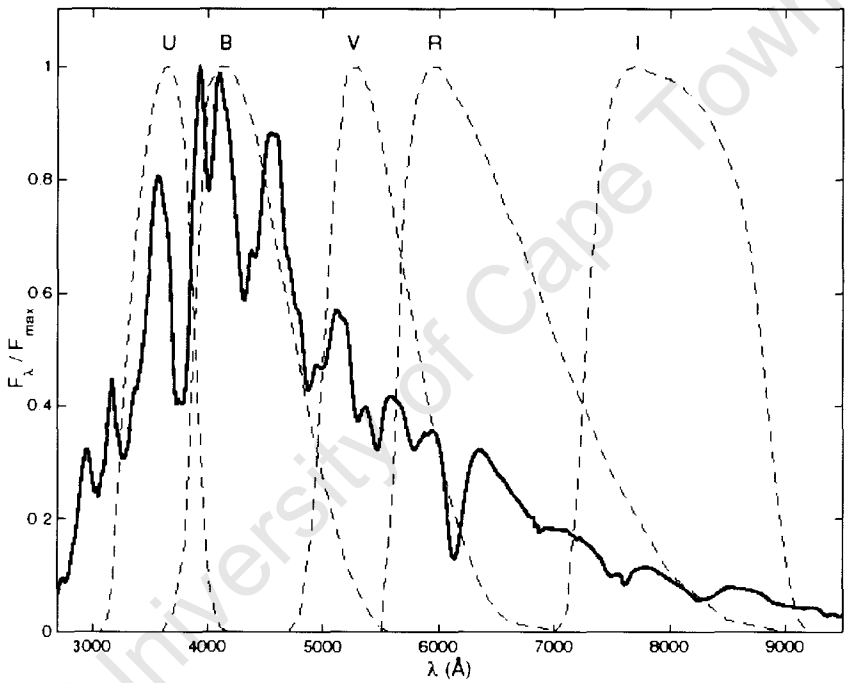

Figure 4.15: *Optical photometric passbands UBVRI superimposed on a SNe Ia spectrum at peak luminosity. The choice of the B-Band as the commonly used filter in supernovae cosmology is based on the higher brightness of these objects in that wavelength region at maximum light, and on the availability of better constrained standardization from B-band lightcurves Source : (Folatelli, 2004).*

From section **3.1.2**, Eqs.(3.11) and (3.13) led to :

$$m(z) = M + 5 \cdot \log_{10}\left(d_L^{'}\right) + 25 + constant, \tag{4.7}$$

where $d_L^{'} = \frac{H_0}{c} \cdot d_L = \frac{H_0}{c} \cdot d_L\,(z, \Omega_M, \Omega_\Lambda)$ is a dimensionless quantity with d_L, the luminosity distance given by Eq.(3.11). The *constant* term is a correcting term defined for each supernova. Once m_{B-band}^{eff} is known from the measurements, one is left with the task of fitting a model given by the right hand of Eq.(4.7) to the data and to extract the optimal cosmological parameters H_0, Ω_M and Ω_Λ via :

$$m_{B-band}^{eff} = m(z) = M_{B-band} + 5 \cdot \log_{10}\left(d_L^{'}\right) + 25 + constant. \tag{4.8}$$

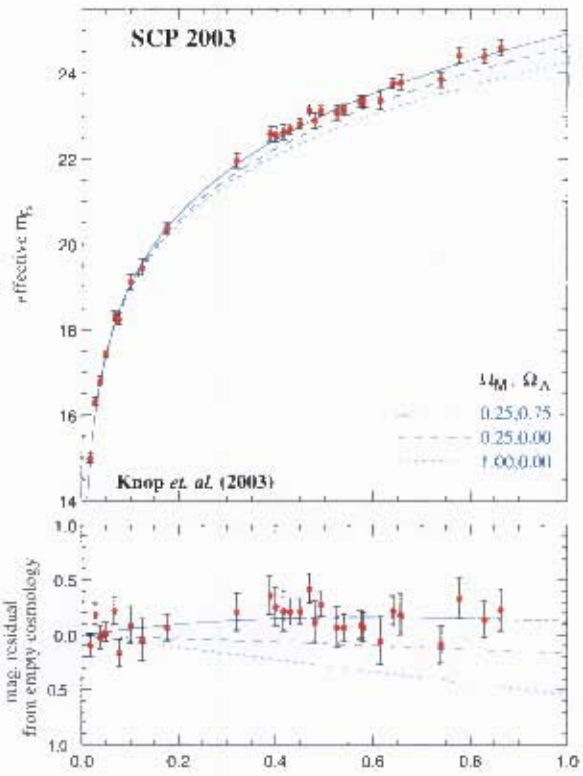

Figure 4.16: *Hubble Diagram representing the evolution of the apparent magnitude versus redshift for Type Ia supernovae seen as standardizable candles. For clarity, points within $\Delta z < 0.01$ from each other have been averaged. The best-fit cosmology $(\Omega_M, \Omega_\Lambda) = (0.25, 0.75)$ is represented by a solid curve. The degeneracy between models is clearly broken at high-redshift. lower panel : Residuals Hubble diagrams compared to the case of an empty Universe $(\Omega_M, \Omega_\Lambda) = (0, 0)$. Source : (Knop et. al., 2003)*

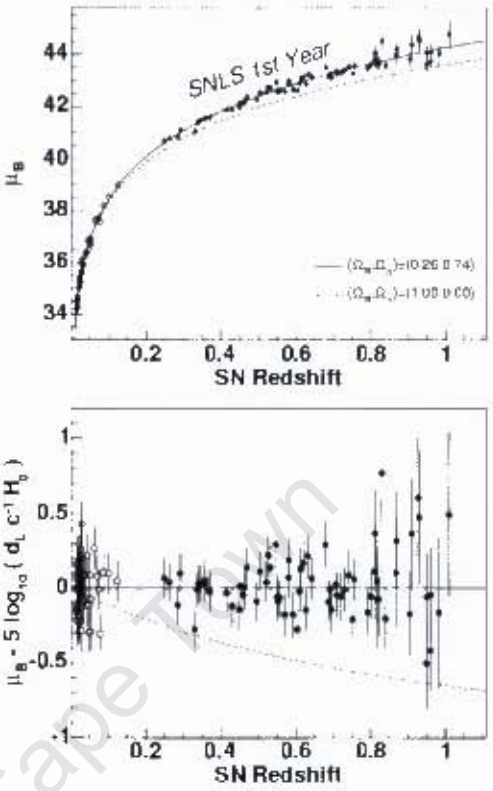

Figure 4.17: *Hubble diagram from SNLS first year data set. The evolution is given in terms of B-band distance modulus μ_B versus redshift. 71 high-redshift SNe Ia from SNLS and 44 from low-redshift ones were considered. The best-fit cosmology $(\Omega_M, \Omega_\Lambda) = (0.26, 0.74)$ is represented by a solid curve. Inner panel: Residuals from each model when compared to the one given by the solid curve. The data strongly suggest an accelerated expansion driven by a cosmological constant while ruling out a flat universe filled only by matter (i.e $\Omega_M = 1 = \Omega_{total}$) at high confidence. Source : (Astier et. al., 2006).*

μ, the distance modulus, is given by :

$$\mu - m(z) - (M_{B-band} + 25 + constant)\,. \tag{4.9}$$

Assuming that H_0 and M_{B-band} are known with great accuracy, an analysis of the redshift (z) dependence of m^{eff}_{B-band} (or equivalently μ) as illustrated in figures 4.16 and 4.17 allows to discrimate cosmological models.

4.2.3 Where do Type Ia supernovae come from ?

The large variability in the spectral features of supernovae clearly points towards the need for a better understanding of their respective progenitor. In the following lines, we focus on dominant approaches trying to relate SNe Ia's spectral and photometric characteristics, and the physics associated to their progenitors. More details can be found in (Filipenko, 1997; Nomoto *et al.*,

1997; Hillebrandt and Niemeyer, 2000). The prevailing concensus is that the source of a "normal" Type Ia is a carbon-oxygen white dwarf accreting matter from its companion star in a binary system (figure 4.18).

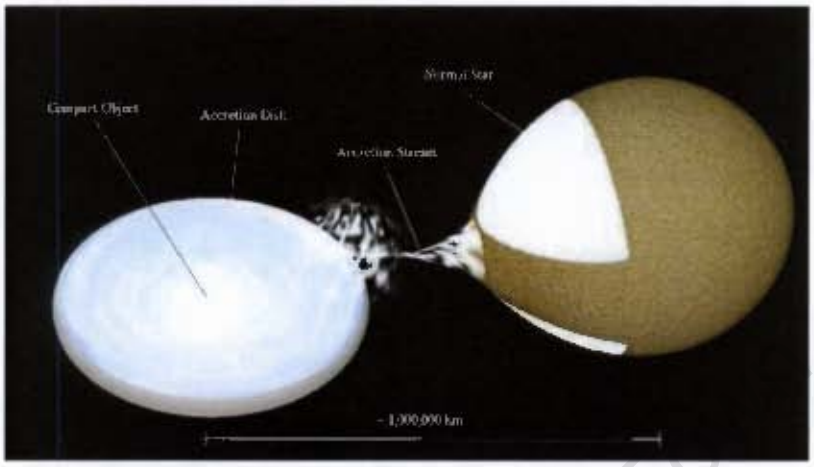

Figure 4.18: *Artist view of a binary system where a white dwarf is accreting matter from a companion star. The white dwarf is located in the central region of the accretion disk. Source : (http : //hea.iki.rssi.ru/ ~ tsp/M31/images/binary_scheme_1_captions_600×400.jpg)*

A white dwarf is the end stage of a low-mass star (mass $< 8M_{\odot}$). Once a low-mass star has burnt almost all the helium in its core into carbon, the temperature there is no longer high enough to fuse carbon. At this stage the outer layers of the star have been ejected into the interstellar medium and a degenerate carbon-oxygen core is left (Bohm-Vitense, 1989). The further gravitational collapse in the gas is prevented by the mutual repulsion of electrons forcing each other into higher energy states, i.e. the core is degenerate. The low mas star is at the end of its lifetime and may now be called a white dwarf: it has a very dense core with a mass of about 0.7 - 1.2 solar masses and is approximately the size of the Earth. 1.4 solar masses, the Chandrasekhar limit (Chandrasekhar, 1931), is the predicted upper limit of the mass of a white dwarf. It defines an equilibrium point in the interplay between the radiation pressure and the gravitational pull inside the star.

A white dwarf can increase its density and internal temperature via two processes :

- Collision with another white dwarf where they will lose angular momentum through gravitational wave radiation;
- Accretion of matter from a swelling binary companion star, often a red giant.

The admitted scenario in the last case (the most observed one) is that if the white dwarf accretes enough mass and exceeds the Chandrasekhar limit, then the temperature in the core becomes high enough to fuse the carbon content into ^{56}Ni. Because of the degenerate state of the core, the increased energy production does not lead to a change of the central pressure. The result is that the star does not expand. Instead, the higher energy output will increase the central temperature, which in turn will accelerate the fusion rate in the core and a thermonuclear runaway may set up. It leads to the explosion and complete annihilation of the white dwarf. That explosion is the phenomenon known as a Type Ia supernova. Such scenario leads to a probable understanding of the observed absence of hydrogen lines in their spectra that may be due to the almost total absence of hydrogen in a white dwarf. More details are given in (Bohm-Vitense, 1989)

The thermonuclear fusion of carbon and oxygen in the core goes up to the production of ^{56}Ni. The latter decays into ^{56}Co with a half-life of 6 days, then into ^{56}Fe with a half-life of 77 days. This double decay is supposed to account for the shape of the observed lightcurve (Niemeyer *et al.*, 2003). Early in the use of SNe Ia as standardizable candles (Phillips, 1993; Hamuy and et al., 1993), it was shown that there is a correlation between the peak brightness and the change in magnitude measured 15 days after (Δm_{15}). A tentative explanation of that last fact is contained in the idea that an increased mass in Nickel - as produced by the thermonuclear fusion of carbon - affects both peak luminosity and decline rate: as temperature rises in the core, the subsequent increase in opacity leads to a longer photon diffusion time that entails a longer decline (Filipenko, 1997).

As for any model , the previous scenario is not water tight. The main difficulties for most of them revolve around :

- The proper mastery of the equilibrium point defined by the Chandrasekhar limit. Some computer simulations give rise to explosions somewhere before the adopted value of 1.4 $M_{\odot}$.
- The binary system formed by a white dwarf and a companion star (mostly a Red Giant) is not the only one always considered. Some simulations do consider a binary system of two white dwarfs.
- The type of explosions occuring. It depends on whether the "flame" induced (ignited) at the breaking of the degeneracy in the core has a speed above or below the speed of sound. In each case, the induced thermonuclear fusion (of carbon and oxygen) gives rise to the same type of elements , but in varying proportions.

Thanks to the huge increase in computational power, very sophisticated numerical simulations are bringing a clearer picture of the large diversity prevailing among Type Ia supernovae. The task is still burdened by the lack of a satisfying mastery of their classification, the poor understanding of the physics of the progenitors as well as the prevailing uncertainties related to hydrodynamic models of SNe Ia. Meanwhile, the strong observational evidences previously highlighted point to the fact that SNe Ia are:

- homogeneous : they have similar spectral properties and light-curves;
- highly luminous : their peak luminosity can exceed the host galaxy's;
- ubiquitous. One of the most observationally challenging component of supernovae cosmology as SNe Ia seem to be rare events. Fortunately, recent advances in observational strategies (Perlmutter and Schmidt, 2003) have eased their detection from low and intermediate to high-redshift.

They seem to fullfill the requirements for being standardizable candles and used for cosmology. The forthcoming and ambitious surveys targeting at SNe Ia will certainly bring some additional light.

4.2.4 Where do we mostly find Type Ia supernovae ?

The rate of explosions of supernovae is the quantity used to quantify the distribution of SNe throughout the universe. It is the number of supernovae explosions per unit of volume per unit

of time (expressed in $h^3 \cdot Mpc^{-3} \cdot year^{-1}$ with $h = \frac{H_0}{100\ km/s/Mpc}$). As supernovae occur in galaxies, that number must depend on the luminosity of the host galaxy. Therefore , it is expressed in unit of B-band galactic luminosity per unit of time : 1 SNu (SuperNova unit) corresponding to 1 SN/$10^{10} \cdot L^B_\odot$/century ; $10^{10} \cdot L^B_\odot$ being the average B-band luminosity of a galaxy. Various estimates integrating cosmological models have yielded some estimates at low and high-redshift summarized in table 4.2. The rate of explosions of type II supernovae other than in the nearby universe is still unknown. *Table 4.1 suggests that SNe Ia are more common in spiral galaxies than in other morphological types.*

Type of Galaxy	Type of SN			
	Ia	Ib/c	II	All types
E-S0	$0.32 \pm 0.11\ h^2$	$< 0.02\ h^2$	$< 0.04\ h^2$	$0.32 \pm 0.11\ h^2$
S0a-Sb	$0.32 \pm 0.12\ h^2$	$0.20 \pm 0.11\ h^2$	$0.75 \pm 0.34\ h^2$	$1.28 \pm 0.37\ h^2$
Sbc-Sd	$0.37 \pm 0.14\ h^2$	$0.25 \pm 0.12\ h^2$	$1.53 \pm 0.62\ h^2$	$2.15 \pm 0.66\ h^2$
All types	$0.36 \pm 0.11\ h^2$	$0.14 \pm 0.07\ h^2$	$0.71 \pm 0.34\ h^2$	$1.21 \pm 0.36\ h^2$

Table 4.1: *Rate of nearby supernovae in units of* $SNu = \mathrm{SN} \cdot 10^{-10}\ \mathrm{L}^{\mathrm{B}}_{\odot} \cdot century^{-1}$ *where* $h = \frac{H_0}{100\ km/s/Mpc}$. *It suggests that SNe Ia are more common in spiral galaxies than in other morphological types. From (Capellaro and Turatto, 1999).*

$< z >$	$R_{\mathrm{SN\ Ia}}$ (h^2·SNu)	$(\Omega_{M_0}, \Omega_{\Lambda_0})$	Nb of SNe	Author
~ 0	0.36 ± 0.11		70	(Capellaro and Turatto, 1999)
0.14	$0.44^{+0.35\ +0.13}_{-0.21\ -0.07}$	(0.3, 0.0)	4	(Hardin *et al.*, 2000)
0.13	$0.23^{+0.09+0.08}_{-0.05-0.08}$	(0.3, 0.7)	14	(Blanc, 2002)
0.55	$0.58^{+0.10\ +0.10}_{-0.09\ -0.09}$	(0.3, 0.7)	38	(Pain *et al.*, 1999)
0.55	$0.94^{+0.16\ +0.14}_{-0.14\ -0.14}$	(1.0, 0.0)	38	(Pain *et al.*, 1999)

Table 4.2: *Estimates of rates of explosions for nearby SNe Ia. Estimates are given for various redshifts and values for comological parameters.*

4.2.5 Some peculiar Type Ia supernovae

In a previous section, an emphasis was put on the existence of peculiar supernovae among the globally homogeneous Type Ia class. Two of the most extreme examples are SN 1991T and SN 1991bg. Both have become the most refered prototypes for identifying two subtypes of peculiar SNe Ia. The spectra of 1991T-like SNe show particularly weak Si II (λ6355) before maximum light. The spectra of 1991bg-like SNe show particularly strong Ti II lines that persist long after maximum light. 1991bg-like SNe are also found to be $\sim$ 2 to 3 magnitudes fainter and significantly redder than "average" SNe Ia (Folatelli, 2004). Spectra of SN 1991T, SN 1991bg and a normal one, SN 1989B are shown in figure 4.19. These "unconventional" supernovae are still poorly understood, worst than for "normal" Type Ia.

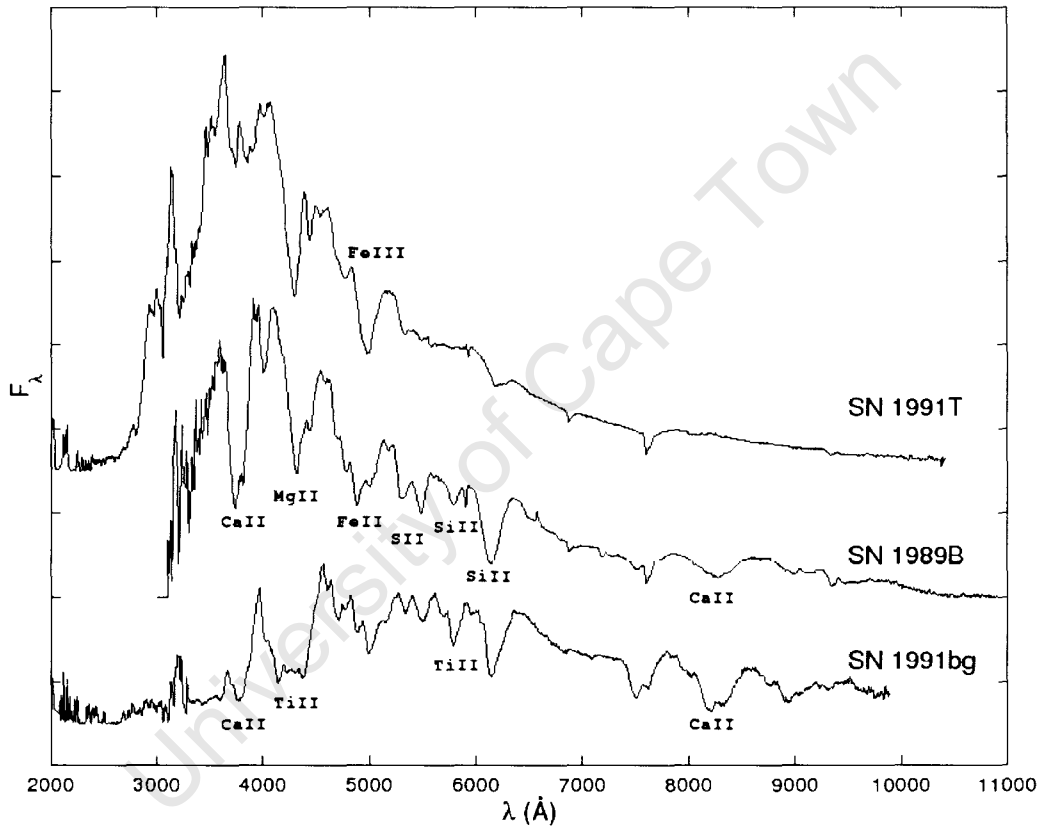

Figure 4.19: *Top : Spectra of SN 1991bg (bottom) and SN 1991T (top), two prototype peculiar . For comparison, a "normal" Type Ia (SN 1989B) spectrum is also shown. The most prominent lines are identified. Source: (Folatelli, 2004).*

Chapter 5

SNe Ia template fitting

5.1 Introduction

It was shown in chapter **4** that SNe Ia are good standardizable candles. For that reason, when observing some candidates SNe Ia for cosmology, the first challenge is to confirm its type (Ia, Ib, II, etc), redshift (z) and phase (Φ) with satisfactory accuracy; as inaccurate parameters lead to contamination of the sample (by non SNe Ia and/or atypical SNe Ia), which cause critical biases in the Hubble diagram and increase the errors on the luminosity distance (d_L). These three parameters can be extracted with satisfactory precision from the spectrum of the candidate. In this chapter; using Nugent's template spectra (Nugent *et al.*, 2002), we apply the χ^2 statistic to estimate :

- the redshift z,
- the phase Φ.

of given Type Ia supernovae from SUSPECT, an online database of supernovae spectra. By phase here, it is meant the rank occupied by the template in the list of 91 templates from Nugent. For example, phase 10 means the eleventh template from Nugent's templates which consist of a matrix of $91, 2401 - by - 3$ submatrices (each for one phase) arranged in increasing order from (phase) 0 to (phase) 90. A simple code identifies the twentieth template in Nugent's database as the template for a spectrum at peak B-band brightness. Hence a template at phase $\Phi = 25$ would - ideally - correspond to a template $|25 - 20|$ days after maximum and a template at phase $\Phi = 10$ would correspond to one at $|10 - 20|$ days before maximum. The code(s) hereafter developed could also be applied to SNe Ia spectra from the Southern African Large Telescope (SALT). In the process of fitting a "standard" template, it is also possible to confirm the type of the supernova in some cases. Two strategies have been implemented for that purpose : the first one is based on a grid strategy for the parameter space and the second is an implementation of the Metropolis-Hastings algorithm for the Markov Chain Monte Carlo method.

5.2 Pre-processing the data and the templates

As can be expected with any spectrum, the flux calibration process is not perfect. A consequence is that the overall amplitudes of the input spectrum does not coincide with the amplitudes and

shape of the templates : we then speak of a mismatch. For this reason, the input spectrum and templates are pre-processed and their residuals are used instead. These residuals are obtained by dividing each spectrum by its associated smooth function obtained by averaging the spectrum over a moving window of 500 datapoints. In two steps :

- Averaging of spectrum via a moving window of 500 datapoints. In the case of a template, it corresponds to a moving window covering a wavelength range of ~ 5000 angstroms.
- The wavelength range of the average spectrum is shorter than the one for the initial specrum. The spectrum is therefore "splined" over the average wavelength range and the output is divided by the previous average (point by point).

Typical outputs are presented in figures 5.1, 5.2, 5.3 and 5.4. In the best case, the end product is a curve oscillating around the value of 1 (figure 5.2), particularly advantageous from a computational point of view as working with the original spectra implies the processing of small values ($\sim 10^{-15}$). One additional advantage of that approach is to provide a dimensionless output, meaning a way to handle flux calibration problems. However, that strategy does throw away information and it makes it impossible to achieve good matches in some cases.

One additional source of mismatch comes from the fact that even if they have been recently updated[1], the Nugent templates used in this work are far from perfect, as clearly visible in the plots of all the residual templates in figures 5.5, 5.6 and 5.7. It appears that the majority of the initial sample used to generate the composite spectra relied on a few objects. According to (Foley *et al.*, 2007), Nugent originally constructed his templates from 84 spectra (31 for the maximum-light template) of which 63% (52% near maximum light) come from SNe 1989B, 1992A and 1994D. Two of these SNe Ia still appear as somewhat atypical in the literature, namely :

- SN 1989B shows strong dust absorption (Wells *et al.*, 1994);
- SN 1994D exhibits anomalous luminosity and colors (Richmond *et al.*, 1995; Patat *et al.*, 1996).

The size of the sample and the persistent influence of these atypical SNe Ia can result in severely skewing the composite away from the true average, making them non-ideal for template matching. Nevertheless these are typical template set in the literature. As illustrated in figures 5.23, and 5.24, the oscillating patterns in the input data contribute significantly to the amplitude mismatch. The quality of the fit in both extremities is particularly poor, with the blue part having a relatively strong contribution. The Nugent templates are clearly limited in scope and type. A way out of these limitations would be to widen the variety of SNe Ia used in creating the composite templates. That approach has been taken by authors like Blondin and Tonry (2006) in developing and testing the SNID tool introduced, that we discuss in chapter **6**.

Also of interest for computational reasons is the fact that the full set of templates is a single matrix of (2401×91) rows and 3 columns covering 91 days of evolution before, during and after peak B-band magnitude. The columns give the day, the wavelength and the amplitude respectively, with each day consisting of a sub-matrix of 2401 rows and 3 columns. Hence, the proper use of priors on redshift and phase coupled with reasonable CPU power have both a noticeable impact on the outcome and the duration of the parameter estimations whose algorithms are still subject to possible improvements. It is recalled that the grid based χ^2 has a computational cost that scales

[1] *http : //supernova.lbl.gov/ ∼ nugent_templates.html*

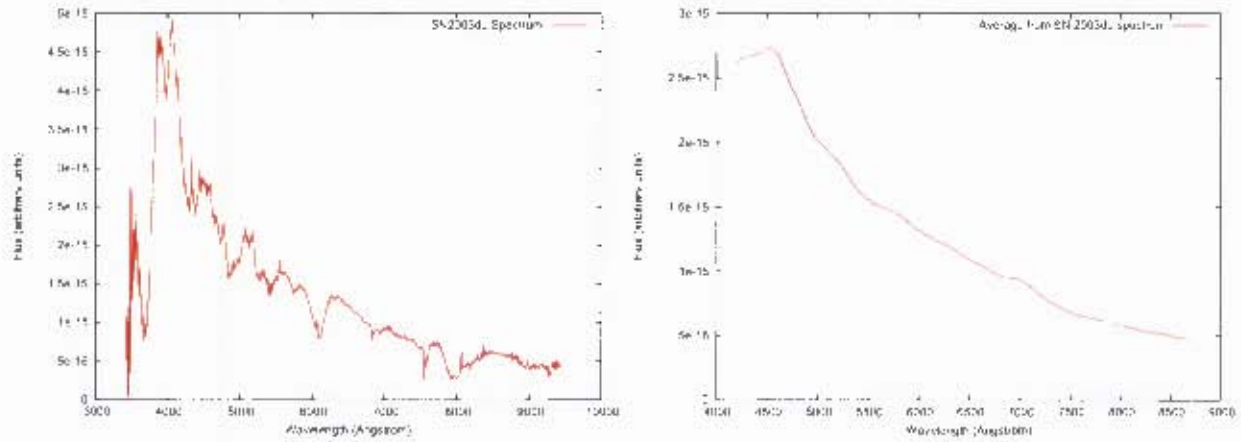

Figure 5.1: *Left : The spectrum of SN 2003du here plotted is from the SUSPECT database. It is a Type Ia supernova at redshift* ~ 0.0064. *Right : The average for SN 2003du spectrum is obtained via a moving window averaging strategy. The window size taken is made of 500 datapoints. The initial wavelength range of the average spectrum is shorter than the one for the initial data. The input spectrum is therefore "splined" over the average wavelength range and the output is divided by the previous average (point by point division).*

exponentially with the number of parameters (Doran and Muller, 2004) while the one for MCMC scales linearly with the number of parameters (Neal, 1993). In writing the octave code, special care was made to vectorise the code in order to avoid as much as possible the use of loops and control expressions (for,while,if, if-elseif-else). These are known to be extremely slow in octave. Unfortunately, not always is it possible to avoid loops when handling parts or the whole matrix mentioned above. The re-writing and execution of the initial octave codes in a matlab version also brings a significant improvement in the speed of the computational process by more than 60% (a decrease by a factor of ~ 70 in the case of the grid based estimation).

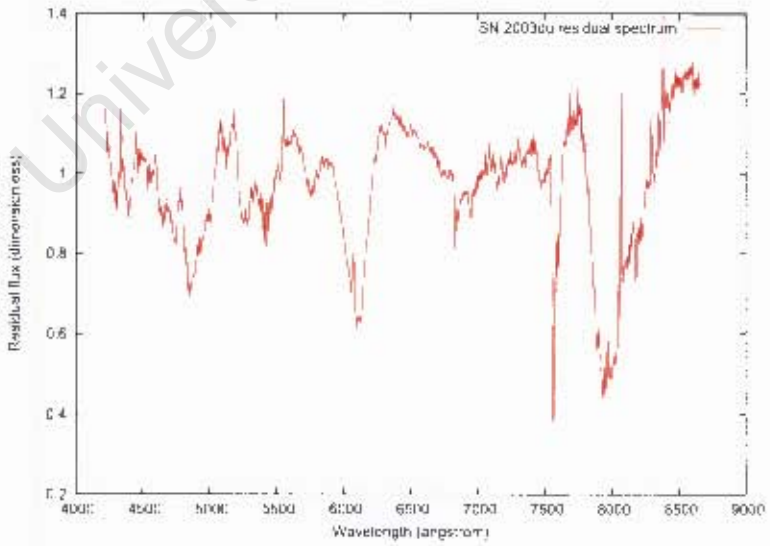

Figure 5.2: *Residual spectrum from SN 2003du, a Type Ia supernova. The window size used for the averaging is made of 500 datapoints. The resulting curve homogeneously oscillates around the value of 1, as expected.*

The strategy of averaging via a moving window was preferred to two other possibilities :

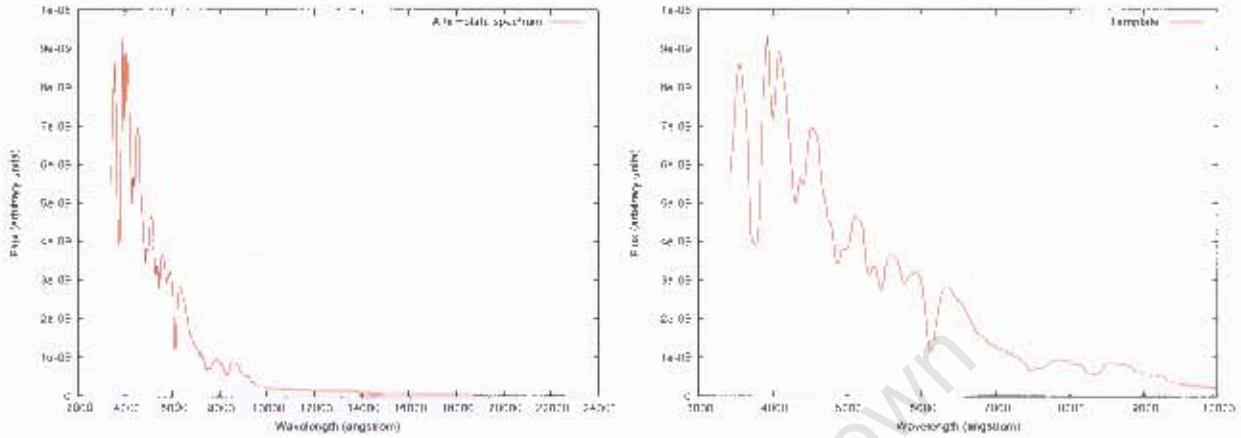

Figure 5.3: *Left : A template with phase = 20 from Nugent's set. Note the edge effects and the oscillating patterns on the spectrum. Right : The same template, this time truncated. The section between ~ 2000 and 10000 angstroms was extracted. Note that this template at phase = 20 is the template for a spectrum at peak brightness in Nugent's set of templates.*

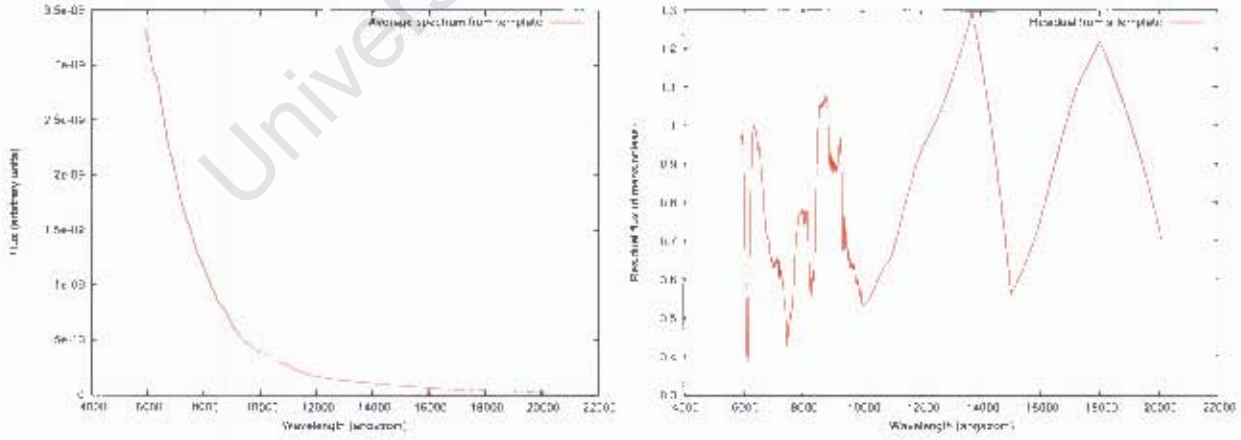

Figure 5.4: *Left : The average from the previous template is shown. It was obtained as explained in figure 5.1. Here, a window of 500 datapoints corresponds to a wavelength range of ~ 5000 angstroms. Right : Residual spectrum of the same template (phase = 20) from Nugent's templates. The features in the edges, particularly in the far right clearly highlight the "imperfection" in the averaging process used in generating the composite spectra. The wavelength range from 10000 angstroms onwards exhibit artificial patterns originating from the averaging procedure used by (Nugent* et al., *2002) in creating his templates.*

1. Splining the templates in such a way that both template and data are on the same grid; then performing the matching using these outputs directly. Compared to the moving window averaging, this is difficult because the data and the templates must be in the same units and an extra parameter, the relative amplitude, must be estimated, in addition to the redshift and the phase. Also, this method is sensitive to flux calibration errors.

2. Fitting a polynomial of fixed degree to both data and template; then dividing them by their respective polynomial fit. Here also dimensionless outputs are obtained. The unsatisfactory result of the polynomial fit of both data and templates made this approach unreliable compared to the moving window averaging. A known solution generally preferred in practice consists in using several polynomials of lower orders, i.e splines.

One other important step in handling both the data and the templates is the need to have then on the same wavelength grid prior to the computation of the χ^2. To do so, the spline of the residual templates over the wavelength range of the residual data is performed at relevant stages of each code.

5.3 The grid-based χ^2 statistical method

5.3.1 Principle of the χ^2 statistical method

In this method one uses a grid on the parameter space to estimate a set of N parameters $\Theta = (\Theta_1, \Theta_2, ..., \Theta_N)$ from observed spectra of a Type Ia supernova. The approach relies on the evaluation of the χ^2 statistics discussed below. In the present case, $N = 2$ where Θ_1 is the redshift z and Θ_2 is the phase of an observed Type Ia supernova. The basic problem is that one has a vector of data **D** from which one wishes to estimate a vector of parameters Θ. The aim is to try to fit a model with N adjustable parameters $\Theta = (\Theta_1, \Theta_2, ..., \Theta_N)$ to a set of M data points (x_i, y_i), $i = 1, ..., M$. The model predicts a relation between the measured independent and dependent variables given by :

$$y(x) = y(x; \Theta_1; ...; \Theta_N), \tag{5.1}$$

where the right hand-side in Eq.(5.1) gives the explicit dependence on the parameters and x in our case is the wavelength.

The question then is, what should one minimize to get the best values for the Θ_j's ? The very first idea is the usual least-square fit, i.e. minimize over $\Theta_1; ...; \Theta_N$, the quantity given by :

$$\sum_{i=1}^{i=M} [y_i - y(x_i; \Theta_1; ...; \Theta_N)]^2 . \tag{5.2}$$

However, the least-square does not weight the points (x_i, y_i) by their errors σ_i. Instead we want a statistic that is sensitive to the σ_i's. This leads us to introduce the *likelihood*, i.e. the probability of the data given the parameters. The best-fit parameters are then found by maximizing that likelihood. A common assumption is made that each data point (x_i, y_i) has a measurement error that is *distributed as a Gaussian* around the "true" model $y(x_i; \Theta_1; ...; \Theta_M)$ with variance σ_i^2. If in addition, it is assumed that each point has a measurement error σ_i that is independent (uncorrelated) of the others, then it can be shown that the *likelihood* L of the data set is the

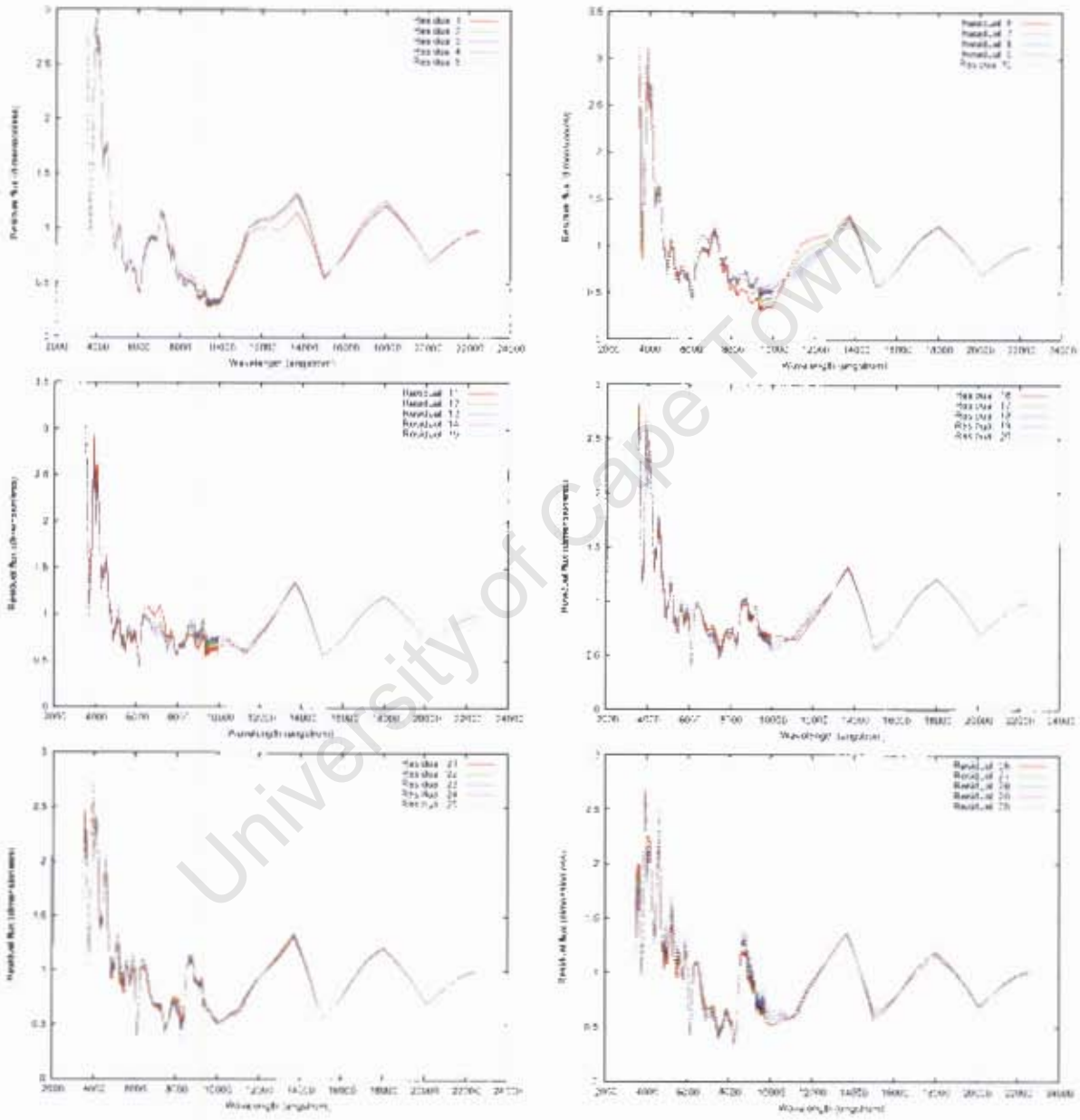

Figure 5.5: *Template residuals 1 to 30 from the Nugent's. Note the distorsions in the edges, particularly in the far right. The very first template in Nugent's database is a flat spectrum with a constant amplitude of* 10^{-20} *and its residual (of constant amplitude = 1) has not been represented.*

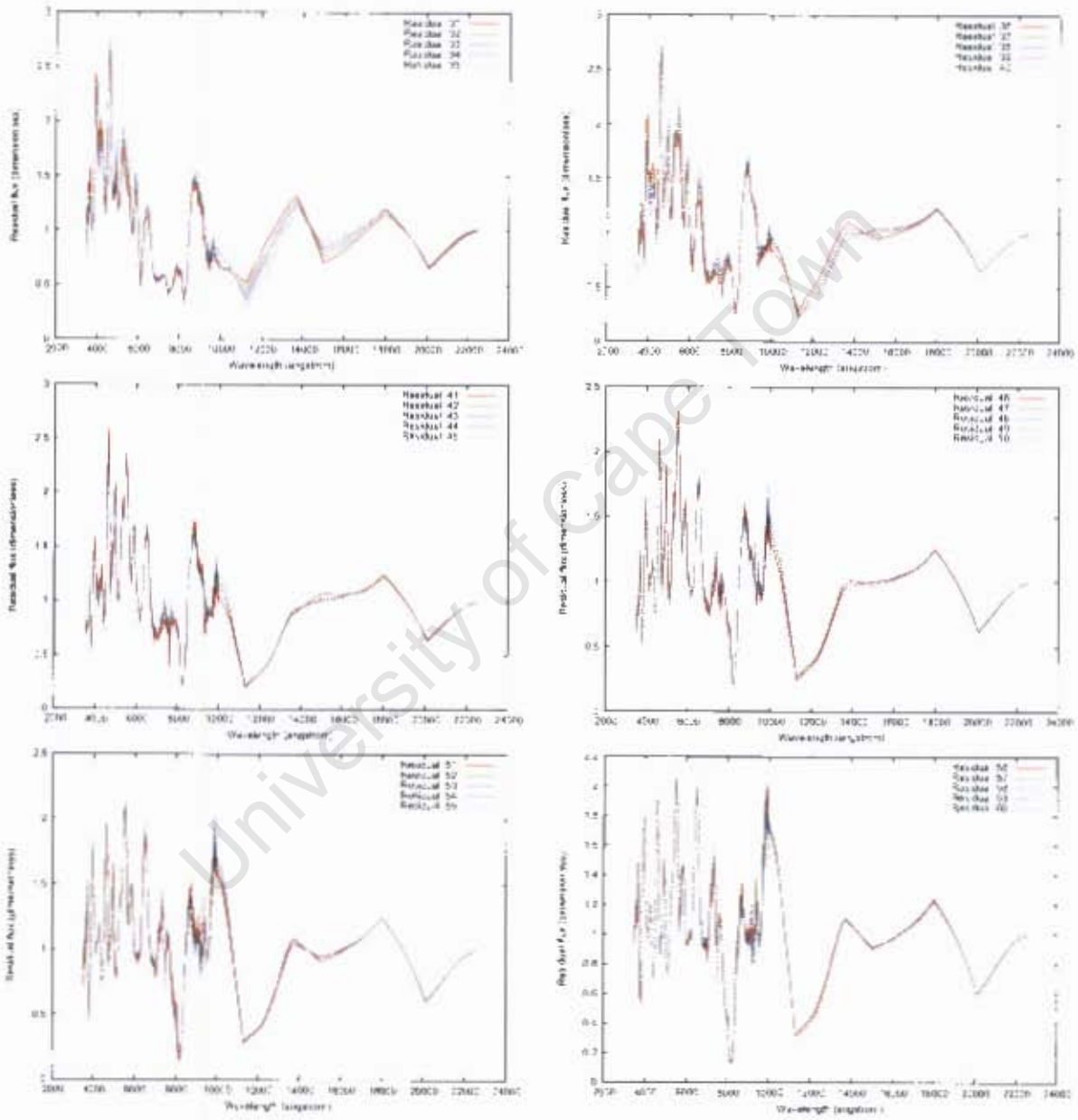

Figure 5.6: *Template residuals 31 to 60 from the Nugent's. Note the distortions in the edges, particularly in the far right.*

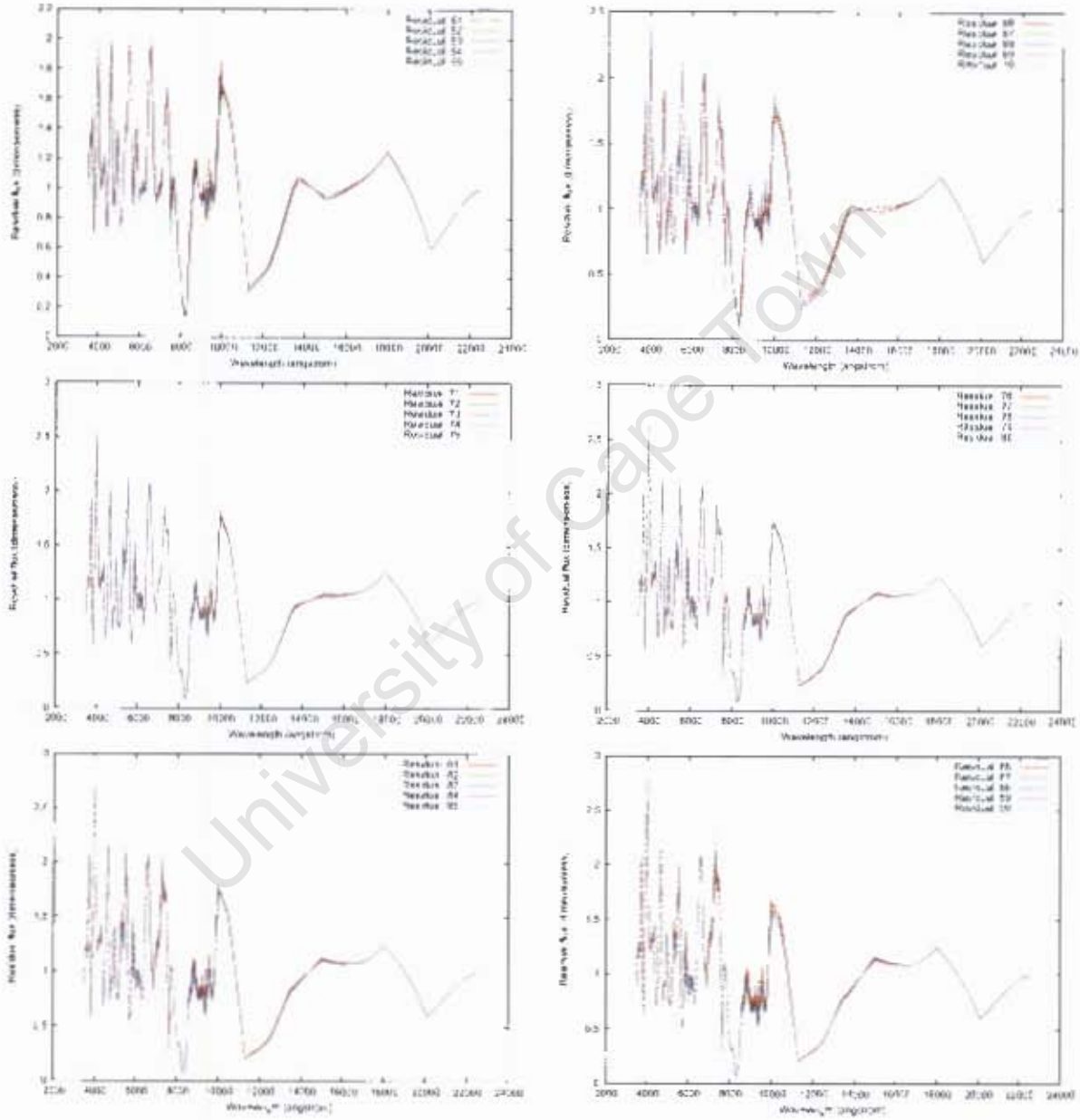

Figure 5.7: *Template residuals 61 to 60 from the Nugent's. Note the distortions in the edges, particularly in the far right.*

product of the probabilities of each data point :

$$L \propto \prod_{i=1}^{i=M} \left\{ e^{\left[-\frac{1}{2}\left(\frac{y_i - y(x)}{\sigma_i} \right)^2 \right]} \right\}. \tag{5.3}$$

Maximizing Eq.(5.3) is equivalent to maximizing its logarithm, or minimizing the negative of its logarithm. In other words, the maximum likelihood estimate of the parameters is obtained by minimizing the quantity :

$$\chi^2 = \sum_{i=1}^{i=M} \left(\frac{y_i - y(x_i; \Theta_1; ...; \Theta_N)}{\sigma_i} \right)^2. \tag{5.4}$$

The χ^2 statistical method is the simplest and most straightforward way of determining the best fit for the vector of parameters $\Theta = (\Theta_1, \Theta_2, ..., \Theta_N)$ that is also sensitive to the σ_i's. For the algorithm, a basic strategy consists of setting up a grid of points over the entire parameter space. The χ^2 value is then computed at each point and the best fit is obtained at the point with the lowest χ^2 value. The main weakness of this approach is its computational cost which scales exponentially with the number of parameters (Doran and Muller, 2004); meaning that this method is only viable for the estimation of relatively small set of parameters. More details on this method are given in (Press *et al.*, 1992). A point worth mentioning is that the probability distribution for different values of χ^2 at its minimum can be derived analytically, and is the χ^2 *distribution for M-N degrees of freedom* (M datapoints and N fitted parameters). It gives a quantitative measurement of the quality of the fit to the model.

5.3.2 Application of the grid-based χ^2 method to the spectral characterization of Type Ia supernovae

A χ^2-test is performed on some Type Ia supernovae from the SUSPECT database. The full code and the associated procedures and functions are given in the appendix. The flow chart is presented in figure 5.8.

Some results

The χ^2 minimization has been used to identify the best fit and $\Delta\chi^2 = \chi^2 - \chi_0^2 = \{1, 4, 9, 16\}$ to identify $\{68.3\%, 95.4\%, 99.7\%, 99.9\%\}$ confidence regions around the minima. χ_0^2 being the χ^2 for the best fit obtained by minimizing Eq.(5.4). In the present case, the denominator was set to a value $\sigma_i^2 = \sigma^2 = 1$. Once the best values for the parameters are known, it is also important to know how good the fit is from these estimates. There is, in the literature, a quantity named Goodness-of-Fit (GoF), which allows to monitor the quality of the fit to the data. It is defined as (Hannestad and Mortsell, 2004) :

$$GoF = \frac{\Gamma(\nu/2, \chi^2/2)}{\Gamma(\nu/2)}. \tag{5.5}$$

where $\Gamma(x)$ is the value of the gamma function at x , $\Gamma(x, y)$ is the incomplete gamma function[2]. ν is the degree of freedom which is defined as the number of measurements minus the number of fitted parameters. In the present case, the GoF does not fully account for the quality of the

[2]The upper incomplete gamma function is defined as $\Gamma(a, x) = \int_x^\infty t^{a-1}\, e^{-t}\, dt$ and the lower incomplete gamma function is defined as $\gamma(a, x) = \int_0^x t^{a-1}\, e^{-t}\, dt$ (Gradshteyn *et al.*, 2007)

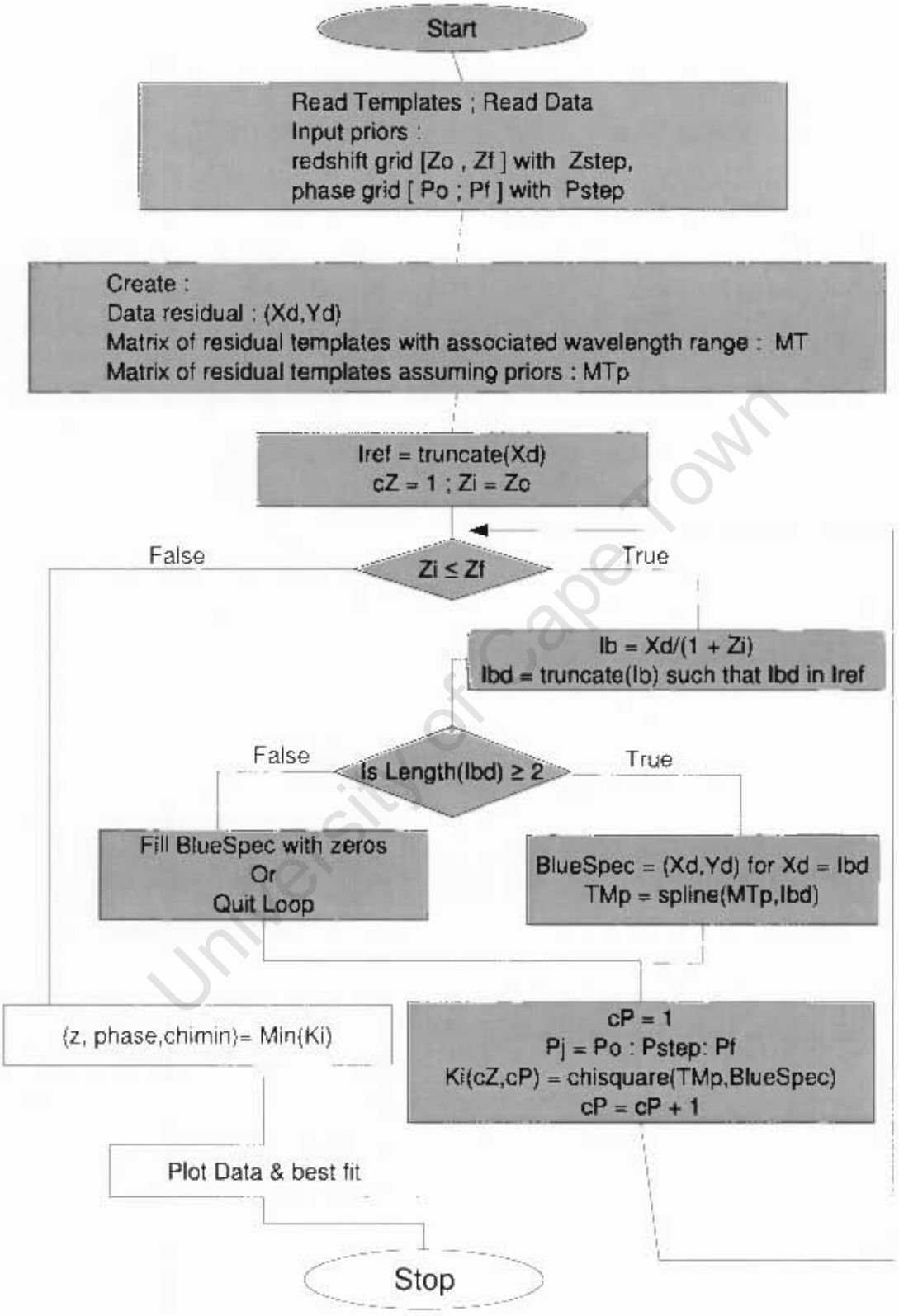

Figure 5.8: *flow chart for the implemented grid based code for* χ^2.

fit, considering that in the computation of the χ^2, the denominator σ_i^2 has been set to 1 for each datapoint. We therefore do not show the GoF in the outputs.

Let's explain here how we generate a redshifted spectrum from an initial one :

- Ispec = (Xspec, Yspec) is the initial spectrum to redshift by a a value z;
- XspecRedshifted = $(1+z)\cdot$Xspec is the wavelength range of the redshifted spectrum and for the blueshifted one we would have to take XspecBlueshifted $= \frac{Xspec}{1+z}$;
- (XspecRedshifted,Yspec) is our initial spectrum now redshifted by z and (XspecBlueshifted,Yspec) would be the blueshifted one.

It is worth mentioning that by input data it is meant the blueshifted initial data : the choice was made to blueshift the data (by each redshift candidate Zi) and then compare them to the templates instead of redshifting each template for each candidate redshift Zi and then comparing to the original data. Blueshifting or redshifting is done as explained above. A straightforward test of that basic strategy consists in firstly redshifting a given spectrum by a value z as presented above. Then blueshifting the output of the previous stage by the same value z. Finally, in figure 5.9, a plot is made of the square of the amplitudes difference between both output (i.e the χ^2) which should be minimized at the value of z (= 0.5) used.

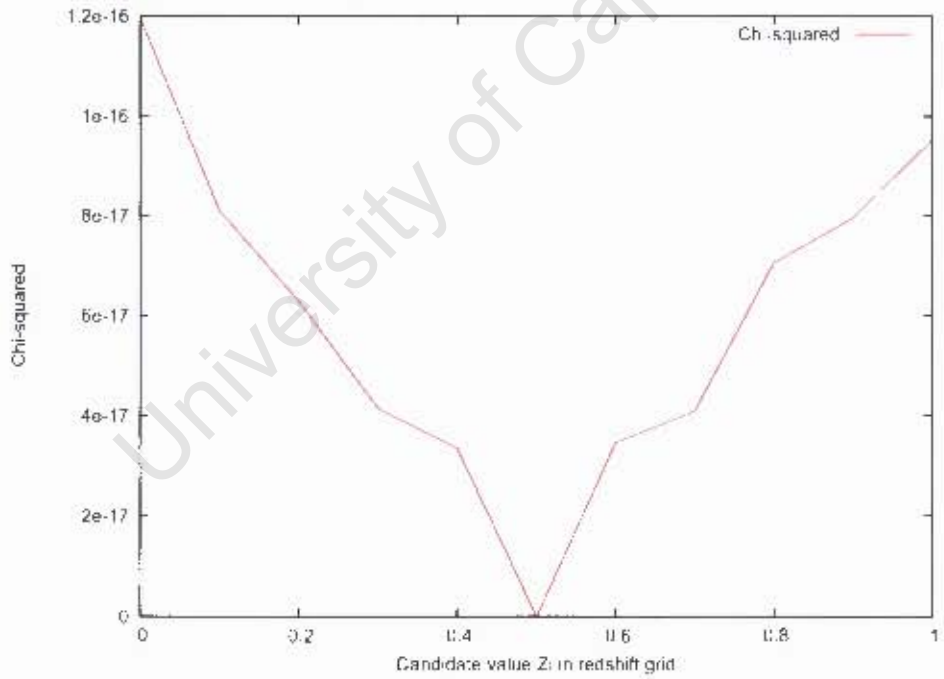

Figure 5.9: *Here we took the same template at phase = 5 and redshifted it by Z = 0.5. That redshifted spectrum is afterwards blueshifted by a serie of candidate redshifts Z_i taken from the predefined redshift grid given in input to the grid-based χ^2 code. Finally the square of the amplitude differences between the blueshifted output and the initial spectrum at phase = 5 (i.e the χ^2) is plotted. We expected the amplitude difference between both output to reach minimum at Z = 0.5, meaning that redshifting and blueshifting as described earlier do not particularly alter the data.*

Some results are summarized in tables 5.1, 5.2, 5.3 and associated plots for some of the tests performed and in tables 5.4, 5.5, 5.6, 5.7 and associated plots for the data obtained from the SUSPECT database of SNe. The testing phase consisted in redshifting a template of phase Φ by

Priors for the test	
Redshift range	[0.0,1.0]
Step size for redshift	0.1
Phase range (in Nugent basis)	[2,91]
Step size for phase	1
Results from the χ^2-test	
Best fit for redshift, z	0.5
Best fit for phase, Φ (in Nugent basis)	5
${\chi_{min}}^2 = {\chi_0}^2$	$4.93{\cdot}10^{-32}$
Duration of test (seconds)	6.2 on a 190 Mb (Ram), 1.6 Ghz laptop

Table 5.1: *The χ^2 minimization is used to identify the best fit and $\Delta\chi^2 = \chi^2 - \chi_0^2 = \{1, 4, 9, 16\}$ to identify $\{68.3\%, 95.4\%, 99.7\%, 99.9\%\}$ confidence regions around the minima. A template at phase = 5 has been redshifted by by z = 0.5. Step size for redshift and step size for phase are the step size in the redshift grid and the phase grid respectively. The exact values for the parameters have been found in this test*

Priors for the test	
Redshift range	[0.0,1.0]
Step size for redshift	0.01
Phase range (in Nugent basis)	[2,91]
Step size for phase	1
Results from the χ^2-test	
Best fit for redshift, z	0.05
Best fit for phase, Φ (in Nugent basis)	10
${\chi_{min}}^2 = {\chi_0}^2$	$8.628{\cdot}10^{-32}$
Duration of test (seconds)	35 on a 190 Mb (Ram), 1.6 Ghz laptop

Table 5.2: *In the present test, a template at phase = 10 is redshifted by z = 0.05. Step size for redshift and step size for phase are the step size in the redshift grid and the phase grid respectively. The exact values for the parameters have been found.*

a given redshift z and trying to find these parameters. In all the cases during the testing phase, the code almost perfectly recovered the information from the input spectrum.

5.4 Markov Chain Monte Carlo

The Markov Chain Monte Carlo (MCMC) is now a well established statistical method for constraining parameters from observed data. It is particularly adapted for high dimensional parameter space. There are different kinds of MCMC methods. Two of them are the Gibbs sampling and the Metropolis-Hastings algorithm (Metropolis *et al.*, 1953; Hastings, 1970). In this section, the Metropolis-Hastings algorithm has been implemented. It produces a "random walk" in likelihood space. One of the main advantages of MCMC is that the computational cost scales roughly linear with the number of parameters (Neal, 1993), meaning that it is a good strategy for the estimation of large number of parameters, as is often the case in cosmology.

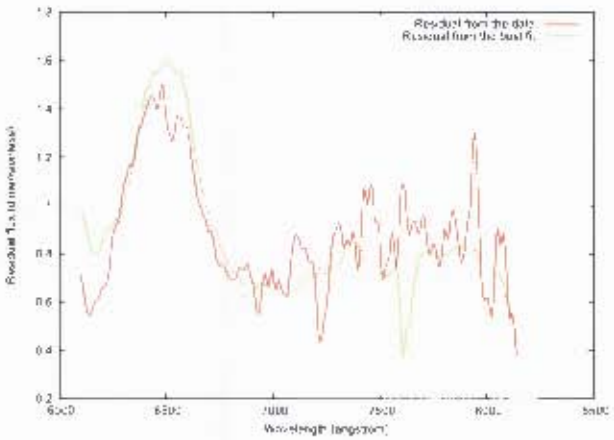

Figure 5.10: χ^2 *fitting from table 5.5, based on SN 1992ac, where the grid has been thinned. The best fit is now* 0.0001 *(0.3343 before in table 5.4) and* 42 *(4 before in table 5.4) for the redshift and the phase respectively. The expected fact, observable, is the improvement of the fit (estimate) once the grid has been thinned. In Nugent's basis, 20 is the phase for a template at B-band peak brightness, hence the matching template has a phase of* $42 - 20 = 22$ *in a frame of reference where the origin corresponds to the time of B-band peak brightness.*

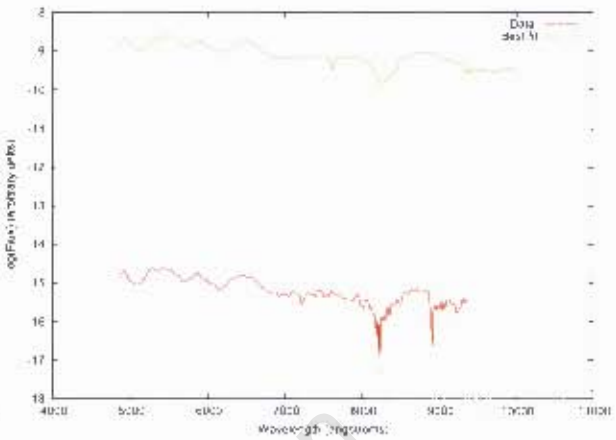

Figure 5.11: *Same* χ^2 *fitting from table 5.5. Plotted here are the unprocessed original data and best fit on a* $(\lambda, \log_{10}(F_\lambda))$ *scale. The large amplitude mismatch between input (flux* $\sim 10^{-15}$ *units) and template spectra (flux* $\sim 10^{-9}$ *units) is evident. The moving window averaging strategy was adopted to try to overcome that difficulty.*

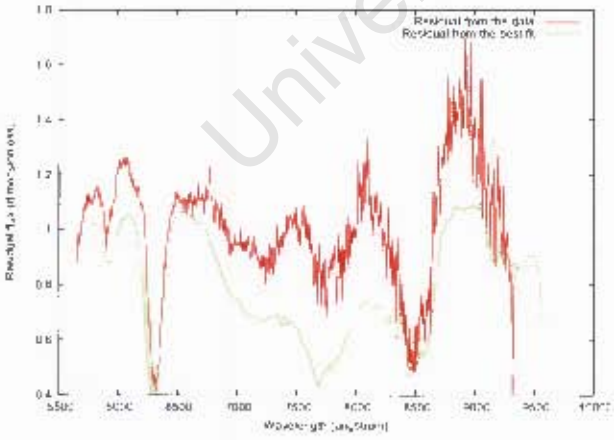

Figure 5.12: χ^2 *fitting from table 5.6, based on SN 2005eq, where the grid has been thinned using some prior information on the data. The best fit is* 0.026 *and* 23 *(Nugent basis) for the redshift and the phase respectively. The best fit has a phase of* $23 - 20 = 3$ *in a frame of reference where the origin corresponds to the time of B-band peak brightness.*

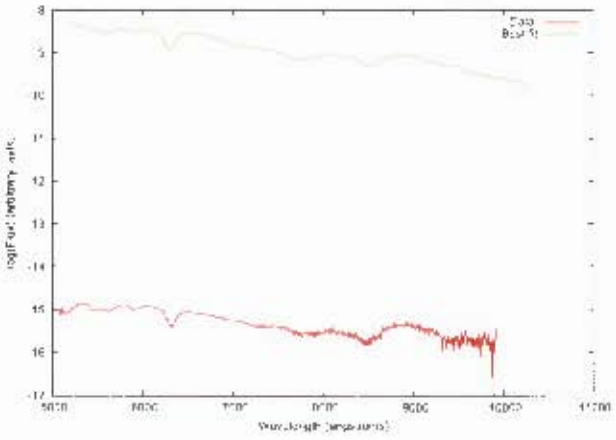

Figure 5.13: *Same* χ^2 *fitting from table 5.6. Plotted here are the unprocessed original data and best fit on a* $(\lambda, \log_{10}(F_\lambda))$ *scale.*

Priors for the test	
Redshift range	[0.0,1.0]
Step size for redshift	0.0001
Phase range (in Nugent basis)	[2,91]
Step size for phase	1
Results from the χ^2-test	
Best fit for redshift, z	0.0095
Best fit for phase, Φ (in Nugent basis)	90
${\chi_{min}}^2 = {\chi_0}^2$	$1.283 \cdot 10^{-26}$
Duration of test (minutes)	60 on a 190 Mb (Ram), 1.6 Ghz laptop

Table 5.3: *In the present test a template at phase = 90 was redshifted by z = 0.0095. Step size for redshift and step size for phase are the step size in the redshift and the phase grid respectively. The exact values for the parameters were obtained.*

Priors for the test	
Redshift range	[0.0,1.0]
Step size for redshift	0.0001
Phase range (in Nugent basis)	[2,91]
Step size for phase	1
Results from the χ^2-test	
Best fit for redshift, z	0.3343
Best fit for phase, Φ (in Nugent basis)	4
${\chi_{min}}^2 = {\chi_0}^2$	$4.15 \cdot 10^{-4}$
Duration of test (minutes)	32.7 on a 190 Mb (Ram), 1.6 Ghz laptop

Table 5.4: *A Type Ia spectrum from the SUSPECT database has been used. SN 1992ac, the SN Ia considered is at phase = 10 and has a redshift $z \sim 0.0523$. The phase of 10 is given with the peak brightness in B-band as the origin. Step size for redshift and step size for phase are the step size in the redshift and the phase grid respectively. The redshift estimate is clearly unsatisfactory. Same for the phase estimate. The incompleteness of Nugent's templates is suspected to be at the core of this difficulty. Thinning the grid is an additional option performed in table 5.5.*

5.4.1 Principle of Markov Chain Monte Carlo

The basic problem : one is given a vector of data **D** from which a vector of parameters Θ is to be estimated. In the MCMC approach, a large set of points Θ_i, i = 1,...,n ; a *chain* is generated by a stochastic procedure such that the points have the probability distribution $L(\Theta, D)$. To get the constraint on one single parameter, say Θ_1, one simply needs to marginalize over all the others, which in the case of MCMC consists of plotting an histogram of Θ_1.

5.4.2 Implemented Markov Chain Monte Carlo

The basic algorithm implemented

The Metropopolis-Hastings algorithm being used is the one defined as follows (Doran and Muller, 2004)

Priors for the test	
Redshift range	[0.0001,0.05]
Step size for redshift	0.0001
Phase range (in Nugent basis)	[2,91]
Step size for phase	1
Results from the χ^2-test	
Best fit for redshift, z	0.0001
Best fit for phase, Φ (in Nugent basis)	42
${\chi_{min}}^2 = {\chi_0}^2$	11.053
Duration of test (minutes)	2.15 on a 190 Mb (Ram), 1.6 Ghz laptop

Table 5.5: *Additional test on SN 1992ac, where the grid has been thinned. The redshift and the phase estimates remain unsatisfactory but, as expected, improving the priors on the redshift range of the data and thinning the grid improve the estimate.*

Priors for the test	
Redshift range	[0.001,0.05]
Step size for redshift	0.001
Phase range (in Nugent basis)	[2,91]
Step size for phase	1
Results from the χ^2-test	
Best fit for redshift, z	0.026
Best fit for phase, Φ (in Nugent basis)	23
${\chi_{min}}^2 = {\chi_0}^2$	99.825
Duration of test (seconds)	20.44 on a 190 Mb (Ram), 1.6 Ghz laptop

Table 5.6: *Here is highlighted again the interest of having some prior information on the data for the grid based χ^2-test. SN 2005cg, the SN Ia considered is at phase = 7 and has a redshift $z \sim 0.031$. The phase of 5 is given with the peak brightness in B-band as the origin. Step size for redshift and step size for phase are the step size in the redshift and the phase grid respectively.*

1. Choose starting point parameter vector Θ_o.
2. Compute the Likelihood $L(D|\Theta_0)$ of observing the experimental data D given the (vector of) parameters Θ_0.
3. Obtain a new parameter vector by sampling from (in our case) a Gaussian Distribution with mean 0 and standard deviation vector σ : How big the characteristic $\Delta\Theta$ jumps are in each vector of parameters is controlled by a vector [*step size for redshift* , *step size for phase*] (Each for a component of the parameter vector).
4. Construct $u_i = \Theta_{i-1} + \Delta\Theta_{i-1}$ (A vector equation).
5. Compute the Likelihood $L(D|u_i) = L_i$.
6. If $L_i \geq L_{i-1}$ then save u_i as a new "point" Θ_i in the chain ("take the step") and go to (3).

Priors for the test	
Redshift range	[0.001,0.05]
Step size for redshift	0.001
Phase range (in Nugent basis)	[2,91]
Step size for phase	1
Results from the χ^2-test	
Best fit for redshift, z	0.015
Best fit for phase, Φ (in Nugent basis)	62
${\chi_{min}}^2 = {\chi_0}^2$	253.8
Duration of test (seconds)	26 on a 190 Mb (Ram), 1.6 Ghz laptop

Table 5.7: *SN 2006gz, the SN Ia considered is at phase = 5 and has a redshift $z \sim 0.0236$. The phase of 5 is given with the peak brightness in B-band as the origin. Step size for redshift and step size for phase are the step size in the redshift and the phase grid respectively. The grid has been thinned using some prior knowledge on the redshift range of the data.*

7. If $L_i < L_{i-1}$ then generate a random variable u from [0,1]. If $u \leq \frac{L_i}{L_{i-1}}$ take the step as in (6). If $u > \frac{L_i}{L_{i-1}}$ then reject u_i, save Θ_{i-1} as a new "point" Θ_i in the chain and go to (3).

In that form a "random walk" in likelihood space is performed. The flow chart f the full code is given in figure 5.16. A general theorem establishes that the chain will approach regions of higher likelihood (Metropolis *et al.*, 1953; Hastings, 1970) after a variable amount of time.

Some relevant issues about the implemented code

By definition, the initial value for the redshift is a positive quantity. Hence, there is a prior information on the redshift. Therefore, at some point in the MCMC code, the χ^2 is set to take a large value whenever it has an input parameter vector with a negative redshift, so that such a candidate step is discarded. The detailed codes are given in the appendix.

5.4.3 Dominant problems and the solutions adopted for the MCMC

In practice , some difficulties are to overcome. Firstly, chosing the step size is probably the most important problem. As mentioned earlier, the most common strategy in MCMC consists of stochastically generating points Θ_i, i = 1, ..., n (i.e. a *chain*) such that the points have a known probability distribution. Usuallly one draws from a Gaussian distribution of mean zero and standard deviation σ (which gives the step size). The first difficulty is therefore to set a good standard deviation for the gaussian, which can vary from parameter to parameter. The code given in appendix takes into account two important prior information on the parameters to estimate :

- Each spectrum has a redshift somewhere between 0 and 1, hence for the redshift, a relevant stepsize in that range is chosen.
- Each spectrum has a phase somewhere between 15 days both before and after peak luminosity.

Because the estimated parameters (redshift and phase) are non-degenerate, there is no need to deal with cases where the χ^2-surface takes peculiar, banana-shaped forms i.e implementing an adaptive Gaussian sampling function (Doran and Muller, 2004; Tegmark *et al.*, 2004) is not necessary.

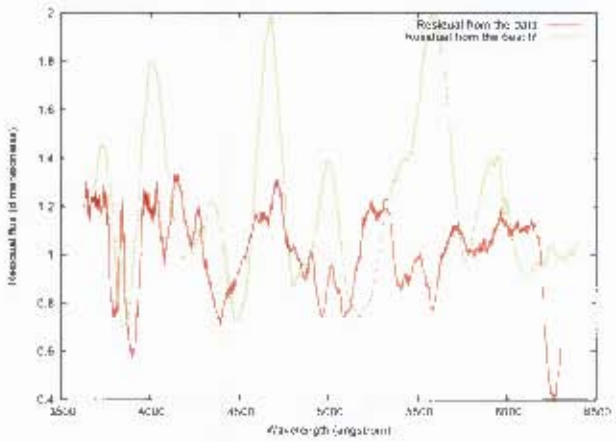

Figure 5.14: *χ^2 fitting from table 5.7, based on SN 2006gz, where the grid has been thinned using some prior information on the data. The best fit is 0.015 and 62 (Nugent's basis) for the redshift and the phase respectively. The best fit has a phase of $62 - 20 = 42$ in a frame of reference where the origin corresponds to the time of B-band peak brightness.*

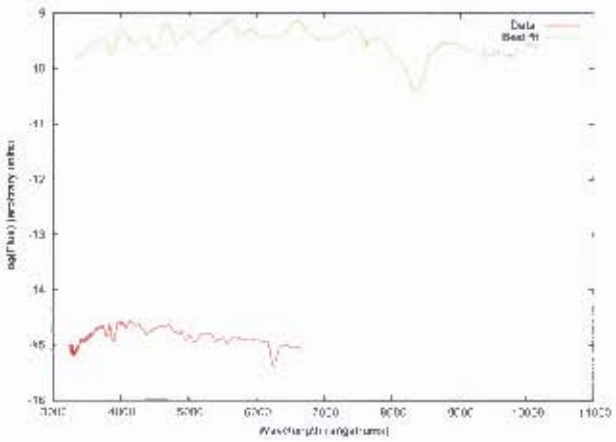

Figure 5.15: *Same χ^2 fitting from table 5.7. Plotted here are the unprocessed original data and best fit on a $(\lambda, \log_{10}(F_\lambda))$ scale.*

Secondly, the initial steps will not be drawn from the stationary distribution [3]. This problem is known as the *burn-in*, in such case, the steps are highly correlated with the starting point. To solve it, several chains are ran as done in the work by Tegmark et al. (2004). A calculation of the median likelihood of all chains combined is done, then as in (Tegmark *et al.*, 2004), the end of the burn-in for a given chain is defined as the first step where its likelihood exceeded the calculated median value. After discarding the burn-in, the independent chains are merged to produce the final chain. This standard procedure of concatenating independent chains is said to preserve their markov character, since they are completely uncorrelated (Tegmark *et al.*, 2004).

The next stage is to check for convergence. The primary aim is to know when is the chain drawing from the stationary distribution as well as if it has visited the whole region of interest. The test used here is the most famous one, the Gelman-Rubin test (Gelman and Rubin, 1992). A review of these tests is found in (Cowles and Carlin, 1996). Once the chain is being drawn from a stationary distribution, it has to run long enough to explore all the relevant parameter space and once done, the chain is said to be "mixed". A chain which moves rapidly through the parameter space so that this happens quickly is said to have "good mixing". Shot noise in the statistics inferred from the chain is also reduced by running longer. When the statistics accurately reflects the posterior distribution and the chain can be used reliably for parameter estimation, it is said to have "converged". In practice, convergence is often taken to have occured when the results derived from the chain are independent of its starting point. The Gelman-Rubin test used here is said to be a good test both for convergence and good mixing.

As done by (Hniopek, 2006); in implementing the convergence test and for practical reasons, M chains each having $2 * N$ points are considered. Then only the last N data points of each chain are taken and labelled as y_i^j where $i = 1, 2, ..., N$ and $j = 1, 2, ..., M$. One computes :

[3] When the chain finds the global minimum, it will stay in that region for most of the time and not travel too far away from the region of interest. One says that the chain draws from a stationary distribution , in other words, the chain has converged.

- The mean of each chain
- The mean of the whole set of chains

The next step involves the computation of :

- Bn, the variance between the M chains
- W, the variance within each chain as :

the Gelman-Rubin test consists in monitoring the quantity :

$$R = \frac{\frac{N-1}{N}W + Bn(1+\frac{1}{M})}{W}. \tag{5.6}$$

R goes asymptomatically towards 1. Convergence is obtained if R is always below a number somewhat slightly larger than 1, for all parameters. Because for long chains, R is approximately $1+\frac{Bn}{W}$, a value closer and closer to 1 states that the variance between the chains should be similar to the variance within the chain after convergence, i.e the chains are indistinguishable. And if the chains are indistinguishable, it is probably because they all draw from the stationary distribution. In (Gelman and Rubin, 1992), the quantity R containing the ratio of the within-chain and between-chain variances is such that at convergence, $R \sim 1.2$. In this work, convergence is assumed to have occurred when $R \sim 1.2$.

The speed with which a chain converges is strongly dependent on the proposal distribution, which in turn brings back to the step size problem. If too many large steps are proposed, the acceptance rate will be low as most steps will be away from the region of low χ^2 (high likelihood), and the chain will be stationary for long period of time. If too many small steps are proposed, most will be accepted but the chain will move slowly through parameter space.

A further check of convergence and good mixing is done using the autocorrelation of one of the parameters , say Θ^1, the redshift in the present case. Successive points of a same chain are highly correlated as each one is a small step away from the previous, i.e. a chain of N points does not systematically correspond to N different measurements. The quantity N_{eff}, the effective length, is monitored. It approximately corresponds to the number of unrelated point, i.e. N_{eff} different measurements (Tegmark *et al.*, 2004). A small N_{eff} means that the chain is not properly mixed (Gilks *et al.*, 1996). The autocorrelation c_j is defined as :

$$c_j = \frac{\sum_{k=1}^{N-j+1}\left(\Theta_k^1 - <\Theta^1>\right)\left(\Theta_{k+j-1}^1 - <\Theta^1>\right)}{\sum_{k=1}^{N-j+1}\left(\Theta_k^1 - <\Theta^1>\right)^2}, \tag{5.7}$$

where $<\Theta^1>$ is the mean value for the parameter Θ^1. By definition, $c_1 = 1$. The correlation length, c_l, is the index where the autocorrelation drops below a properly chosen value (a test value of 0.5 was chosen in the present case). The correlation length is the number of steps required so that data point Θ_{i+c_l} is independent of data point Θ_i. The effective length is then given by :

$$N_{eff} = \frac{N}{c_l}. \tag{5.8}$$

The easiest difficulty to overcome seems to be the length of the chain. The longer the chain, the better the output. Therefore, the code is ran with as many steps as possible, depending on the capacity of the computer used. In running the code presented below, the further check of convergence using the autocorrelation was disabled.

5.4.4 Application of a MCMC to the spectral characterization of Type Ia supernovae

A MCMC is performed on some Type Ia supernovae from SUSPECT, an online database of supernovae. The full code and the associated procedures and functions are given in the appendix. The flow chart for the algorithm is given in figure 5.16.

Some results

Inputs for the test	
Length of simulation	10 chains of 10 000 steps each
Redshift range for initial draw	[0.001,1.0]
Step size for redshift	0.1
Phase range for initial draw (in Nugent basis)	[5,35]
Step size for phase	1
Results from the MCMC simulation	
Convergence criterion, $R = (R_z; R_{phase})$	(1.0085 ; 1.0277)
Best fit for redshift, z	0.5
σ_z	0.0042
Best fit for phase, Φ (in Nugent basis)	5.1
σ_{phase}	1.43
${\chi_{min}}^2 = {\chi_0}^2$	0.0014
Duration of test (hours)	1.5 on a 190 Mb (Ram), 1.6 Ghz laptop

Table 5.8: *Test results from a MCMC simulation where a template at phase = 5 was redshifted by z = 0.5. The step size for redshift and the step size for phase are the jumps for the redshift and the phase parameter, respectively. σ_z and σ_{phase} are the 1-σ errors on the redshift and the phase, respectively.*

Inputs for the test	
Length of simulation	10 chains of 10 000 steps each
Redshift range for initial draw	[0.01,1.0]
Step size for redshift	0.1
Phase range for initial draw (in Nugent basis)	[8,12]
Step size for phase	1
Results from the MCMC simulation	
Convergence criterion, $R = (R_z; R_{phase})$	(1.0008 ; 1.0017)
Best fit for redshift, z	0.0502
σ_z	0.0029
Best fit for phase, Φ (in Nugent basis)	10.84
σ_{phase}	0.83
${\chi_{min}}^2 = {\chi_0}^2$	$4.89{\cdot}10^{-5}$
Duration of test (hours)	1.15 on a 190 Mb (Ram), 1.6 Ghz laptop

Table 5.9: *Test results from a MCMC simulation where A template at phase = 10 was redshifted by z = 0.05. The step size for the redshift and the step size for the phase are the jumps for the redshift and the phase parameter, respectively.* σ_z *and* σ_{phase} *are the 1-*σ *errors on the redshift and the phase, respectively.*

Inputs for the test	
Length of simulation	10 chains of 30 000 steps each
Redshift range for initial draw	[0.001,0.5]
Step size for redshift	0.1
Phase range for initial draw (in Nugent basis)	[5,35]
Step size for phase	1
Results from the MCMC simulation	
Convergence criterion, $R = (R_z; R_{phase})$	(1.0032 ; 1.0265)
Best fit for redshift, z	0.0262
σ_z	0.002
Best fit for phase, Φ (in Nugent basis)	24.287
σ_{phase}	1.117
${\chi_{min}}^2 = {\chi_0}^2$	99.681
Duration of test (hours)	3.32 on a 190 Mb (Ram), 1.6 Ghz laptop

Table 5.10: *Results from a MCMC simulation on SN 2005cg, a SN Ia. The input spectrum is from the SUSPECT database. SN 2005cg, the SN Ia considered is at phase = 7 and has a redshift* $z \sim 0.0310$. *The phase of 7 is given with the peak brightness in B-band as the origin. Step size for redshift and step size for phase are the jumps for the redshift and the phase parameter, respectively. Data covering well enough the blue and red part of the spectrum, like this one, seem more likely to be satisfactorily processed by the two codes.*

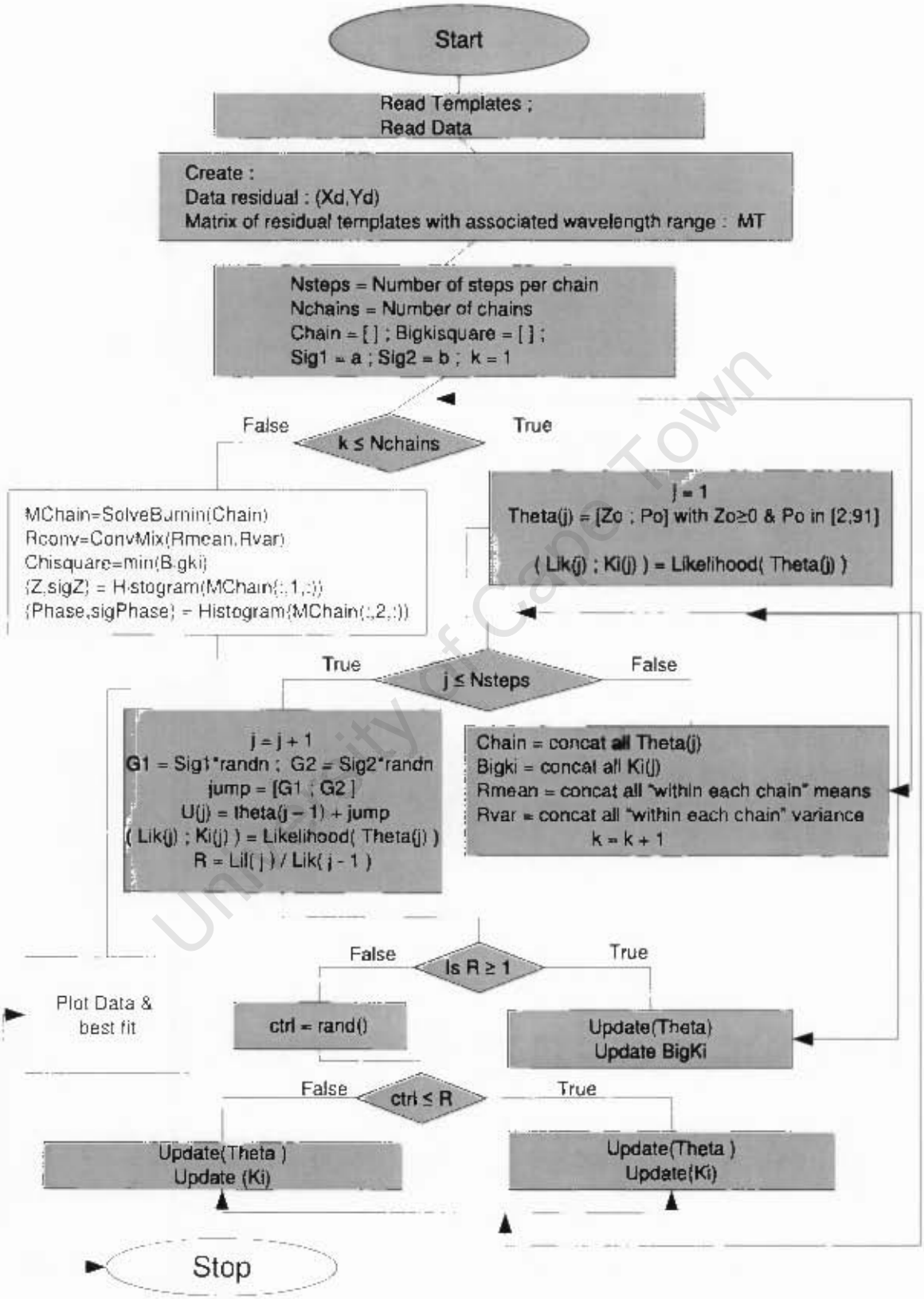

Figure 5.16: *Flow chart for the implemented MCMC code.*

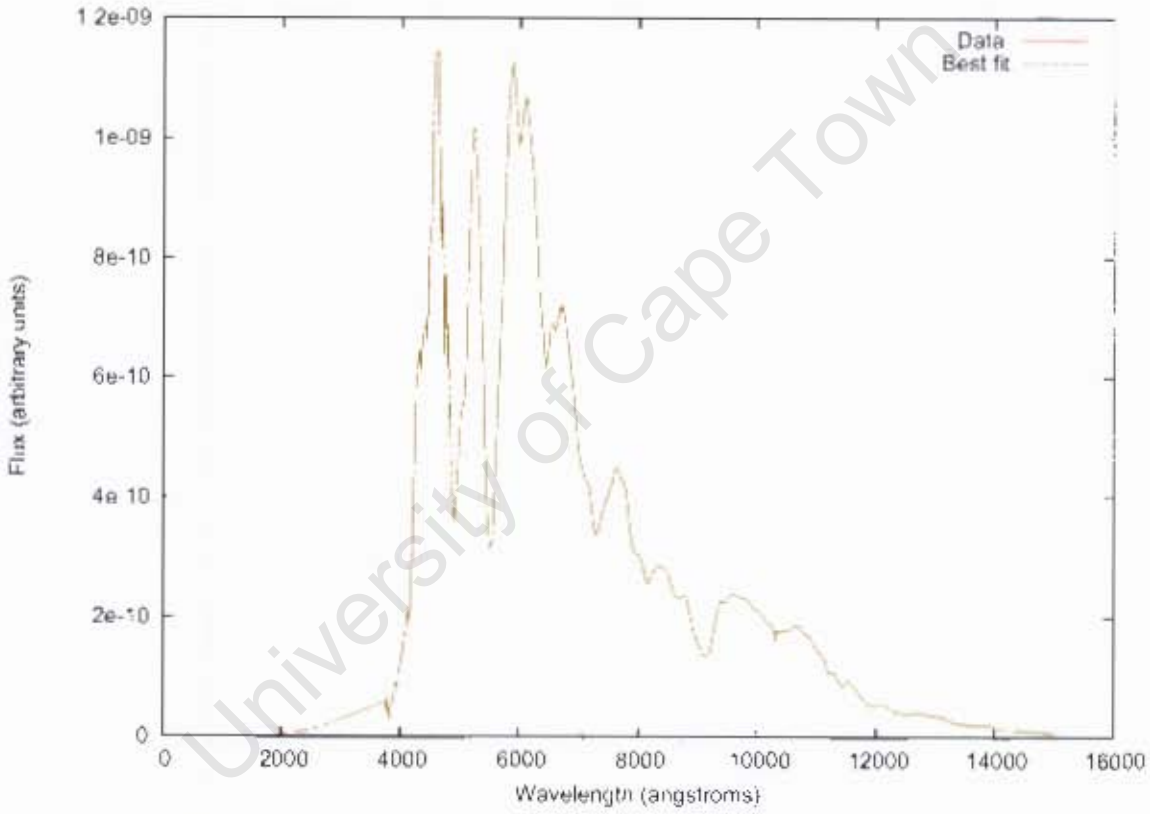

Figure 5.17: *MCMC fitting for the data used in table 5.8. A template at phase = 5 was redshifted by z = 0.5. The best fit is 0.5 (±0.0012) and 5.1 (±1.43) (Nugent basis) for redshift and phase, respectively. As expected, the values of the two parameters (redshift and phase) are almost exactly recovered in this test.*

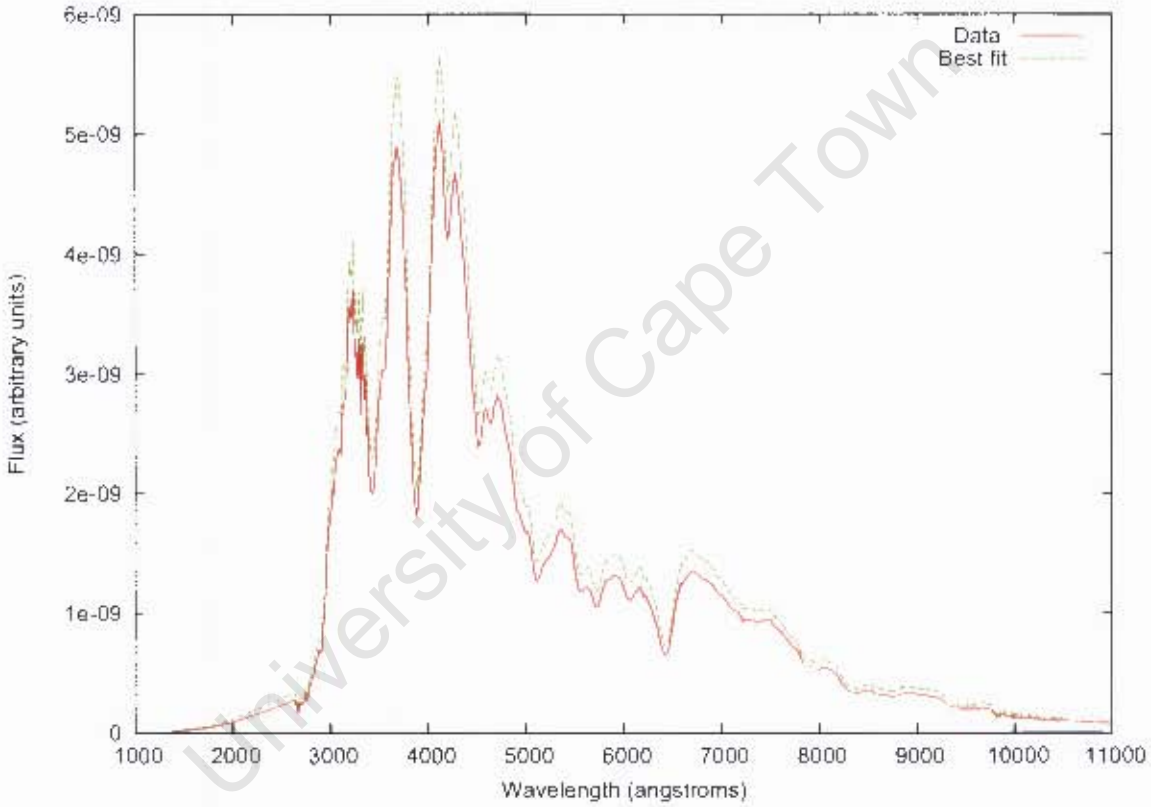

Figure 5.18: *MCMC fitting for the data used in table 5.9. A template at phase − 10 was redshifted by z = 0.05. The best fit is 0.0502 (±0.0029) and 10.84 (±0.83) (Nugent basis) for the redshift and the phase, respectively. The outcome is almost, considering the limitations associated to the cubic spline procedure heavily used in this code.*

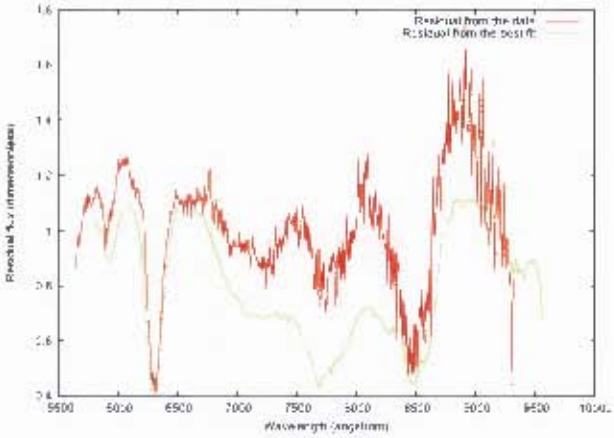

Figure 5.19: *MCMC fitting for the spectrum used in table 5.10. Plotted here are the residuals from both the data and the best fit. Compared to the data in table 5.11, these ones here do cover both the blue and the red side of the spectrum, resulting in a relatively satisfactory outcome. The best fit is 0.0262 (±0.002) and 24.287 (± 1.117) (Nugent basis) for the redshift and the phase, respectively. The best fit has a phase of 24.287 − 20 = 4.287 in a frame of reference where the origin corresponds to the time of B-band peak brightness.*

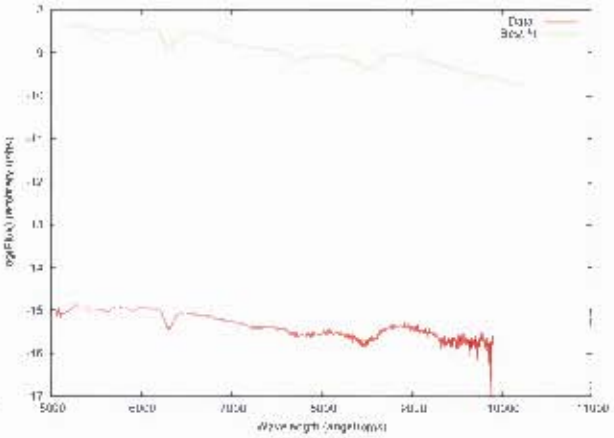

Figure 5.20: *Same MCMC fitting output as in table 5.10. Plotted here are the original unprocessed data and best fit on a $(\lambda, \log_{10}(F_\lambda))$ scale. The large amplitude mismatch between input (flux $\sim 10^{-15}$ units) and template spectra is evident (the best fit having flux $\sim 10^{-9}$ units).*

Inputs for the test	
Length of simulation	10 chains of 30 000 steps each
Redshift range for initial draw	[0.001,0.3]
Step size for redshift	0.1
Phase range for initial draw (in Nugent basis)	[2,91
Step size for phase	1
Results from the MCMC simulation	
Convergence criterion, $R = (R_z; R_{phase})$	(1.0062 ; 1.0109)
Best fit for redshift, z	0.0142
σ_z	0.002
Best fit for phase, Φ (in Nugent basis)	63.454
$\frac{\sigma_{phase}}{\chi_{min}{}^2 = \chi_0{}^2}$	0.965
	254.201
Duration of test (hours)	2.90 on a 190 Mb (Ram), 1.6 Ghz laptop

Table 5.11: *Results from a MCMC simulation on SN 2006gz, a SNe Ia. The input spectrum is from the SUSPECT database. SN 2006gz, the SN Ia considered is at phase = 5 and has a redshift $z \sim 0.0236$. The phase of 5 is given with the peak brightness in B-band as the origin. Step size for redshift and step size for phase are the jumps for the redshift and the phase parameter, respectively. As seen in figures 5.21 and 5.22, the particularity with this spectrum is that the data are mostly in the blue part where the quality of the templates is not uniform. good input data seem to be those covering weel enough the blue and the red part of the spectrum, as in table 5.10 and figure 5.19.*

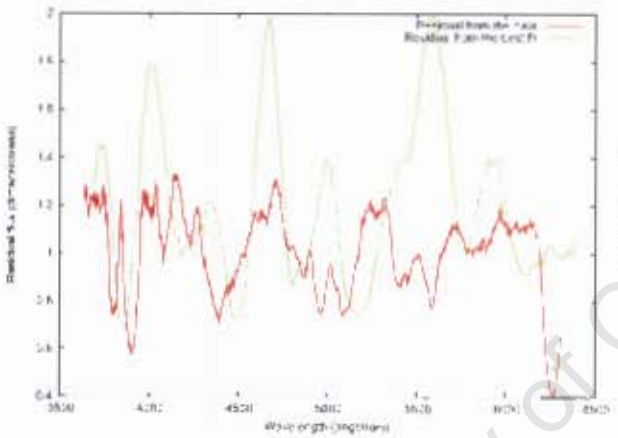

Figure 5.21: *MCMC fitting for the spectrum used in table 5.11. Plotted here are the residuals from both the data and the best fit. The input spectrum is mostly in the blue part where the quality of the templates is not uniform. As in table 5.10, having the data covering both wavelength range from blue to the red is an advantage. The best fit is 0.0142 (±0.0061) and 63.454 (±0.965) (Nugent basis) for the redshift and the phase, respectively. The matching template has a phase of 63.455 − 20 = 40.455 in a frame of reference where the origin corresponds to the time of B-band peak brightness.*

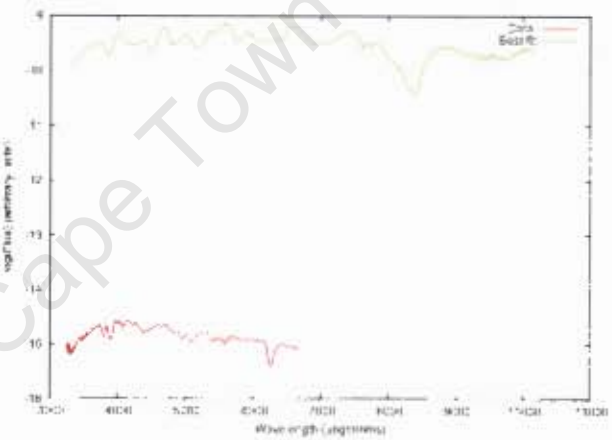

Figure 5.22: *Same MCMC fitting output as in table 5.11. Plotted here are the unprocessed original data and best fit on a* $(\lambda, \log_{10}(F_\lambda))$ *scale. The large amplitude mismatch between input (flux* $\sim 10^{-15}$ *units) and templates spectra remains (the best fit having flux* $\sim 10^{-9}$ *units).*

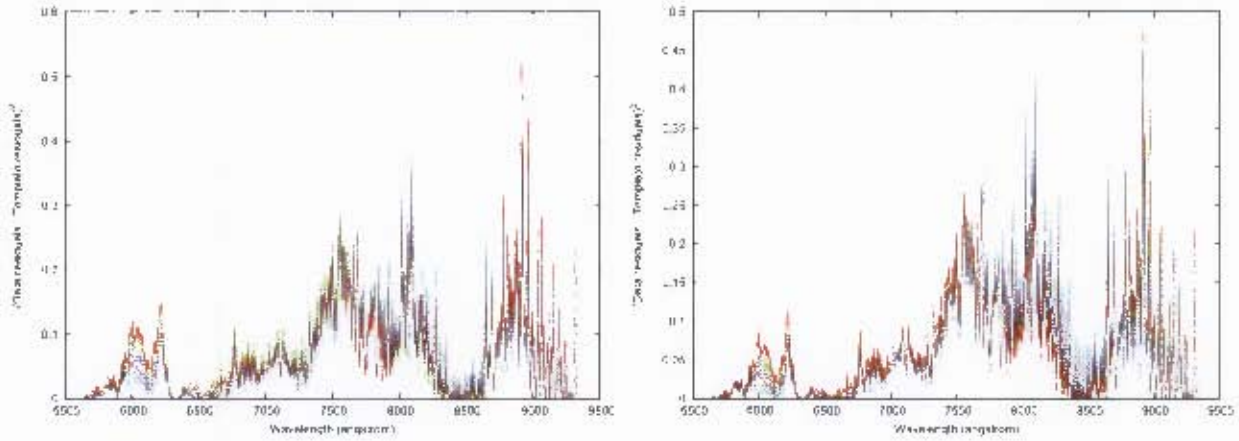

Figure 5.23: ***Left*** *: Comparison of some residuals from both the input data and a set of 05 templates including the best fit, in the case of the estimation performed in table 5.6 and figure 5.12.* ***Right*** *: Comparison of some residuals from both the input data and a set of 05 templates including the best fit, in the case of the estimation performed in table 5.10 and figure 5.19.*

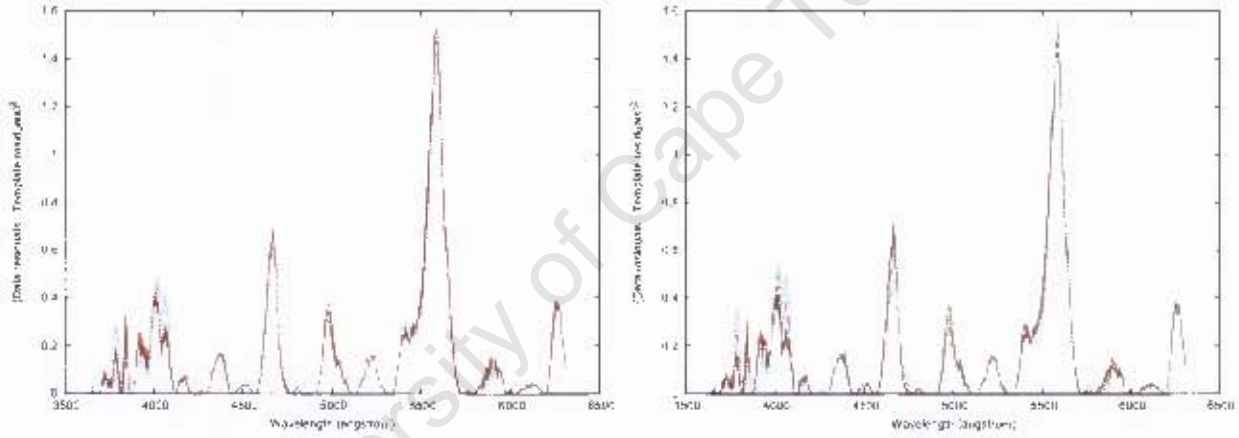

Figure 5.24: ***Left*** *: Comparison of some residuals from both the input data and a set of 05 templates including the best fit, in the case of the estimation performed in table 5.7 and figure 5.14.* ***Right*** *: Comparison of some residuals from both the input data and a set of 05 templates including the best fit, in the case of the estimation performed in table 5.11 and figure 5.21.*

In figures 5.23 and 5.24, the fact that Nugent templates are limited in scope and type is highlighted. The problems with the edges, the oscillating features, the overall shape of the template spectra and the wavelength range covered by the data make the fit particularly poor in some cases. A way out of that difficulty would be to widen the variety of SNe Ia used in creating the composite templates. That approach has been taken by authors like Blondin & al. in developing and testing the SuperNovae IDentification (SNID) code presented in the next chapter.

5.5 Summary

We have presented two codes based on the χ^2 statistic that can be used to estimate the redshift, z, of a given Type Ia supernova and its phase, Φ, from its spectrum using template spectra from (Nugent *et al.*, 2002). By phase it is meant the day from the time of peak B-band brightness. The first code is based on a grid strategy applied to the parameter space (z, Φ). The second code is an implementation of the Metropolis-Hastings algorithm for the Markov Chain Monte Carlo

method. Because the flux calibration process is not perfect or may not even have been done, the overall amplitude of the input spectrum does not coincide with the amplitudes and shape of the templates in general : we then speak of a mismatch. For this reason, the input spectrum and templates are pre-processed and their residuals are used instead to estimate (z, Φ). These residuals are obtained by dividing each spectrum by its associated smooth function obtained by averaging the spectrum over a moving window of 500 datapoints. For both codes, tests were made by redshifting some templates and recovering the initial redshift and phase, exactly in the grid case and within satisfactory error ranges in the case of MCMC for appropriate stepsize for each parameter. In real situations, successful estimates in both cases rely on the wavelength range of the input data (from blue to red being the ideal); the adequate use of some prior knowledge on the input data (range of redshift, phase) and computational power. Typical failures are due to the extent of overall amplitude discrepancies between input spectrum and templates; the sub-optimal behavior of the moving window averaging strategy in handling imperfections on spectra (e.g oscillating patterns) and the need for widening and varying the range and type of supernovae used in creating the composite templates. While they are a typical template set in the literature, Nugent's templates have been generated from only a few objects, some of them slightly atypical, making their general use difficult. This will be remedied by future data sets coming from SDSS, SNLS and other surveys.

Chapter 6

The SuperNovae IDentification (SNID) code

6.1 Introduction

Accurate redshift and phase estimates of Type Ia supernovae are of utmost importance when using them as standardizable candles for cosmology. In the absence of narrow lines in the host galaxy's spectrum, a statistical comparison of the input spectrum with template spectra is often performed. In this chapter, the public code SuperNovae IDentification (SNID) is presented. It is a tool recently developed by (Blondin and Tonry, 2006) and can be used to estimate the redshift and phase of a supernova spectrum as well as to place constraints on its type. By phase here it is meant the time (days) from the day of peak B-band brightness. SNID thus extends the techniques and codes presented in chapter **5**. The basic algorithm is from the correlation technique developed by (Tonry and Davis, 1979). The database of templates for SNID (SUSPECT[1] and CfA[2]) comprises 796 spectra of 64 SNe Ia, 172 spectra of 8 SNe Ib, 116 spectra of 9 SNe Ic, 353 spectra of 10 SNe II, as well as spectra of galaxies, AGNs, and variable stars (Blondin and Tonry, 2006).

6.2 Some elements on the theory of cross-correlation analysis

6.2.1 Introduction

Let $s(n)$ denotes the spectrum of a candidate supernova whose redshift is to be found. It can be cross-correlated with a template $t(n)$ (of known phase, type and redshift $z \sim 0$). The central goal is to determine the $(1+z)$ wavelength scaling to $t(n)$ that maximizes the cross-correlation :

$$c(n) = s(n) \times t(n), \tag{6.1}$$

where $\times$ denotes the cross-correlation product[3].

[1] *http : //bruford.nhn.ou.edu/~suspect/index1.html*

[2] *http : //www.cfa.harvard.edu/oir/Research/supernova/SNarchive.html*

[3] The cross-correlation product "$\times$" is related to the convolution product "$*$" by : $f(t) \times g(t) = f^{\star}(-t) * g(t)$ where $f^{\star}$ denotes the complex conjugate of f.

For practical reasons, the spectra are binned into N bins, labelled by bin number n. Bin number and wavelength are related by

$$n = A \cdot ln(\lambda) + B.$$

Hence, redshifting a template $t(n)$ by $(1 + z)$ is equivalent to adding a $ln(1 + z)$ shift to the logarithmic wavelength axis of $t(n)$. Any typical feature of the input or template spectrum (a characteristic absorption or emission line) at a given wavelength λ is identified by its bin number n.

Following that binning, a pre-processing of the inputs is performed. The aim is to remove any intrinsic color information in the input and template spectra, as well as making sure that the correlation is not excessively biased by reddening and statistical errors: the correlation output should only depend on the relative shape and strength of prominent spectral features in the input and template spectra. The application of a bandpass filter is the final stage. It aims to remove low-frequency residuals left over from the previous processing and high-frequency noise components (Blondin and Tonry, 2006). Both aspects are illustrated in figures 6.1 and 6.2.

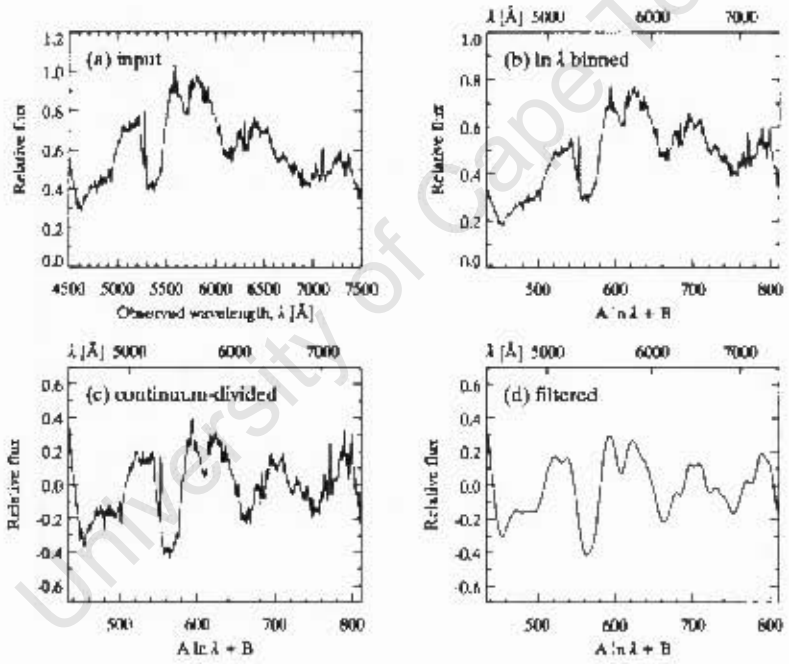

Figure 6.1: *Spectrum pre-processing. The input spectrum is (a) is linearly binned into N bins, labelled by bin number n, on a logarithmic wavelength scale (b) where n and wavelength λ are related by $n = A \cdot \lambda + B$ A pseudo-continuum is substracted (c) and the resulting spectrum is bandpass filtered (d) as illustrated in figure 6.2. Source: (Blondin and Tonry, 2006)*

6.2.2 Estimation of redshift

If $S(k)$ and $T(k)$ denote the discrete Fourier transforms corresponding to $s(n)$ and $t(n)$ respectively, then :

$$S(k) = \sum_{n=0}^{n=N-1} s(n) \cdot e^{\frac{-2\pi i n k}{N}}, \tag{6.2}$$

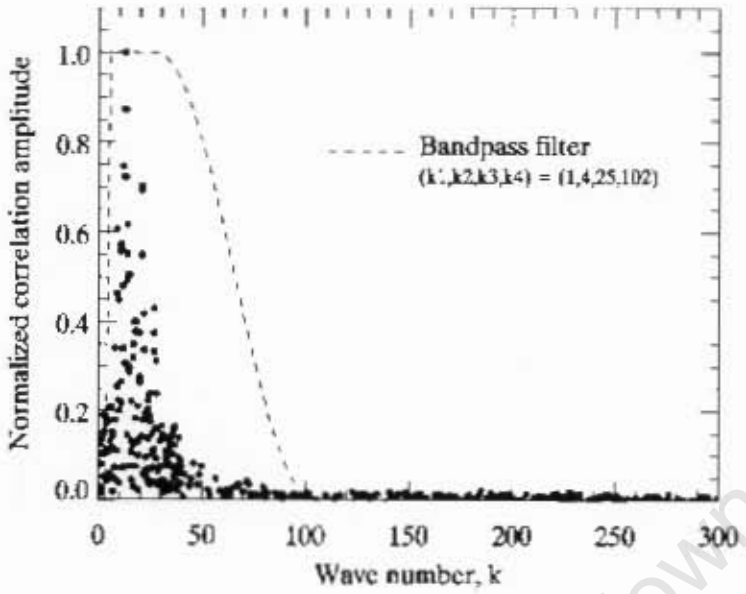

Figure 6.2: *Removing low-frequency residuals left over from the previous input pre-processing and high-frequency noise components . Source : (S. Blondin)*

and :

$$T(k) = \sum_{n=0}^{n=N-1} t(n) \cdot e^{-\frac{2\pi i n k}{N}}, \tag{6.3}$$

where N is the total number of bins used. The corresponding root-mean-squares (rms), σ_s and σ_t are given by :

$$\sigma_s^2 = \frac{1}{N} \sum_{n=0}^{n=N-1} s^2(n), \tag{6.4}$$

$$\sigma_t^2 = \frac{1}{N} \sum_{n=0}^{n=N-1} t^2(n), \tag{6.5}$$

For practical reasons, a normalized cross-correlation $c^*(n)$ is introduced and is given by :

$$c^*(n) = \frac{1}{N \cdot \sigma_s \cdot \sigma_t} \cdot c(n) = \frac{1}{N \cdot \sigma_s \cdot \sigma_t} \sum_m s(m) t(m-n). \tag{6.6}$$

Fourier transforming Eq.(6.6) leads to :

$$C(k) = \frac{1}{N \cdot \sigma_s \cdot \sigma_t} \cdot S(k) \cdot T^*(k), \tag{6.7}$$

where $T^*(k)$ is the complex conjugate of $T(k)$.

Because of Eq.(6.6), if $s(n)$ is exactly the same as $t(n)$ but shifted by β units, $s(n) \times t(n)$ will exhibit a peak equal to 1 at $n = \beta$. If perfect absolute calibration of the input spectrum is assumed , it is possible to suppose, like (Tonry and Davis, 1979) did; that $s(n)$, the input, is some multiple α of $t(n)$ broadened by convolution with a symmetric function $b(n)$ in such a way that :

$$s(n) \cong \alpha t(n) * b(n - \delta), \tag{6.8}$$

where "$*$" denotes the convolution product.

Figure 6.3 grossly illustrates the process. The principle of broadening by convolution is illustrated in figures 6.4, 6.5, 6.6 and 6.7.

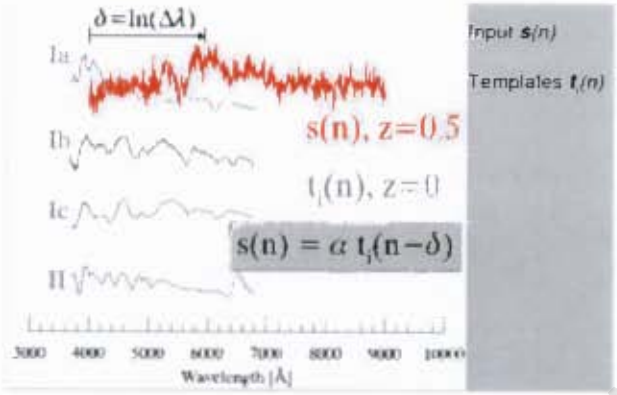

Figure 6.3: *Input and template spectrum cross-correlation basics. Assuming perfect absolute calibration of the input spectrum, the input can be seen as some multiple of $t(n)$ (with α as the factor) broadened by convolution with a symmetric function $b(n)$. Source : (S. Blondin)*

To estimate the parameters α and δ in Eq.(6.8), (Tonry and Davis, 1979) adopted a least square minimization performed by minimizing :

$$\chi^2(\alpha, \delta, b) = \sum_n [\alpha t*b(n-\delta) - s(n)]^2 . \tag{6.9}$$

Eq.(6.9) re-written in Fourier space gives :

$$\chi^2(\alpha, \delta, b) = \sum_k \left[\alpha T(k)B(k)e^{-\frac{2\pi i k\delta}{N}} - S(k)\right]^2 . \tag{6.10}$$

For simplicity the authors re-wrote Eq.(6.9) as :

$$\chi^2(\alpha; \delta; b) = \alpha^2 \sum t*b(n-\delta)^2 - 2\alpha \sum t*b(n-\delta)s(n) + \sum s^2(n) = \alpha^2 N\sigma^2_{t*b} - 2\alpha N\sigma_s\sigma_t c*b(\delta) + N\sigma^2_s, \tag{6.11}$$

where

$$\sigma^2_{t*b} = \frac{1}{N}\sum (t*b)^2$$

Minimizing with respect to α gives

$$\frac{\partial\chi^2}{\partial\alpha} = 2N\left[\alpha\sigma^2_{t*b} - \sigma_s\sigma_t c*b(\delta)\right] = 0$$

which brings

$$\alpha_{min} = \frac{\sigma_s\sigma_t}{\sigma^2_{t*b}} c*b(\delta)$$

Therefore

$$\chi^2(\alpha_{min}; \delta; b) = N\sigma^2_s\left(1 - \frac{\sigma^2_t}{\sigma^2_{t*b}}[c*b(\delta)]^2\right).$$

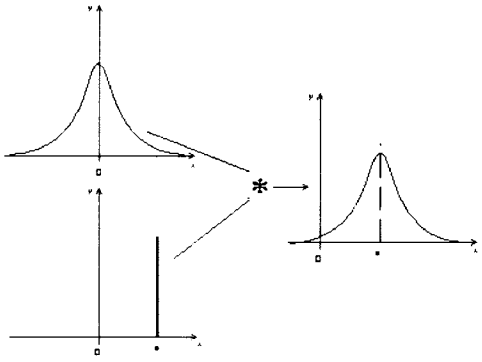

Figure 6.4: *A function f convolved with a Dirac delta function, δ_a. f has been "translated" by a. Source : (http : //fr.wikipedia.org/wiki/Produit_de_convolution)*

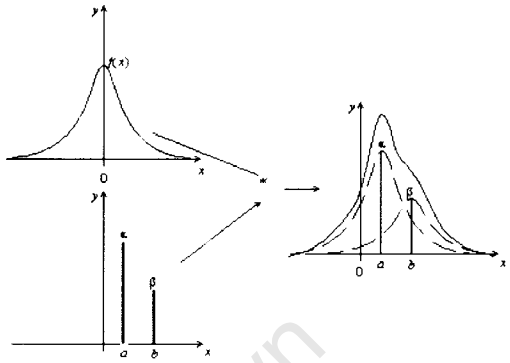

Figure 6.5: *A function f convolved with a sum of weighted Dirac delta functions. The final function is the original one "translated" and enlarged. Source : (http : //fr.wikipedia.org/wiki/Produit_de_convolution)*

.

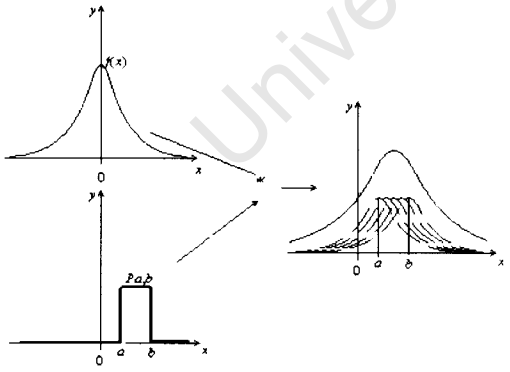

Figure 6.6: *A function f convolved with a given window function. The end product is obtained by "translating" the original function f all over the interval $[a, b]$ and then "enlargening" it. Source : (http : //fr.wikipedia.org/wiki/Produit_de_convolution)*

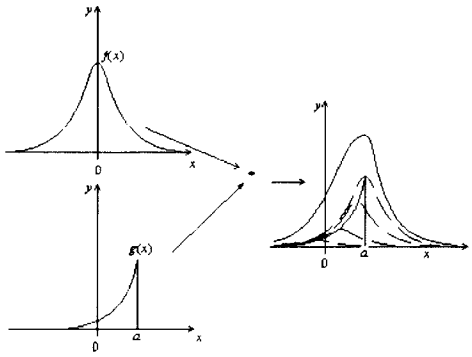

Figure 6.7: *A convolution product between two functions f and g. The end result is obtained by "translating" f and enlarging it according to each value of g. Source : (http : //fr.wikipedia.org/wiki/Produit_de_convolution)*

.

At that point, minimizing χ^2 is equivalent to maximizing

$$\frac{1}{\sigma_{t*b}} c*b(\delta)$$

From there, (Tonry and Davis, 1979) make some *suitable and realistic assumptions about b, c and t* :

1. $b(n)$ is a Gaussian centered on 0 with a dispersion of σ, i.e. $b(n) \sim Norm(0, \sigma)$ then $B(k) = e^{-\frac{(2\pi\sigma k)^2}{2N^2}}$,
2. $c(n)$ is approximately Gaussian shaped, centered at δ with dispersion μ, i.e. $c(n) \sim Norm(\delta, \mu)$ then $C(k) = \sqrt{2\pi}\mu c(\delta) e^{-\frac{(2\pi\mu k)^2}{2N^2}} e^{-\frac{2\pi i \delta k}{N}}$,
3. $\mid T(k) \mid \cong \sigma_t \left(\frac{2\pi N\tau}{\sqrt{\pi}}\right)^{\frac{1}{2}} e^{-\frac{(2\pi\tau k)^2}{2N^2}}$ i.e. the amplitude of Fourier transform of $t(n)$ is approximately Gaussian with τ, the width of the typical feature under consideration in $t(n)$ (or $S(n)$).

The approximation $\sum_n e^{-\frac{n^2}{\sigma^2}} \simeq \sigma\sqrt{\pi}$ leads to :

$$\sigma^2_{t*b} = \frac{1}{N}\sum (t*b)^2(n) = \frac{1}{N^2}\sum |T(k)B(k)|^2 = \sigma_t^2 \frac{\tau}{\sqrt{\sigma^2+\tau^2}}, \tag{6.12}$$

$$c*b(\delta) = \frac{1}{N}\sum_k C(k)B(k)e^{\frac{2\pi i\delta k}{N}} = c(\delta)\frac{\mu}{\sqrt{\mu^2+\sigma^2}}. \tag{6.13}$$

The realistic assumption of gaussian shape for $c(n)$ helps in the fact that by chosing δ as the center of the largest peak in $c(n)$ which is symmetric (as for any Gaussian), δ will also be the center of the largest peak in

$$\frac{1}{\sigma_{t*b}} c*b(\delta)$$

as $b(n) \sim Norm(0, \sigma)$. It was previously established that a suitable estimate for σ is found by maximizing $\frac{1}{\sigma_{t*b}} c*b(\delta)$ i.e solving

$$\frac{\partial}{\partial\sigma}\left(\frac{1}{\sigma_{t*b}} c*b(\delta)\right) = 2\sigma\frac{\partial}{\partial\sigma^2}\left(\frac{1}{\sigma_{t*b}} c*b(\delta)\right) = \frac{\mu\sigma}{2}\frac{c(\delta)}{\sigma_t\sqrt{\tau}}\left(\sigma^2+\tau^2\right)^{-\frac{3}{4}}\left(\sigma^2+\mu^2\right)^{-\frac{3}{2}}\left[\sigma^2+\mu^2-2\left(\sigma^2+\tau^2\right)\right] = 0$$

from Eqs.(6.12) and (6.13). The best δ minimizing χ^2 is then :

$$\sigma^2 = \mu^2 - 2\tau^2. \tag{6.14}$$

In their original application of the method to galaxy redshifts estimation, the authors sum up the all process by stating that "*the galaxy spectrum is correlated against the template spectrum and the resultant peak is fit by a smooth symmetric function (we use a quadratic polynomial). the central height of this fit determines α, the center is δ, and the width in conjunction with the width of the template provides σ* " (Tonry and Davis, 1979).

Error analysis - Redshift error and refining redshift estimates

The authors recognize the need to properly take into account the mismatch between input and template as the main contribution to the error budget. To formalize that, they introduce a "perturbed" version of the expression for $c(n)$ in Eq.(6.1) with a candidate for $s(n)$ of the type given

in Eq.(6.8) :

$$c(n) = s(n) \times t(n) \cong (h_0 t * b) \times t(n - n_0) + a(n). \tag{6.15}$$

The first term in the right hand is the exact correlated function between input spectrum and template and the second term is the distorsion introduced in the exact value by the mismatch between spectrum and template. The combination of both leads to the value of $c(n)$ as obtained in the previous section. $b(n)$ is normalized in such a way that

$$(t * b) \times t(0) = 1.$$

Because $c(n)$ is a normalized cross-correlation function, n_0 being the exact value for the perfect peak (i.e $c(n_0) = 1$) leads to

$$h_0 + a(n_0) = 1.$$

$a(n)$ is then a random function to be determined. $(t*b) \times t(n - n_0)$ is even about $n = n_0$ because $b(n)$ is even and any autocorrelation function[4] is even about 0. By consequence, the odd component of $c(n)$ about $n = n_0$ is the odd component of $a(n)$ about $n = n_0$. This brings :

$$\frac{1}{2}\left[c(n + n_0) - c(-n + n_0))\right] = \frac{1}{2}\left[a(n + n_0) - a(-n + n_0)\right]. \tag{6.16}$$

In practice n_0 is not precisely known but approximated by δ, and because this procedure gives no information about the symmetric part of $a(n)$, only the root-mean-square[5](rms) of the anti-symmetric part of $c(n)$ about δ is computed. If it is further assumed that $a(n)$ has even and odd components uncorrelated but of equal rms. Therefore, the rms of $a(n)$ is $\sqrt{2}$ times the rms of its antisymmetric component[6] (Tonry and Davis, 1979) :

$$\sigma_a^2 \cong \frac{1}{N}\frac{1}{2}\sum \left[c(n + \delta) - c(-n + \delta)\right]^2. \tag{6.17}$$

The (assumed) random behaviour of $a(n)$ alters the "exact peak" value obtained from :

$$(h_0 t * b) \times t(n - n_0). \tag{6.18}$$

ϵ, the (mean) error in the peak estimate is then defined as $\epsilon = |\delta - n_0|$ where δ is well estimated from Eq.(6.18). (Tonry and Davis, 1979) estimate the shift from "the exact peak" by interpolating Eq.(6.18) with parabolas, i.e :

$$(h_0 t * b) \times t(n - n_0) \cong h_0 \left[1 - \frac{2}{w_0^2}(n - n_0)^2\right] = h_0 + \eta, \tag{6.19}$$

where η is of appropriate type (here a 2nd order polynomial in $n - n_0$). In addition :

$$\delta = \frac{n_0 d_0 + n_1 d_1}{d_0 + d_1} \tag{6.20}$$

[4]The autocorrelation function is the cross-correlation of a function with itself

[5]In mathematics, the root-mean-square is the statistical measure of the magnitude of a varying quantity. It is especially useful when variates are alternatively positive and negative, e.g waves. By definition : $X_{rms} = \sqrt{< X^2 >}$ where $< X^2 >$ denotes the variance of the input signal X. In the case of a given population whose random variable X follows a given distribution, we have : $X_{rms}^2 =< X >^2 + \sigma_X^2$ $(http://en.wikipedia.org/wiki/Root\_mean\_square)$.

[6]Straightforward from both the definitions of rms and the expression of any function f in terms of its symmetric/even and antisymmetric/odd components as $f(x) = f_{symmetric/even} + f_{antisymmetric/odd} = \frac{f(x)+f(-x)}{2} + \frac{f(x)-f(-x)}{2}$.

is a general estimate for δ from the resulting peak in a parabola obtained by adding two parabolas centered at n_0 and n_1 with second derivatives $d_0(n_0)$ and $d_1(n_1)$. In the case of a quadratic interpolation, considering Eqs.(6.15) and (6.19), the "true peak" will have :

$$d_0 = -\frac{4h}{w^2}, \tag{6.21}$$

"whereas a typical peak in $a(n)$ has average height $\sqrt{2}\sigma_a$ and width w if we assume the power spectrum of $a(n)$ to be similar to that of $t*b\times t$" (Tonry and Davis, 1979). From Eq.(6.17) and considering - to first order - the nearest peak to n_0 in $a(n)$, one can show that the estimated mean distance from n_0 satisfies :

$$\mid n_1 - n_0 \mid \propto N. \tag{6.22}$$

As illustrated in figure 6.8, r, the ratio of the height of the true peak h to the average peak, $\sqrt{2}\sigma_a$ in $a(x)$ is introduced as :

$$r = \frac{h}{\sqrt{2}\sigma_a}. \tag{6.23}$$

(Blondin and Tonry, 2006) introduce the correlation r-value as :

$$r - value = \frac{h}{2\sigma_a}. \tag{6.24}$$

Considering equations 6.20, 6.21, 6.22 and 6.23; (Tonry and Davis, 1979) found that the mean error ,ϵ , in the peak estimate satisfies :

$$\epsilon = |\delta - n_0| \propto N\frac{1}{1+r}. \tag{6.25}$$

The precise coefficients multiplying $\frac{1}{1+r}$ can be adjusted so that the predicted error fits external errors gathered from other independent accurate estimation methods.

In Eq.(6.15) and because $c(n)$ is normalized; for a perfect correlation, a (true) peak will have $h = 1$ at the exact redshift Z_{true} i.e. when $n = n_0$. By definition of the cross-correlation $c(n)$, it will then be symmetric about that redshift Z_{true} (or equivalently about $n = n_0$) i.e. $c(n+n_0)-c(-n+n_0) = 0$ and the relation 6.16 leads to $\sigma_a = 0$ which implies that $r \rightarrow \infty$ by Eq. (6.24). In realistic terms that means that r will be small ($r < 3$) for a spurious correlation peak and large ($r \geq 8$) for a significant peak since in the latter case $h \simeq 1$ and σ_a necessarily small (Blondin and Tonry, 2006) as illustrated in figures 6.8 and 6.9.

In developing SNID, (Blondin and Tonry, 2006) went further by weighting the $r - value$ by the overlap, *lap* , in $ln(\lambda)$ space (figure 6.10) at the correlation redshift between input and template spectra. The overlap is complementary to the $r - value$ in conveying absolute information about the quality of the correlation. Correlation redshifts with an associated $lap < lap_{min} = 0/40$ and a combined $rlap = r\times lap < rlap_{min} = 5$ are usually discarded by the authors.

Redshift and phase estimate accuracy with SNID

Numerical simulations were performed by (Blondin and Tonry, 2006) to evaluate the accuracy of SNID in estimating the redshift and phase of a supernovae spectrum. The authors segregated the templates in the unique database, to avoid double use. *Only Type Ia supernovae were used.* The sample was made of $\sim$ 64 SNe Ia for which $\sim$ 796 spectra are available. Each input spectrum was

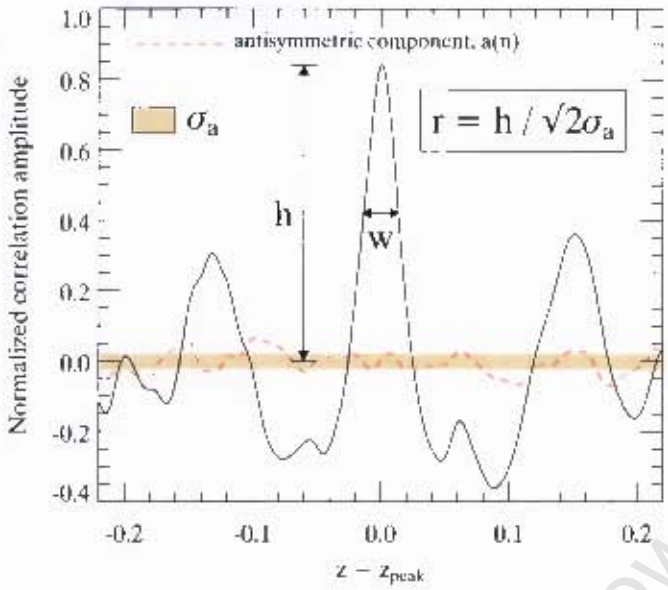

Figure 6.8: *r, the correlation r-value is defined as the ratio of the height, h, of the peak in the normalized function (solid line) to twice the rms, σ_a of its antisymmetric component. As did (Tonry and Davis, 1979), w, can be obtained by estimating the width of a typical peak in a(n) assuming its power spectrum is similar to the power spectrum of (t∗b)×t. Source : (Blondin and Tonry, 2006)*

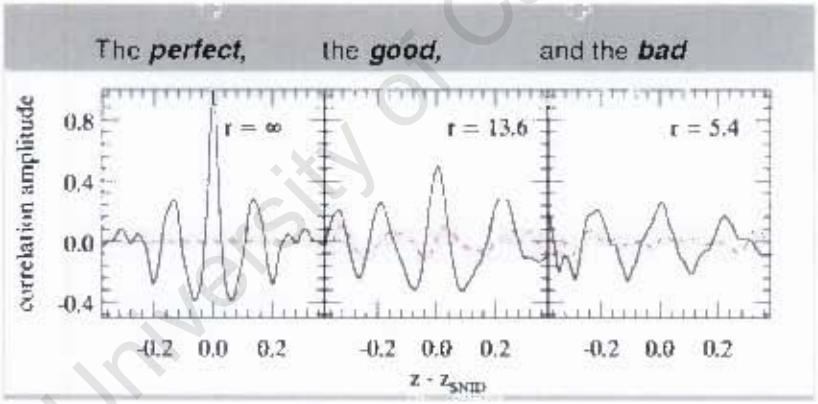

Figure 6.9: *Numerical simulations by (Blondin and Tonry, 2006) indicate that in realistic situations, r will be small (r < 3) for a spurious correlation peak, and large (r ≥ 8) for a significant peak. Source : (S. Blondin)*

randomly redshifted by $z \in [0.1, 0.7]$. Some noise was also added to mimic real data from $8-10$ m class telescopes typically used in cosmological SNe Ia surveys.

Based on these simulations, the authors showed that the typical errors on redshift and phase are respectively $\sigma_z < 0.01$ and $\sigma_t \leq 3$ days for $rlap - r - value \times lap \geq 5$. A further cross-checking was performed by comparing both the redshift from narrow emission/absorption lines in the host galaxy spectrum and SNID: 47 SNe Ia from the ESSENCE project with $0.164 \leq z \leq 0.781$. $\sigma \approx 0.006$ was the dispersion obtained on a one-to-one correspondence of the redshifts, in the range expected. It also appeared that good priors on redshift could improve the output on phase estimate and *vice versa*. Figures 6.11, 6.12, 6.13 and 6.14 show these results.

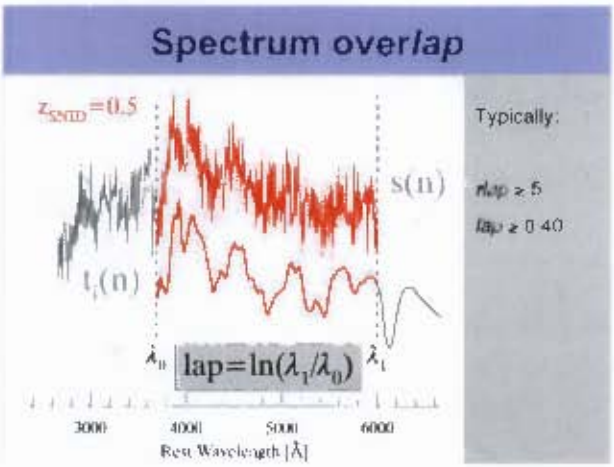

Figure 6.10: *The lap quantifies the overlap in rest wavelength between input and template spectrum, trimmed at correlation redshift. It is complementary to the $r-value$ in conveying absolute information about the quality of the correlation. Source : (S. Blondin)*

Type estimate accuracy with SNID

SNID could also be used to place reasonable constraints on the type of the input spectrum. The authors' preliminary strategy is based on the cumulative fraction of correlations exceeding a certain *rlap* cutoff. In testing the method via simulations, they focused on tackling two issues particularly relevant to ongoing SNe Ia searches at high redshift :

- The ability to distinguish between 1991T-like SNe Ia mentioned in section **4.2.4** and other Type Ia supernovae;
- The increasing difficulty to distinguish between type Ic supernovae and SNe Ia at high redshifts.

Their first results shown in figures 6.15 and 6.16, highlight the complementarity between spectroscopic and photometric observations for the classification of supernovae.

6.2.3 An example of spectral analysis with SNID

Here we test SNID on two Type Ia supernovae from the SUSPECT database; details given in table 6.1. In figures 6.17 a set of outputs without priors is presented. Two aspects are highlighted there :

- SNID is able to give a good estimate of both redshift and phase estimate in the absence of any prior. As a reminder, (Blondin and Tonry, 2006) established through simulations that ($\sigma_z \leq 0.01$) and ($\sigma_t \leq 3$ days) are typical dispersions for mostly SNe Ia.
- As with any other software, some regions of weaknesses do exist. An important one being related to how to reduce inaccuracies in the estimation of any of the two parameters (redshift and phase). Here, for the Type Ia SN 1992ac, while the phase estimate is reasonable, the redshift estimate is particularly unsatisfactory. An application is then made of the fact established by SNID's authors that simulations show a covariance between redshift and phase errors : In running SNID, the possibility is given to the user to enter an initial redshift

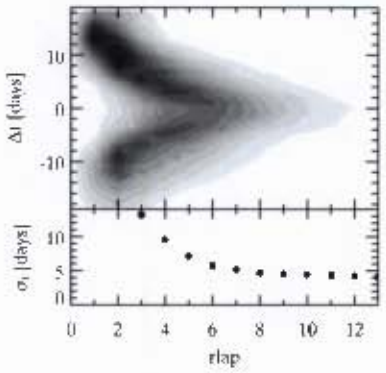

Figure 6.11: *Top: 2-D distribution of redshift residuals vs the rlap for input spectra satisfying* $0.3 \leq z \leq 0.5$; $-5 \leq phase[days] < +15$; $2 \leq SN!perAngstrom] \leq 10$. *The grayscale reflects the number of points in a given* $[\delta z, rlap]$ *2D bin (darker for more points). Only correlations with* $lap \geq 0.40$ *are shown. In case of good correlations (*$rlap \geq 5$*), the residuals distribution is almost a gaussian centered on* $\delta z = 0$. *Bottom: Standard deviation of redshift residuals,*σ_z*, in rlap bins of size unity. For* $rlap \geq 5$ *(i.e. good correlations),*$\sigma_z \leq 0.01$. *Source : (Blondin and Tonry, 2006)*

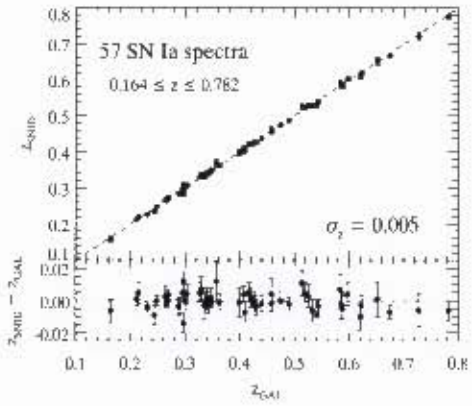

Figure 6.12: *Top: One-to-one correspondence between a supernova redshift (*Z_{SNID}*) and its host galaxy redshift (*Z_{GAL}*) as estimated with SNID.* σ_z*, the dispersion over the redshift range* $0.164 < z < 0.781$ *is* $\sigma_z \sim 0.006$. *Bottom: Redshift residuals vs* Z_{GAL}. *The ESSENCE project is the source of the 47 SNe Ia. Source : (Blondin and Tonry, 2006)*

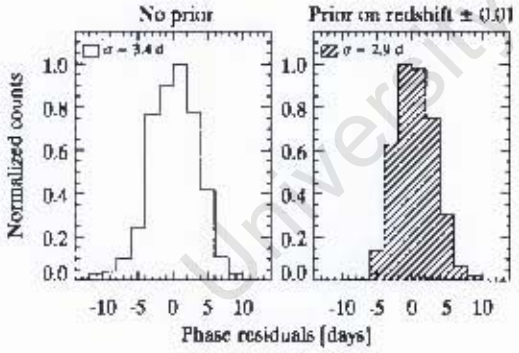

Figure 6.13: *Interplay between good redshift prior and phase estimate.* σ *is for* σ_t *the dispersion in the phase estimate. Simulations also showed that a* ± 3*-days prior on phase slightly improves the redshift estimate (*$\sigma_z = 0.006$ *to* $\sigma_z - 0.004$*) Source : (Blondin and Tonry, 2006)*

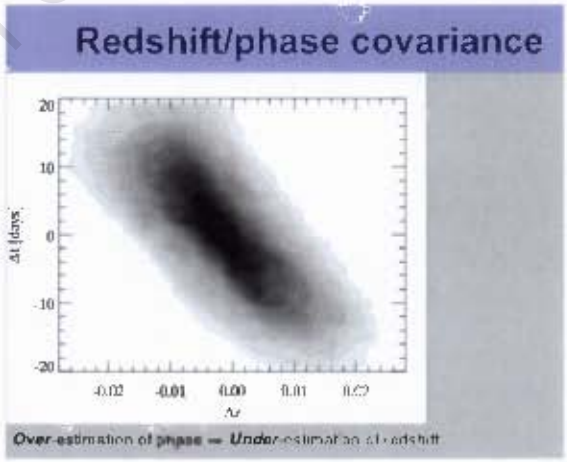

Figure 6.14: *Simulations show a covariance between redshift and phase erros which suggests that good priors on redshift could improve the output on phase estimate and vice versa. Source : (S. Blondin)*

estimate to be used by the code in the parameter estimation. Figures 6.18 are the outputs from SNID on SN 1992ac with two different initial values for the redshift : the first being a value far from the true one and the second is the exact redshift of the target (SN 1992ac) as given in the SUSPECT database. An improvement of the outcome with the refinment of the input initial redshift seems to be evident : an aspect worth more systematic investigations as shown by some tests whose results are given in table 6.2. One therefore foresees the

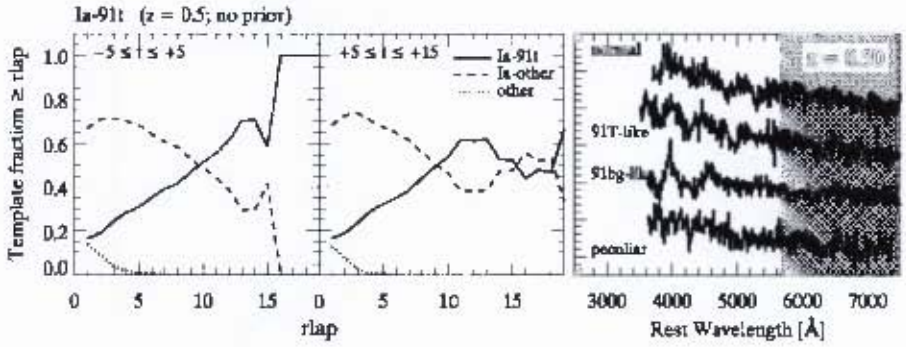

Figure 6.15: *Left panel : Identification of a 1991T-like SN Ia at $z = 0.5$, around maximum light and past maximum light (middle). The curves correspond to the fraction of templates of a given type greater than a given rlap value: 1991T-like SNe (solid); other SNe Ia (dashed); other SN types (dotted). The right panel shows representative maximum-light spectra of the various SN Ia subtypes, as observed with a typical optical spectrograph at $z = 0.5$ (Blondin and Tonry, 2006).*

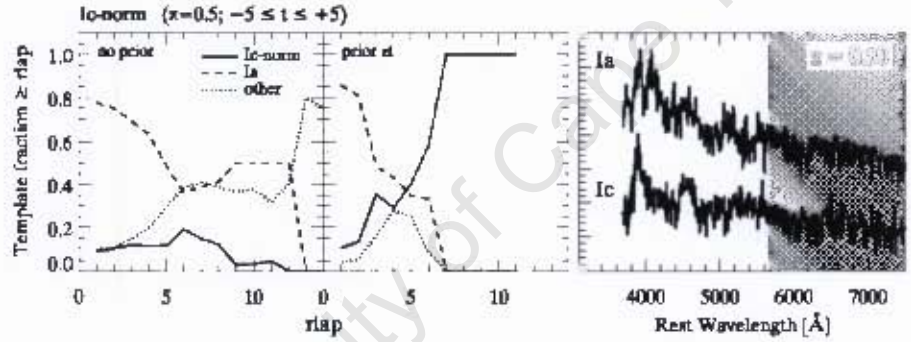

Figure 6.16: *Identification of a normal SN Ic around maximum light at $z = 0.5$, with no prior on redshift or phase (right), and with a flat ± 0.01 prior on redshift and a ± 3 days prior on the phase (middle). The curves correspond to the fraction of templates of a given type greater than a given rlap value: normal SNe Ic (solid); SNe Ia and SNe Ic, as observed with a typical optical spectrograph at $z = 0.5$ (Blondin and Tonry, 2006).*

possibility of using either a grid based χ^2 or a MCMC to get some candidate initial values for both the redshift and the phase and feed -where possible - SNID with them. Of relative importance is also the fact that the broader the pool and the quality of the templates the better the outcomes.

Identity	Redshift z as in the database	Phase (Peak magnitude in B-band is the origin) as in the database
2005cg	0.0310	5
1992ae	0.0523	10

Table 6.1: *Two Type Ia supernovae from the SUSPECT database to be characterized using SNID.*

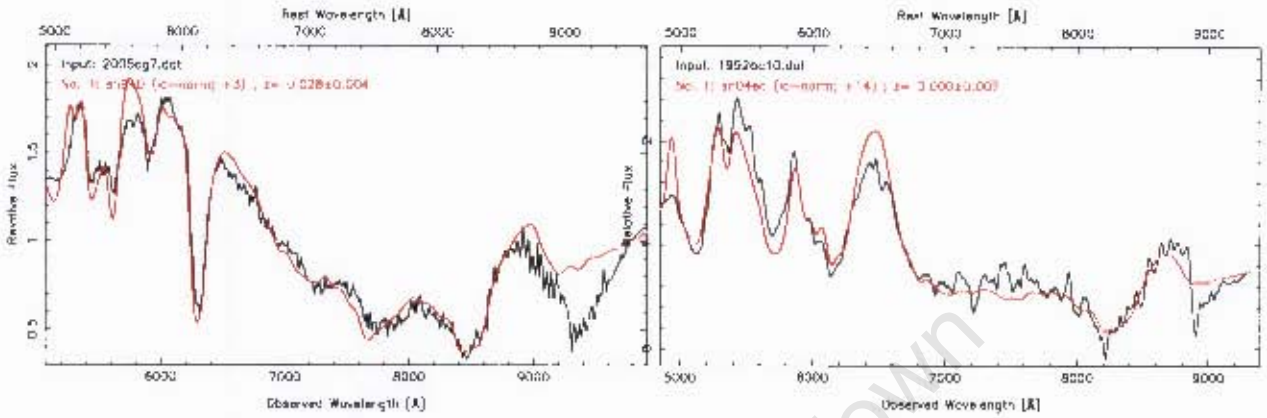

Figure 6.17: Graphical outputs for 2005eg and 1992ac using SNID. No initial value for the redshift (neither the phase) was considered for both SNe Ia. As seen in the second output, SNID as any other software does exhibit some weaknesses.

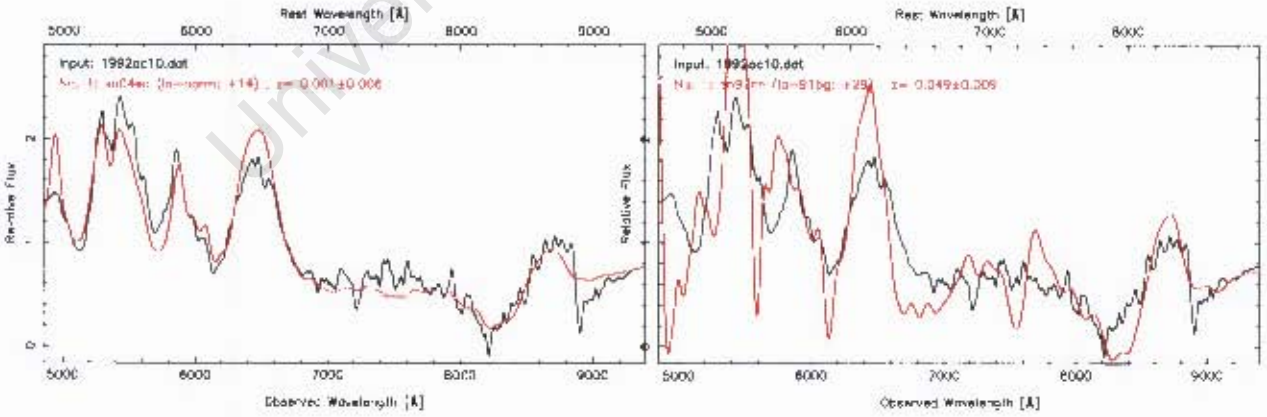

Figure 6.18: *Left* : 0.005, a value far from the true redshift of SN 1992ac is used as an initial redshift in input to SNID. *Right* : 0.0523, the true redshift as appearing in table 6.1 , is given an initial redshift. It seems that the more accurate the initial redshift given to SNID, the better the outcome for that parameter: an aspect worth a more systematic investigation. The quality of the outcome for the phase could be improved with an even wider range of templates.

Initial redshift entered, z_0	Outcome (template ID, type, phase and redshift estimate, z)
0.005	SN 04eo (Ia - normal, +14) ; $z = 0.001 \pm 0.006$
0.01	SN 04eo (Ia - normal, +14) ; $z = 0.001 \pm 0.007$
0.015	SN 96 (Ia - normal, +23) ; $z = 0.000 \pm 0.007$
0.025	SN 95al (Ia - normal, +25) ; $z = 0.002 \pm 0.008$
0.035	SN 95al (Ia - normal, +25) ; $z = 0.002 \pm 0.008$
0.05	SN 99aa (Ia - 91T , +54) ; $z = 0.014 \pm 0.009$
0.051	SN 97cn (Ia - 91bg, +29) ; $z = 0.049 \pm 0.009$
0.052	SN 97cn (Ia - 91bg, +29) ; $z = 0.049 \pm 0.009$
0.0523	SN 97cn (Ia - 91bg, +29) ; $z = 0.049 \pm 0.009$
0.055	SN 97cn (Ia - 91bg, +29) ; $z = 0.050 \pm 0.009$

Table 6.2: *SN 1992ac given in table 6.1 has its redshift and phase estimate relatively inaccurate in figure 6.17. We redo the test on SN 1992ac, with SNID, using various initial redshift z_0 ranging from an arbitrarily chosen to the exact value given in table 6.1 . The abbreviation "Ia" is for the type of supernova, "normal" indicates a normal Type Ia and "91T" and "91bg" refer to perculiar Type Ia as explained in the previous sections. Apparently, the more accurate the initial redshift z_0, the better the outcome for the redshift (z) and phase estimates. The need for a wider pool of templates is evident. One foresees the possibility of using either a grid based χ^2 or a MCMC to get initial values for both the redshift (and the phase) and feed -where possible - SNID with them.*

6.3 Summary

In chapter **5**, it was realised that widening and varying the range and type of supernovae spectra used in creating the composite templates was crucial in securing a satisfactory outcome from the spectral characterization of a given supernova. In looking at more complete strategies, cross-correlation techniques were introduced via the presentation of SuperNova IDentification code (SNID). SNID is an algorithm written by (Blondin and Tonry, 2006) from the correlation technique developed by (Tonry and Davis, 1979). Given a candidate spectrum, $s(n)$, and a template spectrum, $t(n)$, the central goal is to determine the $(1 + z)$ wavelength scaling to $t(n)$ that maximizes the cross-correlation $c(n) = s(n) \times t(n)$ where $\times$ denotes the cross-correlation product. For practical reasons, the spectra are binned into N bins. Contrary to the initial sample used by (Nugent *et al.*, 2002), the database for SNID (SUSPECT and CfA) comprises a larger and more varied collection of spectra as templates. As a result, SNID gives accurate estimates for redshift ($\sigma_z \leq 0.01$) and phase ($\sigma_t \leq 3$ days) for SNe Ia. SNID also allows the estimation of the type of the supernova under consideration, which in many cases is accurate. In running SNID, the possibility is given to the user to enter an initial redshift estimate to be used by the code in the parameter estimation. Because an apparent improvement of the outcome with the refinment of the input initial redshift seems evident, one foresees the possibility of using a χ^2-based test (grid or MCMC) as done previously, to obtain some initial values for both the redshift and the phase and to feed them -where possible - into SNID.

Chapter 7

Summary

The main purpose of this thesis is two-fold. Firstly to gain a better understanding of the theoretical and observational grounding of dark energy, the supposed driving force of the recently observed cosmic acceleration. Secondly it aims at exploring and learning parameter estimation strategies commonly used in modern cosmology. The parameter estimation is applied to the quantitative analysis of Type Ia supernovae (SNe Ia) spectra to estimate redshift and phase (relative to maximum brightness) of the SN Ia.

It is generally admitted that SNe Ia result from the explosion of a white dwarf having undergone a dwelling process by accreting matter from a companion star up to the Chandrasekhar limit. A growing concensus in the scientific community strongly points toward the use of SNe Ia as standardizable candles. The drive for the latter being their high luminosity, homogeneity and (quasi) ubiquity. SNe Ia were at the origin of the discovery of the accelerating universe. With the elusive dark matter already accounted for in the energy budget of the universe, SNe Ia indicated the need for an additio nal dark component with a negative equation of state. This challenging result has since been corroborated by estimates of the age of the universe which requires a non-zero dark energy component if consistency with current estimates of the Hubble constant is required. More recently, measurements of the geometry from the CMB, which suggest a flat universe, and studies of large scale structures pointing toward a preferred length scale in their clustering, have contributed to the stream of evidence implying the need for a non-zero dark component.

The challenges associated to sharpening SNe Ia as *standardizable candles* are related to the poor understanding of SNe Ia progenitors and to the lack of a relevant physics for dark energy. The dominant beliefs assume that dark energy might be caused by Einstein's cosmological constant, Λ, leading to the ΛCDM model; or by a time-varying scalar field rolling slowly down the potential and thus being dominated by the potential energy.

A rapidly growing sector of cosmology revolves around estimating characteristic parameters for the structure and the evolution of the universe. The more accurate the estimates, the better the constraints on the cosmology; hence the strong emphasis on bringing down the error budget associated to the data. This work revolves around parameter estimation from SNe Ia. We have developed two codes. The first code is based on a grid strategy for the parameter space and the second code is an implementation of the Metropolis-Hastingds algorithm for the a Markov Chain Monte Carlo method. The aim is to fit templates to spectra of SNe Ia from the SUSPECT database using Nugent templates. The fitting process allows us to estimate : (a) the redshift of a given SNe Ia; (b) the phase of the targeted SNe Ia in relation to the day of peak B-band brightness.

Successful estimates in both codes rely on the wavelength range of the input data (from blue to red being the ideal); the adequate use of some prior knowledge on the input data (range of redshift, phase) and computational power. Typical failures are due to the extent of overall amplitude discrepancies between input data and template spectra; the sub-optimal behavior of the moving window averaging strategy in handling imperfections on spectra (e.g oscillating patterns) and the need for widening and varying the range and type of supernovae used in creating the composite templates. In looking at more complete strategies, cross-correlation techniques were explored via the SuperNova IDentification code (SNID). SNID is an algorithm developed by (Blondin and Tonry, 2006) and gives promising estimates for redshift ($\sigma_z \leq 0.01$) and phase ($\sigma_t \leq 3$ days) of mostly SNe Ia. SNID also allows the estimation of the type of the supernova under consideration, which in many cases is accurate.

SNID and codes such as the ones we developed will remain a key part of Supernova cosmology in the coming decade as we push to higher redshifts and smaller systematics errors.

Bibliography

A. Aguirre. "Dust versus Cosmic Acceleration". *Astrophys. J., 512, L19* (1999).

J. Alcaniz and J. Lima. "New Limits on OmegaLambda and OmegaM from Old Galaxies at High Redshift". *Astrophys. J., 521, L87* (1999).

P. Astier, J. Guy *et al.* "The Supernova Legacy Survey: Measurement of OmegaM, OmegaLambda and w from the First Year Data Set". *arXiv:astro-ph/0510447* (2006).

T. Barreiro, E. Copeland and N. Nunes. "Quintessence arising from exponential potentials". *Phys. Rev. D, 61, 127301* (2000).

C. Bennett, M. Halpern and G. Hinshaw. "First-Year Wilkinson Microwave Anisotropy Probe (WMAP) Observations: Preliminary Maps and Basic Results". *Astrophys. J. Suppl., 148, p. 1* (2003).

L. Bergstrom and A. Goobar. *Cosmology and Particle Astrophysics.* Springer (2006).

M. Bessell. "UBVRI passbands". *PASP, 102, p. 1181* (1990).

H. A. Bethe. "Recent Evidence on the Nuclear Reactions in the Carbon Cycle." *Astrophys. J., 92, p. 118* (1940).

M. Blanc. *Recherche et étude des supernovae, mesure des taux d'explosion.* Ph.D. thesis, Université Paris XI (2002).

S. Blondin and J. Tonry. "Determining the Type, Redshift, and Phase of a Supernova Spectrum". *arXiv:astro-ph/0612512v1* (2006).

E. Bohm-Vitense. *Stellar Astrophysics Volume 3: Stellar structure and Evolution.* Cambridge University Press (1989).

E. Bowers, W. Geballe *et al.* "Infrared and optical spectroscopy of Type Ia Supernovae in the nebular phase". *MNRAS., 290, pp. 663 -679* (1997).

D. Branch, S. Perlmutter *et al.* "Coping with Type Ia Supernova "Evolution" when Probing the Nature of the Dark Energy". *arXiv:astro-ph/0109070* (2001).

M. Capellaro and M. Turatto. "A new determination of supernovae rates and a comparison with indicators for galactic star formation". *A & A, 351, pp. 459 - 466* (1999).

S. Chandrasekhar. "The maximum mass of ideal white dwarfs". *Astrophysical Journal* (1931).

J. Christensen-Dalsgaard. "Lecture notes on stellar structure and evolution". *Institut for Fysik og Astronomi, Aarhus University* (1995).

M. Colless, B. Peterson *et al.* "The 2dF Redshift Survey : Final Data Release". *arXiv:astro-ph/0306581* (2003).

G. Contardeo, B. Leibundgut and W. Vacca. "Epoch of maximum light and bolometric light curves of Type Ia Supernovae". *A & A., 359, pp. 876 - 886* (2000).

E. Copeland, A. R. Liddle and D. Wands. "Exponential potentials and cosmological scaling solutions". *Phys. Rev. D, 57, p. 4686* (1998).

E. J. Copeland, M. Sami and S. Tsujikawa. "Dynamics of Dark Energy". *arXiv:hep-th/0603057* (2006).

M. Cowles and B. Carlin. "Markov Chain Monte Carlo Convergence Diagnostics: A comparative Review". *Journal of the American Statistical Association* (1996).

W. de Sitter. *Proc. Akad. Weteush Amsterdam, 19, p. 1217* (1917).

S. Dodelson. *Modern Cosmology.* Academic Press (2003).

M. Doran and C. Muller. "Analyse This! A cosmological constraint package for cmbeasy". *arXiv:astro-ph/0311311* (2004).

P. Drell, T. Loredo and I. Wasserman. "Type Ia Supernovae, Evolution, and the Cosmological Constant". *Astrophys. J., 530, pp. 593 - 617* (2000).

J. Dunlop. "Old stellar populations in distant radio galaxies". *arXiv:astro-ph/9801114* (1998).

J. Dunlop, J. Peacock *et al.* "A 3.5-Gyr-old galaxy at redshift 1.55". *Nature, 381, p. 581* (1996).

D. Eisenstein, I. Zehavi *et al.* "Detection of the Baryon Acoustic Peak in the Large-Scale Correlation Function of the SDSS Luminous Red Galaxies". *Astrophys. J., 633, p. 560* (2005).

A. Filipenko. "Optical Spectra of Supernovae". *Annual Review of Astronomy and Astrophysics, 35, pp. 309-355* (1997).

D. Fixsen and J. Mather. "The Spectral Results of the Far-Infrared Absolute Spectrophotometer Instrument on COBE". *Astrophys. J., 581, p. 817* (2002).

G. Folatelli. *Type Ia supernova Cosmology : Quantitative Spectral Analysis.* Ph.D. thesis, Stockholm University, Department of Physics (2004).

R. Foley, A. Filipenko *et al.* "Constraining Cosmic Evolution of Type Ia supernovae". *arXiv:0710.2338v1v1* (2007).

W. Freedman, B. Madore *et al.* "Final Results from the Hubble Space Telescope Key Project to Measure the Hubble Constant". *Astrophys. J., 553, p. 47* (2001).

A. Gelman and D. Rubin. "Interference from Iterative Simulation using Multiple Sequences". *Statistical Science,7, p. 457* (1992).

W. Gilks, S. Richardson and D. Spiegelhalter. *Markov Chain Monte Carlo in Practice.* Chapman and Hall (1996).

A. Goobar and S. Perlmutter. "Feasibility of Measuring the Cosmological Constant Lambda and Mass Density Omega using Type Ia Supernovae". *arXiv:astro-ph/9505022* (1995).

I. Gradshteyn, I. Ryzhik *et al.* *Table of Integrals, Series, and Products.* Academic Press (2007).

M. Hamuy and et al. "The 1990 Calan/Tololo supernovae search". *Astron. J., 106(6), pp. 2392-2407* (1993).

M. Hamuy, M. Phillips *et al.* "A Hubble Diagram of distant Type Ia supernovae". *Astron. J., 109, 1669, pp. 1-13* (1995).

M. Hamuy, M. Phillips *et al.* "The Morphology of Type-Ia Supernovae Light Curves". *Astron. J., 112, p. 2438* (1996).

S. Hannestad and E. Mortsell. "Cosmological constraints on the dark energy equation of state and its evolution". *arXiv:astro-ph/0407259* (2004).

B. Hansen, J. Brewer *et al.* "The White Dwarf Cooling Sequence of the Globular Cluster Messier 4". *Astrophys. J., 574, L155* (2002).

D. Hardin, C. Afonso *et al.* "Type Ia supernovae rate at z $\sim$ 0.1". *A & A , 362, pp. 419 - 425* (2000).

W. Hastings. "Monte Carlo Sampling Methods Using Markov Chains and Their Applications". *Biometrika, 57, p. 97* (1970).

W. Hillebrandt and J. Niemeyer. "Type Ia Supernovae explosion Models". *Annual Review of Astronomy and Astrophysics, 38, p. 191* (2000).

G. Hinshaw. "Data Analysis for the Microwave Anisotropy Probe (MAP) Mission". *arXiv:astro-ph/0011555* (2000).

G. Hinshaw, D. Spergel *et al.* "First-Year Wilkinson Microwave Anisotropy Probe (WMAP) Observations: The Angular Power Spectrum". *Astrophys. J. Suppl., 148, p. 135* (2003).

K. Hniopek. *Investigating the dark energy using a Markov Chain Monte Carlo.* Master's thesis, Department of Astronomy, Stockholm University (2006).

F. Hoyle, G. Burbidge and J. Narlikar. *A Different Approach to Cosmology.* Cambridge University Press (2000).

E. Hubble. "A Relation between Distance and Radial Velocity among Extra-Galactic Nebulae". *Proc. Natl. Acad. Sci., 15, p. 168* (1929).

G. Hutsi. *Cosmic Sound: Measuring the Universe with baryonic acoustic oscillations.* Ph.D. thesis, Fakultat fur Physik der Ludwig-Maximilians-Universitat Munchen (2006).

K. Ichikawa and T. Takahashi. "Dark Energy Evolution and the Curvature of the Universe from Recent Observations". *arXiv:astro-ph/0511821* (2005).

G. Jacoby, D. Branch *et al.* "A critical review of selected techniques for measuring extragalactic distances". *PASP, 104, pp. 599 - 662* (1992).

R. Jimenez, P. Thejll *et al.* "Ages of globular clusters: a new approach". *MNRAS, 282, p. 926* (1996).

A. Kamenshchik, U. Moshella and V. Pasquier. "An alternative to quintessence". *Phys. Lett. B, 511, p. 265* (2001).

A. Kim, A. Goobar and S. Perlmutter. "A Generalized K-correction for Type Ia Supernovae: Comparing R-band Photometry beyond z = 0.2 with B, V, and R-band Nearby Photometry." *PASP, 108 - 190* (1996).

R. Kirshner and J. Kwan. "Distances to extragalactic supernovae". *Astrophys. J., 193, pp. 27-36* (1974).

R. Knop, G. Aldering *et al.* "New Constraints on OmegaM, OmegaLambda and w from an Independent Set of Eleven High-Redshift Supernovae Observed with HST". *arXiv:astro-ph/0309368* (2003).

L. Krauss. "Old Galaxies at High Redshift and the Cosmological Constant". *Astrophys. J., 480, p. 466* (1997).

B. Leibundgut. "Type Ia Supernovae". *A & A., 245, pp. 179 - 209* (2000).

J. Mather, E. Cheng *et al.* "A preliminary measurement of the cosmic microwave background spectrum by the Cosmic Background Explorer (COBE) satellite". *Astrophys. J., 354, L37* (1990).

J. Mather, D. Cottingham *et al.* "Measurement of the cosmic microwave background spectrum by the COBE FIRAS instrument". *Astrophys. J., 420, p. 439* (1994).

N. Metropolis, A. Rosenbluth *et al.* "Equation of State Calculations by Fast Computing Machines." *Journal of Chemical Physics, 21, p. 1087* (1953).

R. Minkowski. "Spectra of Supernovae". *PASP, 53, p. 224* (1941).

R. Neal. "Probabilistic Inference Using Markov Chain Monte Carlo Methods". *Department of Computer Science, University of Toronto* (1993).

J. Niemeyer, M. Reinecke *et al.* "Small steps Towards Realistic Explosion Models of Type Ia Supernovae". *In From Twilight to Highlight: The Physics of Supernovae* (2003).

K. Nomoto, K. Iwamoto and N. Kishimoto. "Type Ia Supernovae : Their origin and possible applications in cosmology". *Science, 276, pp. 1378 - 1382* (1997).

P. Nugent, A. Kim and S. Perlmutter. "K-corrections and Extinction corrections for type Ia Supernovae". *arXiv:astro-ph/020535v1* (2002).

T. Padmanabhan. "Cosmological Constant - the Weight of the Vacuum". *arXiv:hep-th/0212290* (2003).

L. Page, M. Nolta *et al.* "First-Year Wilkinson Microwave Anisotropy Probe (WMAP) Observations: Interpretation of the TT and TE Angular Power Spectrum Peaks". *Astrophys. J. Suppl., 148, p. 233* (2003).

R. Pain, S. Fabbro *et al.* "The Distant Type Ia Supernovae Rate". *Astrophys. J., 577, pp. 120 - 132* (1999).

F. Patat, S. Benedetti *et al.* "The type IA supernova 1994D in NGC 4526: the early phases". *MNRAS, 278, p. 111* (1996).

J. Peacock, J. R *et al.* "Old high-redshift galaxies and primordial density fluctuation spectra". *MNRAS, 296, p. 1089* (1998).

S. Perlmutter, G. Aldering *et al.* "Discovery of a Supernovae explosion at half the age of the Universe". *Nature, 391, p. 51* (1998).

S. Perlmutter, G. Aldering *et al.* "Measurements of Omega and Lambda from 42 High-Redshift Supernovae". *Astrophys. J., 517, pp. 565-586* (1999).

S. Perlmutter, G. Gabi *et al.* "Measurements of the Cosmological Parameters OmegaM and OmegaLambda from the first seven supernovae at z > 0.35". *Astrophys. J., 483, pp. 565-581* (1997).

S. Perlmutter and B. Schmidt. "Measuring Cosmology with Supernovae". *In LNP Vol. 598 : Supernovae and Gamma-Ray Bursters, p. 195* (2003).

M. Phillips. "The Absolute Magnitude of Type Ia Supernovae". *Astrophys. J. Suppl., 413, L105 - L108* (1993).

M. Phillips, P. Lira *et al.* "The Reddening - Free Decline Rate Versus Luminosity Relationship for Type Ia Supernovae". *Astron. J., 118, pp. 1766 - 1778* (1999).

W. Press, B. Flannery *et al. Numerical Recipes in FORTRAN: The Art of Scientific Computing.* Cambridge University Press (1992).

I. Pskovskii. "Light curves, color curves, and expansion velocity of type I supernovae as functions of the rate of brightness decline". *Soviet Astronomy, pp. 675 - 682* (1977).

H. Richer, J. Brewer *et al.* "The Lower Main Sequence and Mass Function of the Globular Cluster Messier 4". *Astrophys. J., 574, L151* (2002).

M. Richmond, R. Treffers *et al.* "UBVRI Photometry of the Type IA SN 1994D in NGC 4526". *Astron. J., 109, p. 2121* (1995).

A. Riess, A. Filipenko *et al.* "Observational Evidence from supernovae for an Accelerating Universe and a Cosmological Constant". *Astron. J., 116, p. 1009* (1998).

A. Riess, R. Kirshner *et al.* "BVRI Light Curves for 22 Type IA Supernovae". *Astron. J., 117, p. 707* (1999).

A. Riess, W. Press and R. Kirshner. "Using SNIa Light Curve Shapes to Measure the Hubble Constant". *arXiv:astro-ph/9410054* (1994).

M. Rowan-Robinson. "Do type Ia supernovae prove lambda > 0 ?" *arXiv:astro-ph/0201034* (2002).

A. N. S. C. C. Ng and F. Rosati. "Applications of scalar attractor solutions to cosmology". *Phys. Rev. D, 64, p. 083510* (2001).

A. Saha, A. Sandage *et al.* "Cepheid Calibration of the peak brightness of Type Ia Supernovae. IX. SN 1989B in NGC 3627". *Astrophys. J., 522, pp. 802 - 838* (1999).

V. Sahni and L. Wang. "New cosmological model of quintessence and dark matter". *Phys. Rev. D, 62, p. 103517* (2000).

S. Sarkar. "Is the evidence for dark energy secure ?" *arXiv:astro-ph/0710.5307v2* (2007).

G. Smoot, C. Bennett *et al.* "COBE Differential Microwave Radiometers - Instrument design and implementation". *Astrophys. J., 360, pp. 685-695* (1990).

D. Spergel, L. Verde *et al.* "First Year Microwave Anisotropy Probe (WMAP) Observations : Determination of Cosmological Parameters". *Astrophys. J. Suppl. 148, p. 175* (2003).

M. Tegmark, A. de Oliveira-Costa and A. Hamilton. "High resolution foreground cleaned CMB map from WMAP". *Phys. Rev. D, 68(12), p. 123523* (2003).

M. Tegmark, M. Strauss *et al.* "Cosmological parameters from SDSS and WMAP". *Phys. Rev. D, 69, p. 103501* (2004).

J. Tonry and M. Davis. "A Survey of Galaxy Redshifts I. A Data Reduction Techniques". *Astron. J., 84, pp. 1511 - 1525* (1979).

M. Turatto. "Classification of Supernovae." *In LNP Vol. 598: Supernovae and Gamma-Ray Bursters, p. 21* (2003).

S. Weinberg. "Curvature dependence of peaks in the cosmic microwave background distribution". *Phys. Rev. D, 62, p. 127302* (2000).

L. Wells, M. Phillips *et al.* "The Type IA supernova 1989B in NGC 3627 (M66)". *Astron. J., 108, p. 2233* (1994).

Y. Yoshii, T. Tsujimoto and K. Kiwara. "Age Dating of a High-Redshift QSO B1422+231 at Z = 3.62 and Its Cosmological Implications". *Astrophys. J., 507, L113* (1998).

F. Zwicky and W. Baade. "On Super-novae". *PNAS, 20(5), p. 254* (1934).

Chapter 8

Appendix

Matlab version of the code for the grid based χ^2-test

```
clear plot;
clear;

double all;

global tempmatrix
global Xrealspec
global Yrealspec
global Xtempspec
global datalength
global tempmatrixdiv
global Xtempspecdiv
global window
global shift
global tempmatrixdiv
global tempmatrixInPhase
global SplinedTempPhase
global splinedtempmatrixdiv
global Xtempspecprime
global Ytempspecprime
global newstartline
global newend
global Ki_Z_vector
global MinChisQVec
global scope
global fittingspec

tic;

% Reading all the template
```

```
[fid,msg]= fopen('entreSNIa.dat','r','native');
[ttrix countmatrix] = fscanf(fid,'%f',[3,inf]);
fclose(fid);
tempmatrix = ttrix';

% Reading the real data
[fid,msg]= fopen('1992ac10.dat','r','native');
[spec countrealspec] = fscanf(fid,'%f',[2,inf]);
fclose(fid);
realspec = spec';

Xrealspec = realspec(:,1,:);
Yrealspec = realspec(:,2,:);
% Inserting the priors

Zmin = 0.0;
Zmax = 1.0;
Zstep = 0.001;
phasemin = 2;
phasemax = 91;
phasestep = 1;

% Some Technicalities are extracted

datalength = countrealspec/2;
[increment,bas,ctrl] = basicinfomin(Xrealspec,datalength);
lowestwavelength = Xrealspec(1);

% Important for plotting the fit

        k = 1;
        linestart = k*2401 + 1;
        lineend   = linestart + 2400;
        tempspec  = tempmatrix(linestart:lineend,1:3);
        Xtempspec = tempspec(:,2,:);
        [newstartline,daystart,wavel] = locate(tempspec,(lowestwavelength - 0));
        speclong = 2401 - newstartline + 1;
        scope = min(speclong,datalength);
        newend = scope + newstartline - 1;
        numberoflines = newstartline; %- linestart +  1
        tempspecprime  = tempspec(newstartline:newend,1:3);
        Xtempspecprime = tempspecprime(:,2,:);
        Ytempspecprime = tempspecprime(:,3,:);

% Dividing Amplitude of real Data by a smooth fcn obtained via an averaging process
```

```
window = 500;
shift  = 1;
[Xrealspecdiv Yrealspecdiv] = dividespec(Xrealspec,Yrealspec);
datalengthdiv = length(Xrealspecdiv);

% Generating the full set of residual templates and phase splined ones

tempmatrixInPhase = []; % Will be all templates in Phase space
tempmatrixdiv = [];
residualizeTemplatesgrid(); % U get a matrix of residual flux vectors per day + associated Xran

% Gridding

phaseI = floor(phasemin);
phaseF = floor(phasemax) + 1;

InitPhaseRange = phaseI:1:phaseF; % Phase range on which i will spline
FinalPhaseRange = phasemin : phasestep : phasemax; % Subdividing using prior on phase step

t = length(Xtempspecdiv);

% am splining residual templates over phase space by fully using my priors

SplinedTempPhase = splinedPhaseter2(Xtempspecdiv,InitPhaseRange,FinalPhaseRange,phaseI,phaseF,1

        countZ = 1;

        LambdaDmin = Xrealspecdiv(1) ;
        beta = Xrealspecdiv(end - 1);
        tic;
        for Zi = Zmin : Zstep : Zmax
                bluediv = Xrealspecdiv./(1 + Zi);
                Didx = find( (bluediv >= LambdaDmin) & (bluediv <= beta) );
                if ( length(Didx) >= 2 )
                D = Didx(1) ;
                        F = Didx(end);
                        blueInterval = bluediv(D:F); % Associated bluediv truncated
                        PhiDBd = Yrealspecdiv(D:F);
                        SplineResTemplateOverIbd2(Xtempspecdiv,blueInterval);
                elseif (bluediv(1) >= Xtempspecdiv(2))        % Case where only one point left
                        blueInterval = bluediv;
                        SplineResTemplateOverIbd2(Xtempspecdiv,blueInterval);
                        coll = length(splinedtempmatrixdiv(:,1,:));
                        PhiDBd = zeros(1,coll);
```

```
                else
                        Alarm = Zi
                        break;
                end
                countPhase = 1;
             for phase = phasemin:phasestep:phasemax
                chisq(countZ,countPhase) = sum((splinedtempmatrixdiv(:,countPhase,:)-PhiDBd').^
                countPhase = countPhase + 1;
              end
                countZ = countZ + 1;
        end

RedshiftVec = Zmin:Zstep:Zmax;
PhaseVec = phasemin:phasestep:phasemax;

[MinChisQVec, idx] = min(chisq); % Contains column vectors of minimum Ki per phase

[MinChisq, indexP] = min(MinChisQVec); % minimum chi-squared and associated phase
Chi_Squared_min = MinChisq % value of the Ki-squared

Phase = PhaseVec(indexP) - 1 % phase estimate
Bphase = Phase - 20

Ki_Z_vector = chisq(:,indexP,:); % col. vectors of minimum Ki per redshift
[confirmation, indexZ] = min(chisq(:,indexP,:));
Redshift = RedshiftVec(indexZ) % redshift estimate

%Fit7bis(Redshift,Phase + 1)
Fit7(Phase + 1)

finishtime = toc
```


Procedures and functions developed for the grid based χ^2-test

Basicinfomin.m : gives relevant information related to the input data

```
function [increase,low,chek] = basicinfomin(Xtab,length)
% Extracts basic info about input (increment, lower value and a control value)
        somme = 0;
        min =  Xtab(2) - Xtab(1);
        for i = (2 : length)
                temp = Xtab(i) - Xtab(i - 1);
                if (temp < min)
                        min = temp;
                end
```

```
                somme = somme + temp;
        end
        increase = ceil(somme/length);
        low = min;
        chek = temp;
```

dividespec.m : gives the residual spectrum and associated wavelength

```
function [Xvecout Yvecout ] = dividespec(Xvecin,Yvecin)
% Generates the smooth via moving averaging and gives residual spectrum
global datalength
global window
global shift
global scope

looper = length(Xvecin);
n = 0;
start = 1;
lend  = window;
while (lend <= looper)
        n = n + 1;
             tempX    = Xvecin(start:lend);
        Xtemp(n) = sum(tempX)/window;
        tempY    = Yvecin(start:lend);
        Ytemp(n) = sum(tempY)/window;
        start    = start + shift;
        lend     = lend  + shift;
end;
splinedYvecin = spline(Xvecin,Yvecin,Xtemp);
Xvecout = Xtemp;
Yvecout = splinedYvecin./Ytemp;
%New = [Xvecout , Yvecout]
```

residualizeTemplatesgrid.m : Gives a matrix of residual templates ordered in spectrum per day (tempmatrixdiv)

```
function residualizeTemplatesgrid()
% Gives a matrix of residual templates ordered in spectrum per day
% and associated wavelength range
global tempmatrix
global tempmatrixdiv
global tempmatrixInPhase
global Xtempspecdiv
global Xtempspec

k = 0;
        debut = k*2401 + 1;
```

```
        fin   = debut + 2400;
        Xtempspec = tempmatrix(debut:fin,2:2);
        Xtempspecdiv = divideLambda(Xtempspec); % Wavelength range for each spectrum
while (k <= 90)
        linestart  = k*2401 + 1;
        lineend    = linestart + 2400;
        Ytempspec  = tempmatrix(linestart:lineend,3:3);

        Ytempspecdiv = divideTspec(Xtempspec,Ytempspec);

        tempmatrixdiv     = [tempmatrixdiv , Ytempspecdiv'];
        tempmatrixInPhase = [tempmatrixInPhase , Ytempspec];
    k = k + 1;
end
```

splinedPhaseter2.m : splines template residuals over phase space by fully using priors

```
function [interpo] = splinedPhaseter2(V0,V1,V2,scal1,scal2,scal3,scal4)
% Gives residual spectra associated to our priors on phase
% given on Xtempspecdiv range
global datalengthdiv
global tempmatrixdiv
global Xtempspecdiv

        looper = length(V0);
        ligne = 2:1:91;
        length(ligne);
        matrice   = tempmatrixdiv(1:looper,2:91)';
        length(matrice(:,1));
        tempo = interp1(ligne,matrice,V2,'spline'); % Splining
        interpo = tempo; % This is the desired (residual) spectra
```

SplineResTemplateOverIbd2.m : splines residual template over the range defined by the blueshifted data

```
function SplineResTemplateOverIbd2(V1,V2)
% Generates residual template over same X-range as blueshifted data
global tempmatrix
global tempmatrixdiv
global splinedtempmatrixdiv
global SplinedTempPhase

            splinedtemp = interp1(V1, SplinedTempPhase', V2, 'spline'); % Splining
        splinedtempmatrixdiv = splinedtemp; % This is the desired (residual) spectra

%end
```

Fit7.m : plots the original data and the matching template at $Z = 0$

```
function Fit7(Phi) % Should plot the data and the best fit given by phase phi
global Yrealspec
global Xrealspec
global Xtempspecprime
global Xtempspecprime
global datalength
global tempmatrixInPhase
global newstartline
global newend
global scope
global datalength
global fittingspec

        day = floor(Phi);
            ligne = 2:1:91;
            matrice = tempmatrixInPhase(newstartline:scope,2:91)';
            if ( day == Phi ) && ( Phi >= 2 ) && ( Phi <= 91)
                interpo = tempmatrixInPhase(newstartline:scope,day:day);
            elseif ( Phi >= 2 ) && ( Phi <= 91)
                        tempo = interp1(ligne, matrice, Phi, 'spline'); % Splining
                        interpo = tempo; % This is the desired (residual) spectra
        else
                interpo = tempmatrixInPhase(newstartline:scope,1:1);
            end
        xlabel('Wavelength (angstroms)');
        ylabel('Flux (arbitrary units');
        fittingspec = interpo;
        a = length(fittingspec);
        rayon = min(datalength,a)
        Tidx  = find((Xtempspecprime >= Xrealspec(1)) & (Xtempspecprime <= 10000));
        Didx  = find( Xrealspec <= 10000 );
        aT = Tidx(1);
        bT = Tidx(end);
        bD = Didx(end);
        plot(Xrealspec(1:bD),Yrealspec(1:bD),'--r' ,...
        Xtempspecprime(aT:bT),fittingspec(aT:bT),'-.b')
            h = legend('data','Matching template at z = 0',1);
```

Matlab version of the MCMC code

```
clear;
clear all;
clear plot;
```

```
global kisquareprev
global kisquarenext
global tempmatrix
global Xrealspec
global Yrealspec
global Yrealspecdiv
global Xrealspecdiv
global Ytempspecdiv
global Xtempspecdiv
global Xtempspec
global Xtempspecprime
global SNxspline
global datalength
global paramvector
global overallKi
global overallLiK
global chainsnumber
global stepsnumber
global Kioverallchains
global Allchains
global mergedChain
global TheChain
global rowofmean
global rowofvar
global RforConvergence
global autoco
global CorrelationLength
global EffectiveLength
global scope
global initial
global probablenext
global window
global shift
global numberoflines
global numberoflinesdiv
global Template
global tempmatrixdiv
global tempmatrixdivonGrid
global tempmatrixInPhase
global datalengthdiv
global lowestwavelengthdiv
global newstartline
global newend
global fittingspec
```

```
global LiKoverallchains
global BurnInchain
global ratio


% Reading all the template


[fid,msg]= fopen('entreSNIa.dat','r','native');
[ttrix, countmatrix] = fscanf(fid,'%f',[3,inf]);
fclose(fid);
tempmatrix = ttrix';

% Reading the real data

[fid,msg]= fopen('2003duout.dat','r','native');
[spec countrealspec] = fscanf(fid,'%f',[2,inf]);
fclose(fid);
realspec = spec';

Xrealspec = realspec(:,1,:);
Yrealspec = realspec(:,2,:);

% Some Technicalities are extracted

datalength = countrealspec/2;
[increment,bas,ctrl] = basicinfomin(Xrealspec,datalength);
lowestwavelength = Xrealspec(1);

% needed Xrange from template (identical for all templates)

k = 1;
linestart = k*2401 + 1;
lineend   = linestart + 2400;
tempspec  = tempmatrix(linestart:lineend,1:3);
Xtempspec = tempspec(:,2,:);
        [newstartline,daystart,wavel] = locate(tempspec,(lowestwavelength - 0));
        speclong = 2401 - newstartline + 1;
        scope = min(speclong,datalength);
        newend = scope + newstartline - 1;
        numberoflines = newstartline; %- linestart +  1
        tempspecprime  = tempspec(newstartline:newend,1:3);
        Xtempspecprime = tempspecprime(:,2,:);

% Obttaining data residual spectrum
```

```
window = 500;
shift  = 1;

spec = dividespec2(Xrealspec,Yrealspec);
Xrealspecdiv = spec(:,1,:);
Yrealspecdiv = spec(:,2,:);
datalengthdiv = length(Yrealspecdiv);


% Generating the full set of residual templates

tempmatrixInPhase = [];  % Will be all templates in Phase space
tempmatrixdiv = [];
tempmatrixdivonGrid = [];
BurnInchain = [];

Xtempspecdiv = divideLambda(Xtempspec); % wavelength range for each residual template
lowestwavelengthdiv = Xtempspecdiv(1);

residualizeTemplates5;
% U get a matrix of residual flux vectors per day + associated Xrange


% MCMC

% Defining the number of steps per Chain

stepsnumber = input('Desired number of Steps for each Chain (preferably even number) ? \n');

% Defining the number of desired chains

chainsnumber = input('Desired Number of Chains ( preferably => 2 ) ? \n');

Kioverallchains = []; % Important matrices to initialize
LiKoverallchains = [];
mergedChain = [];
rowfomean = [];
rowofvar = [];

i = 1;

        sigma1 = 0.1; % Step size for redshift in the Jump vector
        sigma2 = 1;    % Step size for Phase in the jump vector
```

```
for k = ( 1 : chainsnumber)
        step = 1;
        PhaseI      = 15 + (35 - 15)*rand ; % A number between 2 and 91
        paramvector = [max(0,0.001 + (0.100 - 0.001).*rand(1,1)), PhaseI];

        Zprev   = paramvector(1);
        dayprev = paramvector(2);

           Yprevdiv = splinedPhase7(dayprev); % residual at phase = dayprev

        kisquareprev   = kisquaredparam4(Zprev,Yprevdiv);  % Scalar

        overallKi(step,:) = kisquareprev; % Help for BurnIn solving
           overallLiK(step,:) = exp( - kisquareprev/2 ); % help for BurnIn solving


% Acting
        for step = 1 : stepsnumber - 1
            step = step + 1;
            Gaussian1 = 0 + sigma1.*randn; %From Gauss. distrib with mean 0 and std ~ sigma1
            Gaussian2 = 0 + sigma2.*randn; %From Gauss. distrib with mean 0 and std ~ sigma2
            jump = [Gaussian1,Gaussian2]; % Gaussian1 and Gaussain2 can be < 0
            initial = paramvector(step - 1,:); % A row vector
            probablenext = initial + jump; % A row vector

            Zprev   = initial(1);
            dayprev = initial(2);
            Znext   = probablenext(1);
            daynext = probablenext(2);
            [Yprevdiv,Ynextdiv] = splinedPhase4cinqo(dayprev,daynext);
            [kisquareprev,kisquarenext] = kisquaredparam3quatro2(Zprev,Yprevdiv,Znext,Ynextdiv)

            decisionfactoR = exp( -(kisquarenext - kisquareprev)/2); % Scalar

            i = i + 1;
            Updateparam5(step, decisionfactoR, initial , probablenext);
        end


        % Column vector keeping the Kisquared values per step of the full Chain
        Kioverallchains = [Kioverallchains ; overallKi];
        % Column vector keeping the likelihood values per step of the full Chain
        LiKoverallchains = [LiKoverallchains ; overallLiK];
        mergedChain = [mergedChain ; paramvector]; % Full Chain
        temp = paramvector(stepsnumber/2 : stepsnumber, 1:2);
```

```
        % Extracting some parameter vectors for Conv. & Mixing check.
        rowofmean(k,:)  = mean(temp); % mean of each sub-chain in the truncated whole.
        rowofvar(k,:) = [ cov(temp(:,1)) cov(temp(:,2)) ]; % variance within each sub-chain.

end

SolveBurnIn; % Solves Burn-in
merged = length(mergedChain(:,1,:))
Newmerged = length(TheChain(:,1,:))

ConvMix2; % check convergence
RforConvergence % is the convergence/mixing criterion
%autocorrelationbis();

Chi_squared = min(Kioverallchains)
redshift = mean(TheChain(:,1,:))
sigmaredshift = std(TheChain(:,1,:))
phase = mean(TheChain(:,2,:))
Bphase = phase - 20
sigmaphase = std(TheChain(:,2,:))
Fit7(phase); % For plotting
```

Procedures and functions developed for the MCMC code

Basicinfomin.m : detailed above. Gives relevant information related to the input data

dividelambda.m : gives the X-range associated to the output from divide.m

```
function [vecout] = divideLambda(vecin)
global datalength
global window
global shift

looper = length(vecin);
n = 0;
start = 1;
lend  = window;
while (lend <= looper)
        n++;
        temp     = vecin(start:lend);
        Xtemp(n) = sum(temp)/window;
        start    = start + shift;
        lend     = lend  + shift;
endwhile;
extent = min(looper,length(Xtemp));
```

```
vecout = Xtemp;
return;
endfunction
```

Fit7.m : detailed above. Plots original data and matching template at $Z = 0$.

residualizeTemplates5.m : Generates the full matrix of residual templates

```
function residualizeTemplates5()
% Gives a matrix of residual templates ordered in spectrum per day
% + a set on the same X-grid as the data ----> tempmatrixdivonGrid
global tempmatrix
global tempmatrixdiv
global tempmatrixInPhase
global datalengthdiv
global numberoflinesdiv
global Xrealspecdiv
global Xtempspecdiv
global Xtempspec
global lowestwavelengthdiv
global tempmatrixdivonGrid

plafond = length(Xtempspecdiv);
bound = find(Xrealspecdiv < Xtempspecdiv(plafond));
intake = Xrealspecdiv(1:bound(length(bound)));
k = 0; % From Phase 0 to Phase 90
while (k <= 90)
        linestart = k*2401 + 1;
        lineend   = linestart + 2400;

            Ytempspec  = tempmatrix(linestart:lineend,3:3);
        Ytempspecdiv = divideTspec(Xtempspec,Ytempspec);

        YtempspecdivonGrid = spline(Xtempspecdiv,Ytempspecdiv,intake);
        % Puting templates on same grid as data

            tempmatrixInPhase   = [tempmatrixInPhase , Ytempspec];
        % Template ordered in increasing phase/day
        tempmatrixdiv       = [tempmatrixdiv , Ytempspecdiv'];
        tempmatrixdivonGrid = [tempmatrixdivonGrid , YtempspecdivonGrid'];
        % Template and Data are now on the same grid

        k = k+1;
end
```

splinedPhase7.m : returns the residual spectrum associated to a candidate phase phi

```
function [spectrumtdiv] = splinedPhase7(Phi)
% Returns a residual spectrum associated to candidate phase phi
global Xrealspecdiv
global datalengthdiv
global numberoflinesdiv
global scope
global tempmatrixdiv
global tempmatrixdivonGrid
global tempmatrixInPhase

        alpha = floor(Phi);
        beta = ceil(Phi);
        long = length(tempmatrixdiv(:,1,:));
                %Xtemp = 2:1:91;
                if ( ( Phi <= 91 ) & ( Phi >= 2 ) )
                if ( alpha >= 89 ) % and always <= 91
                    bf = beta;
                    bi = beta - 3;
                    Xtemp = bi:1:bf;
                    extract = tempmatrixdiv(:,bi:bf)';
                    tempo = interp1(Xtemp, extract, Phi, 'spline'); % Splining
                    spectrumtdiv = tempo(1,:); % (residual) spectrum at Phi over
                    %Xrealspecdiv (Both are now on the same grid)
                elseif ( alpha < 89 ) % and always >= 2
                    ai = alpha;
                    af = alpha + 3;
                    Xtemp = ai:1:af;
                    extract = tempmatrixdiv(:,ai:af)';
                    tempo = interp1(Xtemp, extract, Phi, 'spline'); % Splining
                    spectrumtdiv = tempo(1,:); % (residual) spectrum at Phi over
                    %Xrealspecdiv (Both are now on the same grid)
                elseif ( beta <= 4 ) % and always >= 2
                    ai = alpha;
                    af = alpha + 3;
                    Xtemp = ai:1:af;
                    extract = tempmatrixdiv(:,ai:af)';
                    tempo = interp1(Xtemp, extract, Phi, 'spline'); % Splining
                    spectrumtdiv = tempo(1,:); % (residual) spectrum at Phi over
                    %Xrealspecdiv (Both are now on the same grid)
                elseif ( beta > 4 ) % and always >= 2
                    bf = beta;
                    bi = beta - 3;
                    Xtemp = bi:1:bf;
                    extract = tempmatrixdiv(:,bi:bf)';
                    tempo = interp1(Xtemp, extract, Phi, 'spline'); % Splining
```

```
                spectrumtdiv = tempo(1,:); % (residual) spectrum at Phi over
                %Xrealspecdiv (Both are now on the same grid)
            end
        else
           % spectrumtdiv = tempmatrixdiv(:,1,:)'; % i.e Phase 0
            spectrumtdiv = zeros(1,long); % i.e Phase 0
        end
```

kisquaredparam4.m : χ^2 associated to a candidate spectrum

```
function [scalout] = kisquaredparam4(scal1,V1)
% Returns the calculate chi-square associated
% to candidate spectrum V1 at candidate redshift scal1
global Xtempspecprime
global SNxspline
global Xrealspec
global Yrealspec
global Xrealspecdiv
global Yrealspecdiv
global datalength
global scope
global Xtempspecdiv
global numberoflinesdiv

            spec  = [Xtempspecdiv' , V1'];
            Rspec = redshift(scal1,spec);
            redTspec = spline(Rspec(:,1,:),Rspec(:,2,:),Xrealspecdiv);
            scalout = (sum((Yrealspecdiv - redTspec).^2)); % redTspec is candidate spec.
```

splinedPhase4cinqo.m : returns residual spectra associated to two candidate spectra

```
function [spectrumtdiv1,spectrumtdiv2] = splinedPhase4cinqo(Phi1,Phi2)
% Returns 2 residual spectra associated to candidate phase phi1 & phi2
% from the database of residual spectra
global Xrealspecdiv
global datalengthdiv
global numberoflinesdiv
global scope
global tempmatrixdiv
global tempmatrixdivonGrid
global tempmatrixInPhase

        spectrumtdiv1 = splinedPhase7(Phi1);

        spectrumtdiv2 = splinedPhase7(Phi2);
```

kisquaredparam3quatro2.m : χ^2 associated to two candidate spectra

```
function [scalout1,scalout2] = kisquaredparam3quatro(scal1,V1,scal2,V2)
% Returns the calculate chi-square associated to candidate spectrum V1, V2
% at candidate redshift scal1 & scal2 resp.
global Xtempspecprime
global SNxspline
global Xrealspec
global Yrealspec
global Xrealspecdiv
global Yrealspecdiv
global datalength
global scope
global Xtempspecdiv
global numberoflinesdiv

        scalout1  = kisquaredparam4(scal1,V1);
        if (0 <= scal2)
                scalout2  = kisquaredparam4(scal2,V2);
        else
                scalout2 = scalout1 + 10000000;
        end
```

Updateparam5.m : updates the vector of parameters if a candidate step is taken or rejected

```
function Updateparam5(n, V1, V2, V3)
% Update the vector of parameters if the candidate step is taken or not
global paramvector
global overallKi
global overallLiK
global kisquareprev
global kisquarenext

        if ( 1 <= V1 ) % From the decisionfactoR factor
                temp1 = V3; % Take the new step
                temp2 = kisquarenext;
                temp3 = exp( - kisquarenext/2 );
        else
                temp4 = rand; % Drawing a number in the region [0,1]
                if ( temp4 <= V1 )
                        temp1 = V3; % Take the new step
                        temp2 = kisquarenext;
                        temp3 = exp( - kisquarenext/2 );
                else
                        temp1 = V2; % Remain and reject new step
                        temp2 = kisquareprev;
                        temp3 = exp( - kisquareprev/2 );
                end
```

```
        end
        paramvector(n,:)= temp1; % row vector
        overallKi(n,:)  = temp2; % row vector
           overallLiK(n,:) = temp3;
```

SolveBurnin.m : solves the "burn in" problem

```
function SolveBurnIn()
% Routine for solving the "burn-in" problem
global Allchains
global paramvector
global chainsnumber
global stepsnumber
global Kioverallchains
global mergedChain
global TheChain
global overallLiK
global LiKoverallchains
global BurnInchain

        merger = [];
            V2 = median(LiKoverallchains); % A scalar
        for i = ( 1 : chainsnumber)
                fin   =        i*stepsnumber;
                debut =        (fin - stepsnumber) + 1;
                tempLikchain = LiKoverallchains(debut:fin); % likelihoods per step in i-th Chai
                tempchain = mergedChain(debut:fin,1:2); % Extracting the i-th chain
                j = 1;
                while (j <= stepsnumber)
                        if ( V2 <= tempLikchain(j))
                                topup = tempchain(j + 1 : stepsnumber,1:2);
                                merger = [merger ; topup];
                                BurnInchain(i) = j;
                                break;
                        end
                        j=j+1;
                end
        end
        TheChain = merger;
```

ConvMix2.m : checks for convergence and good mixing by giving the R parameter

```
function ConvMix2()
% Checks for convergebnce and good mixin via the Gelman-Rubin test
global chainsnumber
global stepsnumber
global rowofmean
```

```
global rowofvar
global Kioverallchains
global mergedChain
global RforConvergence
global overallLiK
global LiKoverallchains
global ratio

        N = stepsnumber/2;
        M = chainsnumber;
        Ybar = mean(rowofmean);% mean of whole truncated chain

        X1 = sum( ( rowofmean(:,1) - Ybar(:,1) ).^2  ).*(1/(M - 1));
        X2 = sum( ( rowofmean(:,2) - Ybar(:,2) ).^2  ).*(1/(M - 1));
        Bn = [X1 X2]; % variance between the merged chains

        W  = ( N/(N - 1)).*mean(rowofvar); variance within each chain

        RforConvergence =  (( (N - 1)/N).*W + (1 + 1/M).*Bn )./W;
```